UNIVERSITY OF CALIFORNIA SAN DIEGO

Design of Printed Ocean Sensor for Real-time Monitoring in Marine Environments

A Dissertation submitted in partial satisfaction of the requirements
for the degree Doctor of Philosophy

in

Materials Science and Engineering

by

Shuo-En Wu

Committee in charge:

Professor Tse Nga Ng, Chair
Professor Renkun Chen
Professor Drew Hall
Professor Yu-Hwa Lo

2023

THE DISSERTATION OF SHUO-EN WU IS APPROVED, AND IT IS ACCEPTABLE IN QUALITY AND FORM FOR PUBLICATION ON MICROFILM AND ELECTRONICALLY.

University of California San Diego

2023

DEDICATION

To my family

.

TABLE OF CONTENTS

LIST OF FIGURES

LIST OF TABLES

ACKNOWLEDGEMENTS

I would like to express my gratitude to my advisor, Professor Tse Nga Ng, for her unwavering support throughout my PhD career. Her guidance, mentorship, and expertise have played a pivotal role in shaping the direction of my research. From the very beginning, she provided critical feedback and offered invaluable insights that have significantly influenced the trajectory of my academic pursuits. The countless suggestions and comments she shared have not only refined my research but also molded the way I approach my endeavors in the academic realm. I am truly indebted to her for her dedication and commitment to my success.

I would also like to extend my gratitude to the incredible members in our lab who have been instrumental in supporting and encouraging me during my research journey. Their contributions and support have played an integral role in my growth as a researcher, and I am immensely grateful for their presence in my academic life.

I would like to express my deep appreciation to my family, who have stood by my side and provided unwavering support throughout the ups and downs of my PhD journey. Their love, understanding, and encouragement have been a constant source of strength, especially during the challenging times presented by the COVID-19 pandemic. Their mental and emotional support have surpassed anything I could have ever imagined, and I am forever grateful for their belief in me and my aspirations.

Completing a PhD is not merely an academic accomplishment; it is a transformative and life-altering experience. This journey has been an exceptional one, filled with numerous challenges, personal growth, and moments of profound self-discovery. It has become a critical turning point in my life, shaping not only my academic skills and innovation breakthroughs but also providing me with a new lens through which I evaluate and appreciate the world around me.

This degree represents not just the culmination of years of hard work but also a profound shift in my perspective and a gateway to a future filled with endless possibilities.

Chapter 2, in part, is a reprint of the material as it appears in Advanced Electronic Materials. Shuo-En Wu, Lulu Yao, Alan Shiller, Andrew H Barnard, Jason David Azoulay and Tse Nga Ng. 2021. Dual-Gate Organic Electrochemical Transistors for Marine Sensing. The dissertation author was the primary investigator and author of this paper.

Chapter 3, in part, is a reprint of the material as it appears in Microchimica Acta. Shuo-En Wu, Alan Shiller, Andrew H Barnard, Jason David Azoulay and Tse Nga Ng, 2022. Point-of-use printed nitrate sensor with desalination units. The dissertation author was the primary researcher and author of this paper.

Chapter 4, in part, is a reprint of the material as it appears in Nanoscale. Shuo-En Wu, Napasorn Phongphaew, Yichen Zhai, Lulu Yao, Hsun-Hao Hsu, Alan Shiller, Jason David Azoulay and Tse Nga Ng, 2022. Point-of-use printed nitrate sensor with desalination units. The dissertation author was the primary researcher and author of this paper.

Chapter 5, in part is currently being prepared for submission for publication of the material. Shuo-En Wu, Longhui Zeng, Yichen Zhai, Chanho Shin, Naresh Eedugurala, Jason David Azoulay, Tse Nga Ng, 2023. Retinomorphic motion detector fabricated with organic infrared semiconductors. The dissertation author was the primary researcher and author of this material.

VITA

2014 Bachelor of Science, National Tsing-Hua University, Hsinchu, Taiwan

2016 Master of Science, National Tsing-Hua University, Hsinchu, Taiwan

2023 Doctor of Philosophy, University of California San Diego, USA

PUBLICATIONS

[1] **Shuo-En Wu**, Lulu Yao, Alan Shiller, Andrew H. Barnard, Jason David Azoulay, and Tse Nga Ng. "Dual-Gate Organic Electrochemical Transistors for Marine Sensing." Advanced Electronic Materials 7, 6 (2021)

[2] **Shuo-En Wu**, Alan Shiller, Andrew Barnard, Jason D. Azoulay, Tse Nga Ng. "Point-of-Use Printed Nitrate Sensor with Desalination Units" Microchimica Acta, 189.6 (2022): 1-9.

[3] **Shuo-En Wu**, Napasorn Phongphaew, Yichen Zhai, Lulu Yao, Hsun-Hao Hsu, Alan Shiller, Jason Azoulay, Tse Nga Ng. "Multiplexed Printed Sensors for In-Situ Monitoring in Bivalve Aquaculture'' Nanoscale, (2022)14, 16110-16119

[4] **Shuo-En Wu**, Longhui Zeng, Yichen Zhai, Chanho Shin, Naresh Eedugurala, Jason David Azoulay, Tse Nga Ng, "Retinomorphic Motion Detector Fabricated with Organic Infrared Semiconductors'', *under preparation*.

ABSTRACT OF THE DISSERTATION

Design of Printed Ocean Sensor for Real-time Monitoring in Marine Environments

by

Shuo-En Wu

Doctor of Philosophy in Materials Science and Engineering

University of California San Diego, 2023

Professor Tse Nga Ng, Chair

In marine studies, the current sensors technologies have limitations such as time-consuming batch sample analysis, size-weight-power restrictions, and complex encapsulation, which impedes real-time in-situ measurements. In this thesis, we develop printed integrated ocean sensor designs that address the challenges through novel device configurations and soft materials selection and processing and integration strategies.

My novel device configuration of dual-gate organic electrochemical transistors (OECTs) extended the operating potential window over 2 V with remarkable stability, allowing high potential redox reactions to occur. Detailed analysis of the operating principle has been derived by introducing two capacitance ratios to describe the mechanism of modulating the channel conductance. The printed dual-gate OECTs achieves a detection limit of 0.3 ppm dissolved oxygen concentration in seawater, with a sensitivity of 222 $\mu A\ cm^{-2}\ ppm^{-1}$ for concentrations below 5 ppm.

My second approach to enhance the sensitivity of the printed integrated ocean sensor is through the use of a compact microfluidics design. This design allows for the in-situ detection of target anions that are generally interfered with by the high background of chloride, especially under seawater. The tandem microfluidics structure comprises a flow feeding unit, two desalination electrochemical cells, channel extensions to reduce signals cross talk, and downstream detection through a solid-state ion-selective membrane (ISM) sensor. The integration of these components was achieved through digital cutting, stencil-printing, and lamination. This printed microfluidics platform has demonstrated a detection limit of 0.5 mM nitrate with a sensitivity of 11.3 mV/dec under a continuous seawater flow, with a response time within 8 minutes.

The integration of electronic components into printed ocean sensors has been demonstrated, allowing for the simultaneous detection of multiple signals, including dissolved oxygen, salinity, and curvature changes, using customized integrated multiplexer (MUXs) systems. The printed integrated ocean sensor was constructed by patterning conductive carbon paste/graphite foils onto a flexible plastic substrate. The active devices were fabricated through electrodeposition in different configurations, including electrochemical cells and transistor structures. This integrated

ocean sensor demonstrated the feasibility of detecting oyster gape down to sub-mm levels, with a measurement range of dissolved oxygen between 0.5-6 ppm and salinity between 4-40 g kg^{-1}.

In addition, I also contributed to the development of an organic retinomorphic sensor for infrared spectrum. The sensor achieved a noise-equivalent power of 0.24 nW over 0.09 cm^2 detector area. Leveraging the technique of intensity-modulated photovoltage spectroscopy from the photovoltaic community, my study probed the detector operation mechanism and in turn enhanced the sensor detectivity by interfacial modifications. The improved sensor is compatible with the aforementioned ocean sensors and has the potential to serve as a high-performance motion detector in ocean environments.

CHAPTER 1: INTRODUCTION

Ocean plays a critical role in regulating the Earth's climate, providing food and livelihoods for tens of millions of people and supporting a diverse array of marine life. However, human activities including pollution or overfishing are transforming the morphology of our oceans. Understanding the complexities of the ocean environment is crucial for maintaining its health and sustainability. Researchers are investigating various aspects of the ocean, including its chemistry, biology, physics, and geology in order to gain a comprehensive understanding of how it functions and how it is changing over time. These studies are essential for developing effective strategies to address the pressing environmental challenges facing our Earth environments.

1.1 Challenges in current ocean detection technologies

One critical area of research is the study of marine biology. The ocean is home to a vast array of species, many of which are still poorly understood. Marine biologists are investigating how different individuals interact with each other and their environment, including how they adapt to changing conditions, and how they respond to environmental changes brought by human activities. Another important area of research is the study of ocean chemistry. The chemical composition of seawater is crucial for the survival of marine life, and it can also impact global climate patterns. Many works are carried out how various chemical compounds, such as carbon dioxide and nitrogen, cycle through the ocean, and how human activities are affecting these cycles. Despite extensive research efforts to investigate various aspects of the ocean environment and propose useful technologies, many areas remain unknown and require more advanced sensor technology to be solved. For instance, the current technique of collecting seawater samples through batch sampling on research vessels is a well-developed technique as shown in Figure 1.1a. However, it cannot reflect real-time dynamic changes in the seawater environment and may take several days

to provide information. Thus, there is a pressing need for more advanced sensor technology to enable real-time monitoring of the ocean environment, which can provide insights into the understandings of marine species and their reaction to the dynamic environmental changes.

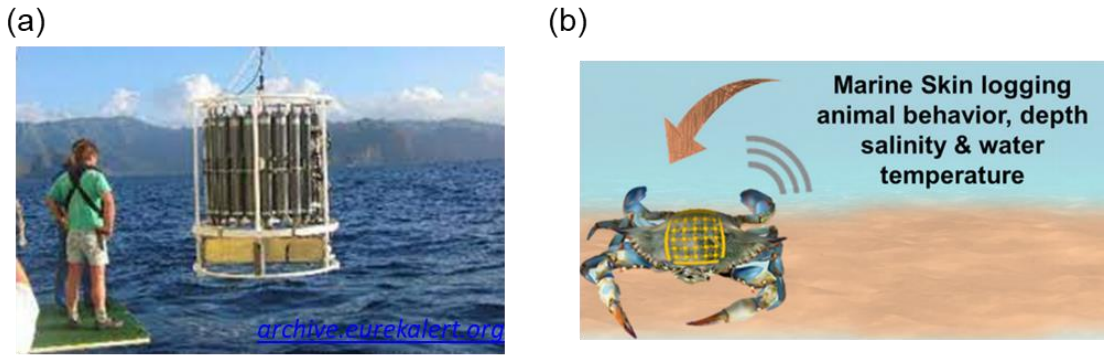

Figure 1.1. Ocean research methodology. (a) Ocean samples analysis through batch-sample collection. (b) The integrated sensors array to deliver in-situ reaction of marine species and environmental changes[1].

In particular, the concept of integrated flexible sensors and integrated circuits has sparked significant interest in marine biology, as it enables real-time tracking of the behavior of marine species in response to environmental changes[1] illustrated in Figure 1.1b. Therefore, the development of an integrated ocean sensor that can provide real-time in-situ measurements of marine species behavior and environmental changes is highly desirable. Our proposed integrated ocean sensor is expected to possess the following advantages: (1) a substrate/platform that is compatible with multiple sensors, (2) the ability to provide in-situ and real-time information in seawater, (3) high sensitivity, small size, robust/flexible design, and low cost. This proposed integrated ocean sensor can address the challenges mentioned above and have further applications in pollution analysis, ocean profile research, aquaculture and beyond, as illustrated in Figure 1.2.

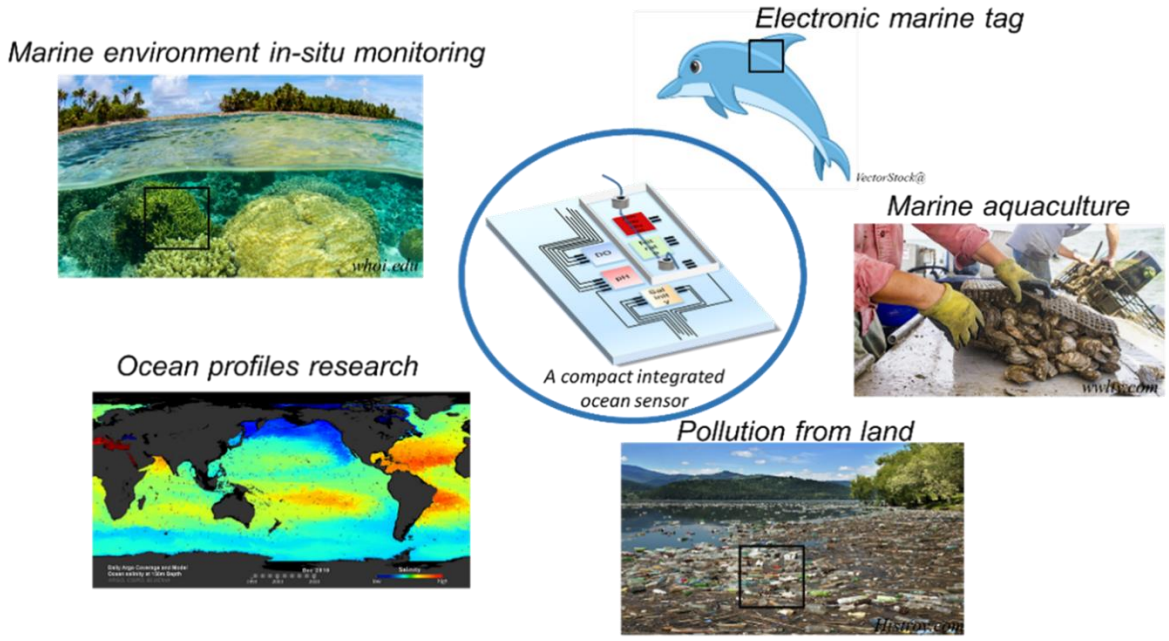

Figure 1.2. The potential uses of proposed compact integrated printed ocean sensor

1.2 Organic mixed ionic and electronic conductors (OMIECs)

Given the high intrinsic ionic conductivity of seawater due to the presence of sodium chloride, the development of integrated ocean sensors based on electrochemical detection is highly promising. Electrochemical sensors have already been developed for various applications and able to detect a wide range of target analytes within aqueous electrolytes. Among those developing materials, organic mixed ionic and electronic conductors (OMIECs) have gained wide interest since 1980s as materials for battery electrodes due to their ability to support electronic and ionic transport, resulting in high throughput and compatibility with specific receptors under aqueous environment[2–8].

OMIECs are mainly composed of π-conjugated polymers (CPs), but also consist of radical polymers and conjugated small molecule systems. Mixed conduction is facilitated by either containing or readily solvating mobile ionic species according to their respective molecule structure and electrolyte components, OMIECs require either the presence of mobile ionic species

or the ability to readily solvate them. The level of electrical and ionic transportation can be further characterized based on the combination class, as depicted in Figure 1.3.

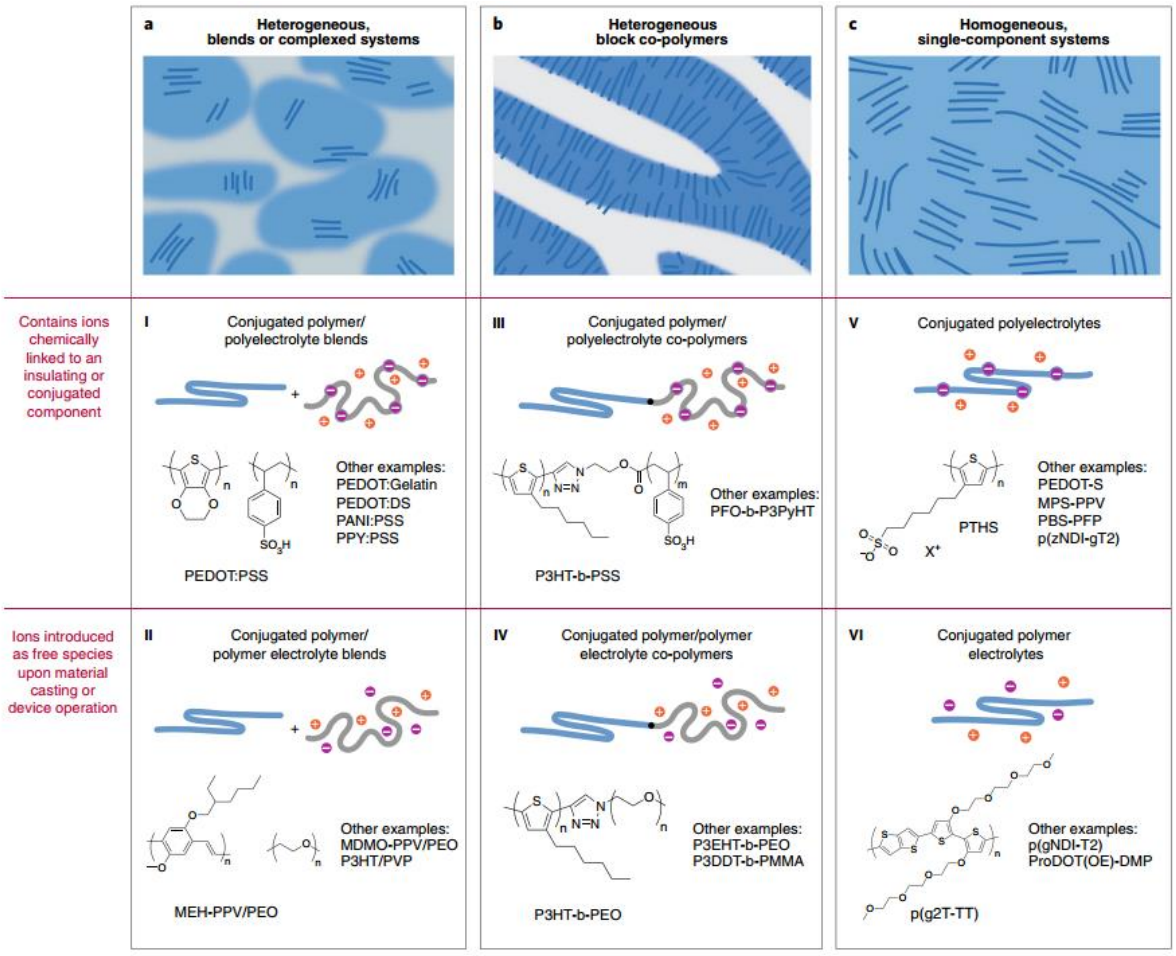

Figure 1.3. The class of OMIECs and their composition[4]

This classification is based on the level of electronic or ionic conductivity contribution, resulting from the respective microstructure of CPs and solvation level of the materials in the electrolyte. The most extensively researched and developed OMIECs is poly(3,4-ethylenedioxythiophene) polystyrene sulfonate (PEDOT:PSS), which belongs to Type 1 in the figure. PEDOT:PSS has been extensively studied and used in various applications, with a focus on its conjugated electrical properties. However, recent studies have demonstrated its impressive

mixed-ionic conductivity by employing organic/water-based electrolyte, grafting moieties on PEDOT conjugated chain or adjusting doping level of conjugated chain by various counter ions dopants[2,9,10]. The solvation effect to the fabricated thin films plays a significant role in OMIECs research, it determines the level of electrical contribution from ionic or electronic properties, as shown in Figure 1.4. The electrical conductivity of OMIECs can have transition from dominantly electronic transport to dominantly ionic conductivity, depending on the surrounding aqueous condition and different wetting level of deposited thin-film materials. This transition can occur as the material changes from a thin-film electronic transport to mobile ion transportation within surrounding electrolyte or both.

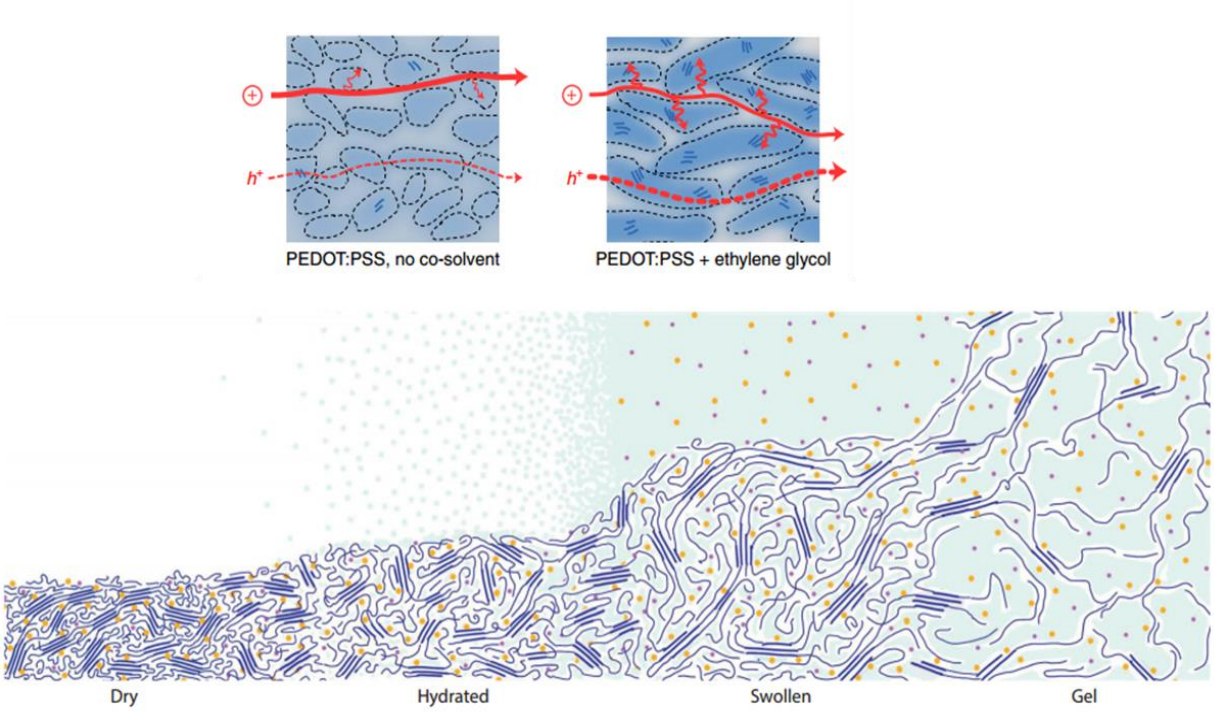

Figure 1.4. The solvation of the thin-film organic semiconducting layer plays a significant role in the electrical conductivity of OMIECs. As the film swells in the solvent, the ionic conductivity becomes the dominant contributor to electrical conductivity. This is due to the loss of charge hopping segments that disperse in the electrolyte[6,11].

The figure-of-merit device performances of OMIECs is determined by the contributions of both electrical and ionic conductivity, which has been extensively studied. Figure 1.5 illustrates the operation principle of organic electrochemical transistors (OECTs) with PEDOT as a conductive channel. The conductance of the channel is controlled by the applied gate bias, which also determines the doping level of PEDOT. When a higher gate bias is applied, mobile ions penetrate the PEDOT film, and the doping level of the conjugated property from the intrinsic sulfonate anions is balanced out by the injected cations from the electrolyte. In order to reach local charge balance, the hole densities responsible for electrical conduction are reduced (or extracted through source-drain electrodes), resulting in a loss of conductance at higher gate bias. This principle is mostly applied to most OMIECs based OECTs and widely used to be biosensor or signal amplifier in the aqueous conditions[12,13].

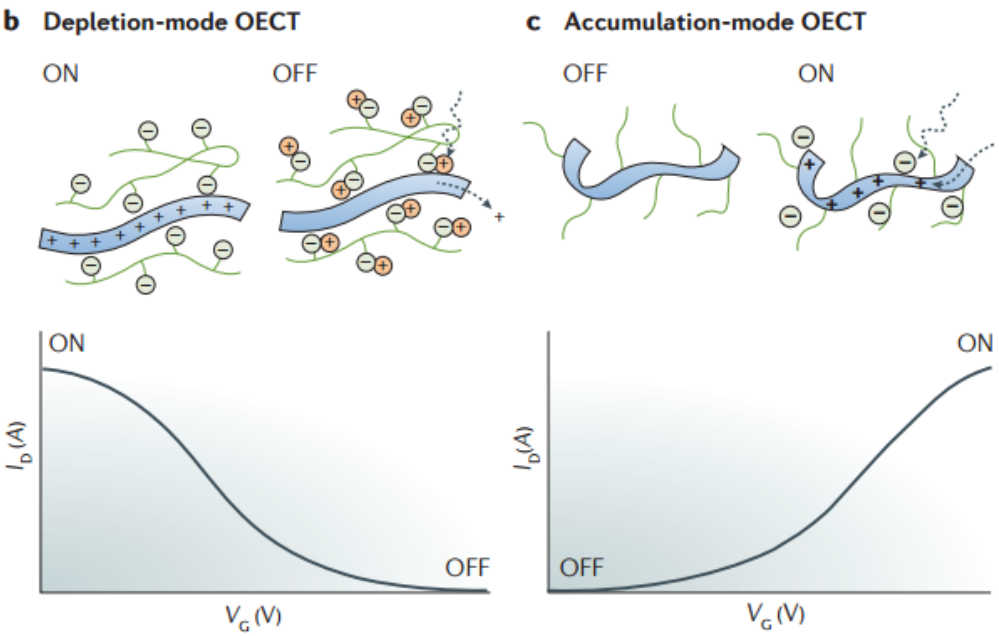

Figure 1.5. Mobile ions penetration into bulky semiconducting films, resulting in changes of conductance in OECTs operation[12].

OMIECs design strategies aim to improve overall charge throughput and compatibility with various electrolyte conditions. Among these, water-based electrolytes are particularly intriguing due to their accessibility and wide range of potential applications in daily life. As a result, grafting glycol side chains onto the π-conjugated polymer, as shown in Figure 1.6, is a common strategy since it greatly increases water solvation ability, which enhances the swelling level of CPs and resulting in effective doping from mobile ions under water-based electrolytes.

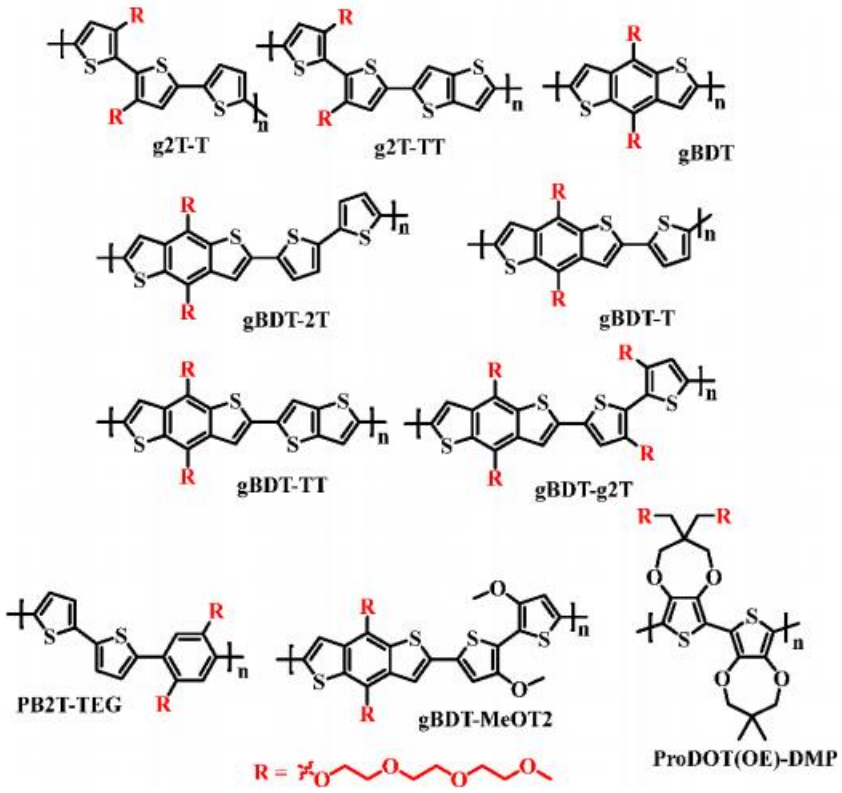

Figure 1.6. Class of p-conjugated polymer grafted with glycol side chains[3,8].

One of major challenges in the OMIECs device operation under water-based electrolyte is the occurrence of oxygen reduction reactions (ORRs)[14]. The electrochemical redox stability of OMIECs is dependent on the operating potential window within the capacitive window, in the absence of oxygen reduction reactions (ORRs). Given the presence of water in water-based

electrolytes, ORRs can unavoidably occur, making it challenging to achieve long-term stability of OMIECs devices. To address this issue, a common strategy is to enhance the electrochemical overpotential, which can help to extend the operating lifetime of OMIECs devices. This includes mass transport engineering, reduced electron transfers kinetic or tuning the electronic densities of conjugated chains as shown in Figure 1.7. However, the issue of long-term device operation still remains, which limits the use of OMIECs in the high potential regime.

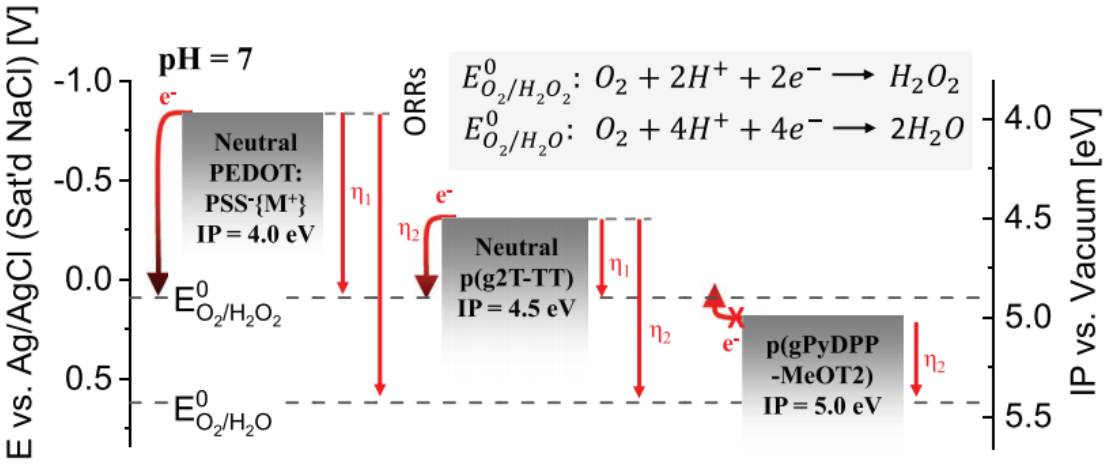

Figure 1.7. The potential levels of some OMIECs materials with respect to ORRs potentials[10,14]

1.3 Operating principle of organic electrochemical transistors (OECTs)

The configuration of organic electrochemical transistors (OECTs) is similar to that of organic field-effect transistors (OFETs), as shown in Figure 1.8. Both consist of channel materials, source, drain, and gate electrodes. Additionally, the working principle of OECTs shares similarities with OFETs, where the modulation of channel conductance can be achieved by applied gate potentials[12,13,15–17]. However, OECTs differ from OFETs with an aqueous electrolyte between the channel and gate instead of a conventional dielectric with dipoles. This distinction is one of the defining features in OECTs, responsible for their unique electronic properties.

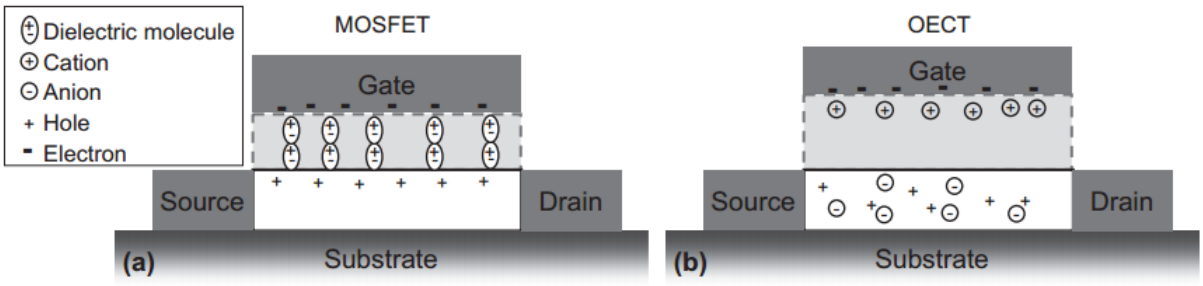

Figure 1.8. Comparison between MOSFET (OFET) and OECTs. The use of capacitance layer signifies the differences in their electronic properties.

The operation principle of OECT can be summarized in Figure 1.9a, where the channel conductance of the channel materials, such as PEDOT, can be modulated by mobile ions in the electrolyte. This doping or dedoping process allows for depletion-mode transistor operation, which results in a smaller channel current at higher gate biases. Therefore, in addition to the conductivity of the channel materials, volumetric capacitance (C*, F/cm^3) plays a critical role in the figure-of-merit of OECT performance, as indicated in the inset of the derived equations. Therefore, one of the main advantages of OECTs is their superior volumetric capacitance compared to the interfacial capacitance of MOSFETs (with a value that is three orders of magnitude higher than state-of-the-art k values), which demonstrates their potentials for signal amplification by enhanced value of transconductance (g_m) in Figure 1.9b.

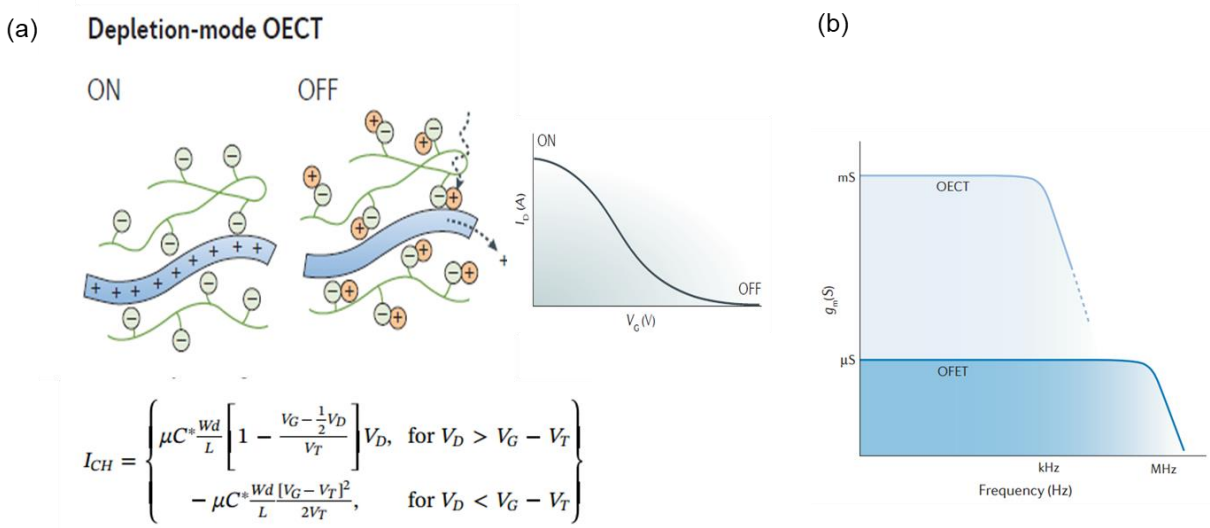

Figure 1.9. Operating principle of OECTs. (a) The doping and dedoping by mobile ions from the electrolyte modulated the electronic properties of channel materials[12]. The channel materials conductance has been modulated under principle of MOS transistor but further modified with volumetric capacitance (C*). (b) Merit of OECTs in transconductance gm brough by the volumetric capacitance[12].

The in-depth understanding of OECTs operation can be explained by the Bernards model (Bernards et al, 2007)[18]. In Figure 1.10a, the device can be divided into two circuits: an ionic circuit that describes the mobile ions penetrate bulky channel materials under gate bias, and an electronic circuit that describes electronic charge transportation between source and drain electrode. Furthermore, the ionic circuit can be divided into two in-series capacitors and a resistor, representing the ions storage in the gate/channel material and the electrolyte conductivity, respectively. When the gate and channel materials under their capacitive potential regime (without redox reaction occur), this model will suggest a purely capacitive process in which ions injected into the channel do not exchange charges with the films, but rather electrostatically compensate for the presence of opposite charges or supplied from the resistor circuit built upon source and drain electrodes, hence reflecting the change in electronic conductance by source-drain current. Therefore, this model provides the basic physic of device operation and its form factors (device

dimension $\frac{Wd}{L}$, gate bias V_g, source-drain bias V_d, channel mobility μ and turn-on voltage V_T) under the aqueous electrolyte as capacitance layer.

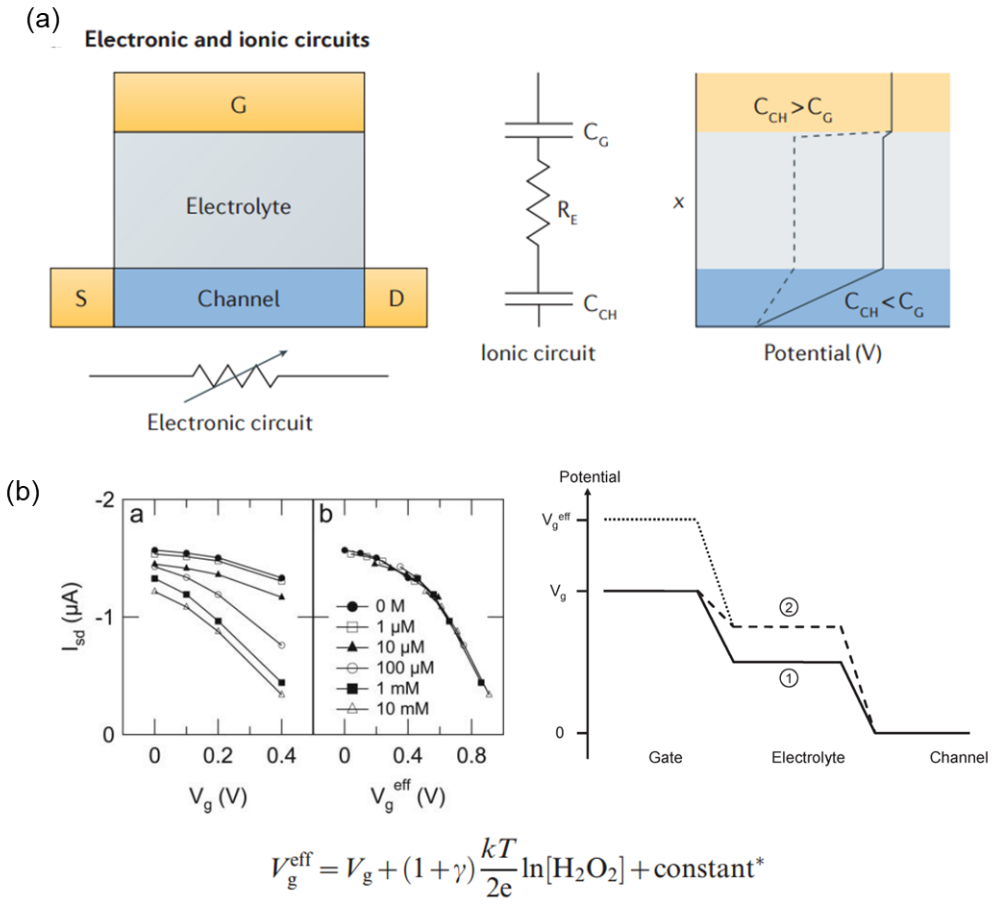

$$V_g^{eff} = V_g + (1+\gamma)\frac{kT}{2e}\ln[H_2O_2] + \text{constant}^*$$

Figure 1.10. Simulated circuits diagram for OECTs. (a) OECTs operation has been simulated in two divided circuits: ionic circuit and resistor circuit[16]. (b) Modified gate potentials as function capacitance ratio (γ) and targe ions concentration (H_2O_2 as example from ref[19].)

One of important application in OECTs is used as biosensors, where the focus is on detecting target ions in the electrolyte after modifying the gate electrode with various receptors[ref]. The channel conductance of OECTs with respect to the concentration of target ions has been derived by introducing the concept of effective voltage (V_{eff}) based on Bernards model[19] summarized in Figure 1.10b. The V_{eff} has been characterized to be a modified term of gate bias V_g as shown inset. The V_{eff} has been further explained as function of capacitance ratio of gate and channel (γ) and

Nernst relationships ($\frac{kT}{2e} ln\alpha, \alpha$ is an activity coefficient, representing the differences of solute concentrations). This principle delivers the device behavior under different target ions concentration and the effect brough by the device dimensions. Other factors in OECTs operating like device structure[15,17,20], ions effect[12,21,22] or fabrication[13] can be derived or modified from the principles and models mentioned above.

1.4 Introduction of organic infrared retinomorphic photodetector

Motion detection is a critical aspect of applications such as autonomous navigation, industrial automation, security, and environmental monitoring. However, conventional sensors, such as charge-coupled device (CCD) cameras, operate at a predetermined frame rate, and this results in gathering redundant data that slows down signal processing[23,24]. To enable efficient motion tracking, researchers are looking for an alternative to frame-based sensing by developing event-driven devices that are inspired by biological retinas, as shown in Figure 1.11. Many photodetectors have been fabricated to be an array, and many works have focused on post-signal treatment to achieve neuromorphic prototypes that can integrate multi-signal processing and receive signals simultaneously.

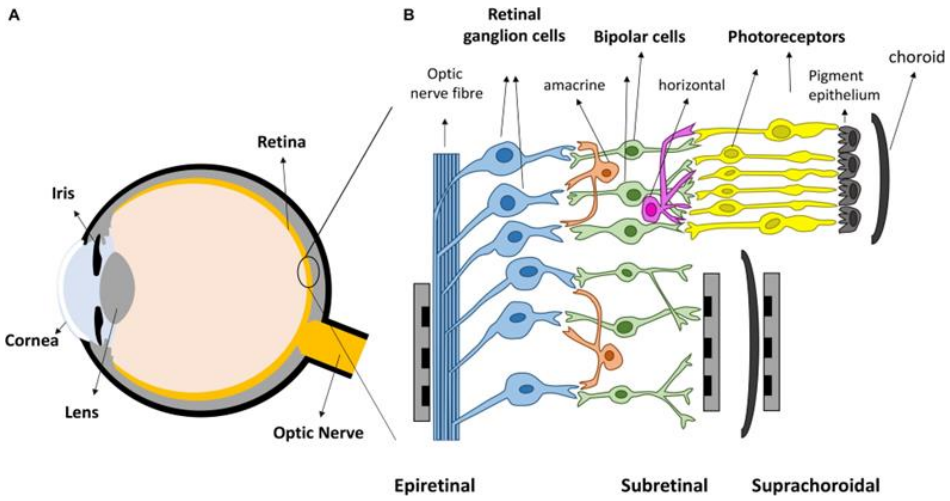

Figure 1.11. Human retina and eye nerves[25].

Although sensors based on the retinomorphic concept have been extensively developed since the 1980s[23], a compact organic prototype design based on this concept was recently achieved by Labram et al. in 2020[26]. The schematic of device configuration and features are summarized in Figure 1.12.

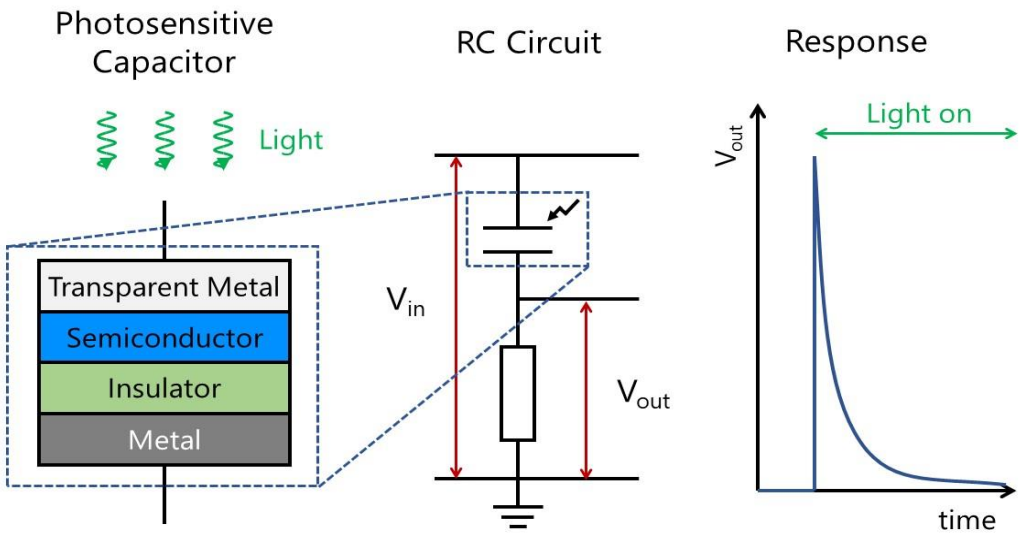

Figure 1.12. The compact design of organic retinomorphic sensor and its electrical feature.[26–28]

The organic retinomorphic device is composed of a photosensitive bilayer capacitor in series with a conventional resistor as typical resistor-capacitator (RC) circuit, illustrated in Figure 1.12. The voltage applied across the device is defined as V_{in}, while the voltage dropped across the capacitor and resistor are V_C and V_{out}, respectively. When the photosensitive capacitor is exposed to illumination, the change in reactance leads to a displacement signal on the V_{out} output. Hence, the organic retinomorphic device is designed to respond only to changes in illumination conditions instead of prolonged, persistent light responses as conventional photodiode operating.

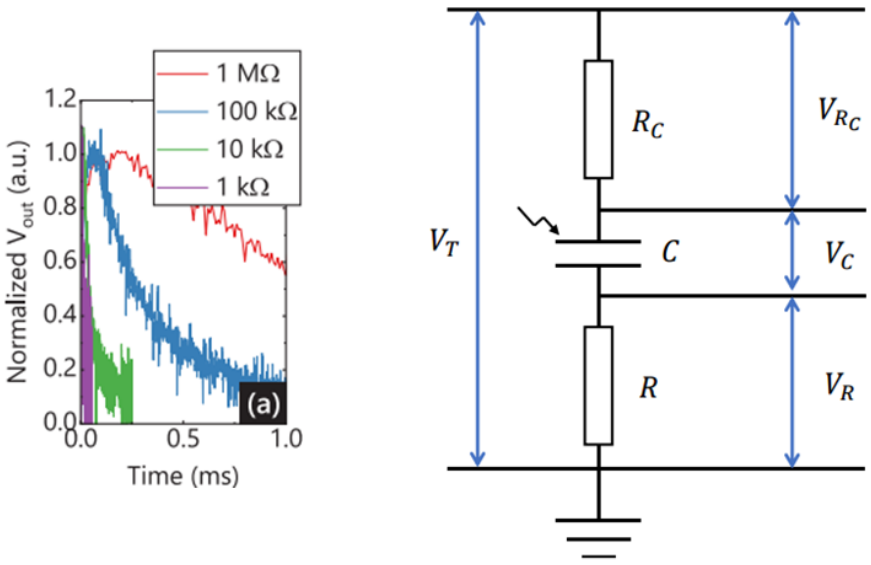

Figure 1.13. High-pass RC filter model in retinomorphic sensor. ΔP=124 mW/cm^2

The model of retinomorphic sensors is attempted to be extracted from device response by different external resistor as shown in Figure 1.13. It has been found that the RC time constant (τ) and the amplitude of V_{out} are dependent on the value of the external resistor. The detailed model for this finding has been developed based on the voltage divider assumption in the RC circuit[26,27] diagram shown in Figure 1.13.

$$V_R = \frac{R}{(R + R_c)}(V_T - V_c)$$

These simple models illustrate the operating principle of the organic retinomorphic sensor and its relationship with an external resistor (Please note that the notation used in this context is different from the one used previously. In this case, V_R refers to the output voltage across the external resistor, as defined by the cited references. However, it should be noted that V_R has a similar meaning to V_{out} in the previous texts, along with some other parameters). Previous studies have attempted to extract models describing the relationship between the retinomorphic sensor and light

illumination[26]. The device's response to a pulse of light signal has been recorded, and the signals selected from the transition of on to off or off to on have been summarized in Figure 1.14.

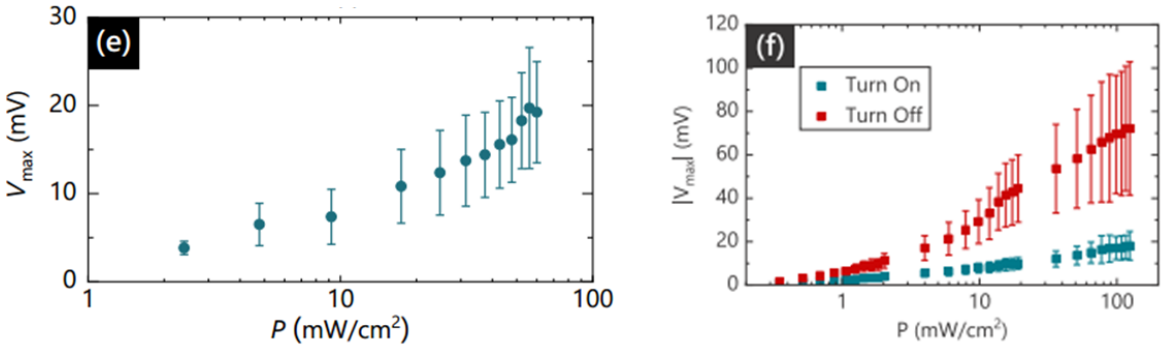

Figure 1.14. The signal output of organic retinomorphic device to light intensities[26]

The further modifications on the previous simple relationship have been summarized[26] here.

$$V_{max} = V_{in}\left(\frac{\alpha_0 P^{\gamma}}{C_D + 2\alpha_0 P^{\gamma}}\right)$$

where V_{max} is signal output (same as V_R, V_{out} in the previous texts), V_{in} is an applied voltage across the whole circuit, α_0 and P^{γ} is a fitting parameter and C_D is a capacitance in the electrical insulation layer. Although this relationship can extract similar report values of γ in agreement with most works on perovskite layers, it was also found incapable of fitting other organic photosensitive layers[27] and which requires further investigation in the future. The capacitance of the device (C_D) might also be affected by light illumination since it is possible that C_D is not simply a separate capacitor layer, but rather a function of light illumination, and therefore cannot be treated separately from the $\alpha_0 P^{\gamma}$ term in the assumptions. The operation of the retinomorphic device with its structure is illustrated in Figure 1.15. This schematic illustrates the charges within the device structure and the flow of charges in the external circuit during a pulse of light. It provides an explanation for the features of the retinomorphic device, such as the asymmetric signals during the

edge of the light pulse. It also presents the principle that the device's response is dependent on the carrier lifetime within the device or structure. Overall, this illustrated schematic provides an explanation for most of the electrical characteristics. However, further discussion and research are needed to fully understand and analyze the behavior of the device.

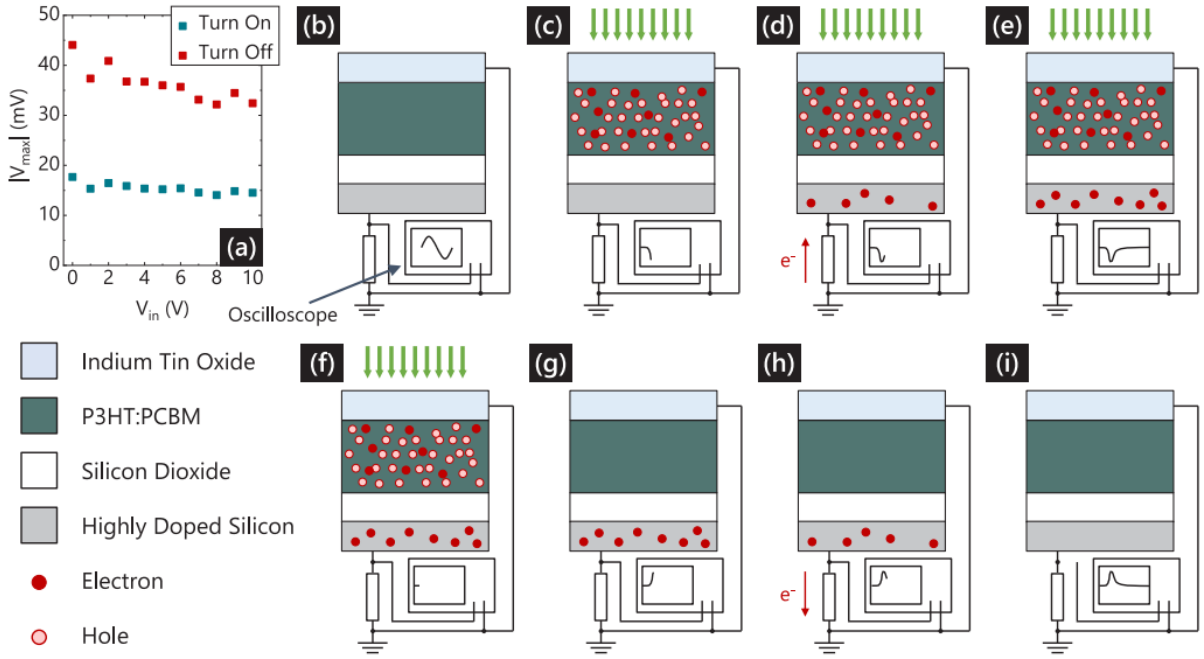

Figure 1.15. Schematics of charges movement in retinomorphic sensor during a pulse of light[27]

Other studies have also investigated the characteristics of organic retinomorphic sensors, such as rising/falling time and stability[27]. These sensors have shown potential for motion detection under visible spectrum, as demonstrated in Figure 1.16. The proposed sensor only captures and reflects the images of the moving subjects and served a great potential in the future applications.

Figure 1.16. The use of retinomorphic sensor on the moving vehicle. It only reflects the image of moving subjects[26].

CHAPTER 2: DUAL-GATE ORGANIC ELECTROCHEMICAL TRANSISTORS FOR MARINE SENSING

2.1 Challenges of OECTs in high potential regime.

Organic electrochemical transistors (OECTs) offer several advantages of signal amplification, biocompatibility and flexibility. Upon incorporation of redox species or selective membranes, OECTs demonstrate the selective detection of target ions in aqueous environments with remarkable sensitivity. However, some sensing functionalities require high driving redox potential, which may inherently change the chemical composition of the semiconductor within the channels and further degrade device performance. It is an ongoing effort to propose novel structure of semiconducting components that enable the effective modulations while maintain high operating stability. In current technology, the most common channel materials used in OECTs operation is poly(3,4-ethylenedioxythiophene) polystyrene sulfonate (PEDOT:PSS), which already demonstrated its superiority in the figure-of-merits performances of OECTs. We take oxygen reduction reaction as one of redox reactions requiring high operating potential that is incompatible with current OECTs technology. In high potentials, reactive oxygen species will take place and alter the structure of PEDOT:PSS[29].

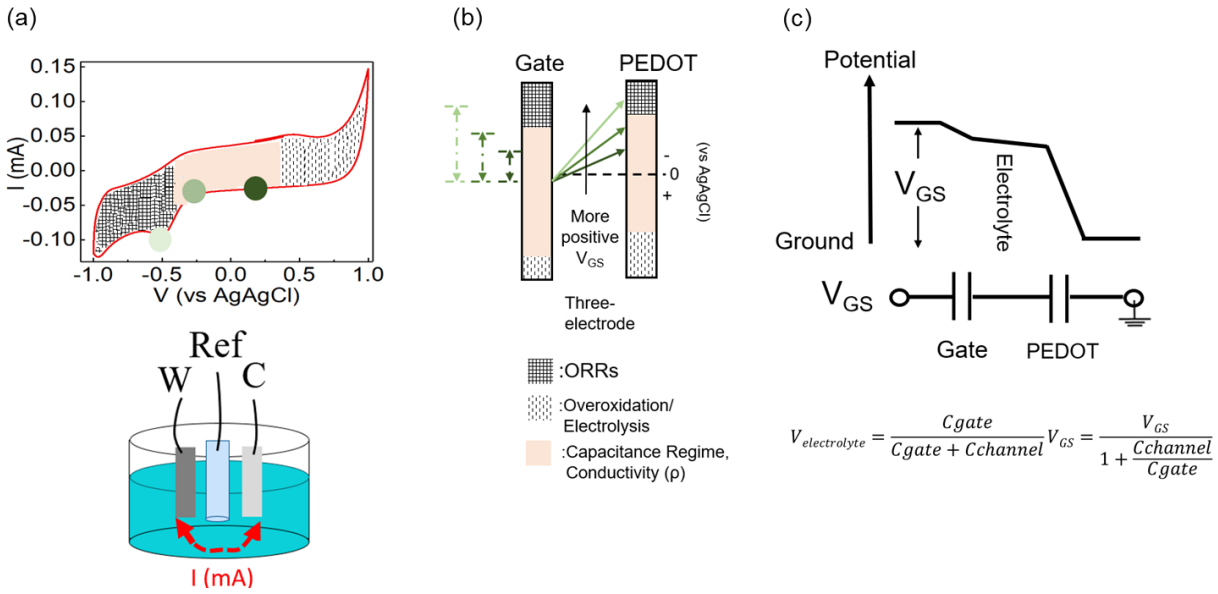

Figure 2.1. Electrochemical properties of PEDOT films (a) cyclic voltammetry of PEDOT films under seawater electrolyte. The region for overoxidation, ORRs or capacitance regime in different operating potential (vs Ag/AgCl) has been marked. (b) Potential diagrams of gate electrode and PEDOT channel. The electrochemical behavior of PEDOT channel with respect to operating potentials (applied gate biases) has been draw. (c) Potential relationships under gate and channels.

In Figure 2.1a, PEDOT films was fabricated on the graphite foils and carried out cyclic voltammetry (CV). Different electrochemical behavior of PEDOT has been found in the range of operating potentials. In brief, when applying a working voltage higher than 0.35 V (vs Ag/AgCl), overoxidation occurs on the PEDOT film, causing a similar composition alternation as mentioned earlier. Applying more negative potentials than -0.45V leads to ORRs on the surface of the PEDOT film, resulting in the irreversible change of morphological properties of the film. Thus, the stable operating potential range of the conjugated PEDOT:PSS film can be found between -0.4 and 0.35 V, denoted by the capacitive regime (light red color). This principle can also be applied to the operating principle of OECTs. The gate bias can now modulate the working potential of organic PEDOT channels, with the gate electrode playing the role of the reference Ag/AgCl electrode in CV. This allows for modulation of the electrochemical behavior of PEDOT channels and leads to different conductance as basic operating principle of OECTs. Similarly, the electrochemical

stability of PEDOT channel can also be modulated through applied gate bias as shown in Figure 2.1b. For instance, when the gate bias is shifted from zero to a more negative value (from dark green to light green), the electrochemical behavior of PEDOT changes from capacitive to ORRs regime, with a working potential ranging from 0.25 to -0.5 V. Meanwhile, the electrochemical potential of the gate electrode (vs Ag/AgCl) remains almost constant. These findings are based on the common architecture of OECTs, which shows that the capacitance of the gate electrode plays a dominant role in effectively modulating the electrochemical state of the channel, resulting in superior device performance. The schematic of electrochemical potential of gate and channel under one applied gate bias has been summarized into the Figure 2.1c. The ionic circuit is built using two parallel capacitors connected through a highly conductive electrolyte with the source electrode (one side of channel) acting as the ground. The capacitors are formulated as double-layer capacitance formed on the surface of the gate electrode or channel, depending on factors such as morphology, electrode area and ionic species. Therefore, the electrochemical potential of gate or channel can be easily derived by the proportional voltage drop in each component, as a result in the capacitance ratio between channel and gate. This principle predicts the operating voltage window and stability of OECTs while characterizing the electrochemical state of the PEDOT channel. As a result, PEDOT channel during the OECTs operation has great chance to suffer degradation (undesirable side reaction), especially applied by the high gate bias as most of effective gate bias ($V_{electrolyte}$) onto channels by the extreme small capacitance ratio ($C_{channel}/C_{gate}$). It is a continuous effort to propose a new molecular structure with wide electrochemical potential window[30–32], alternating composition of electrolyte[33], device dimension design or simply operating with low gate bias within materials capacitive regime. However, these limitations hinder the operation of OECTs for high potential regime applications.

2.1.1 Device configuration

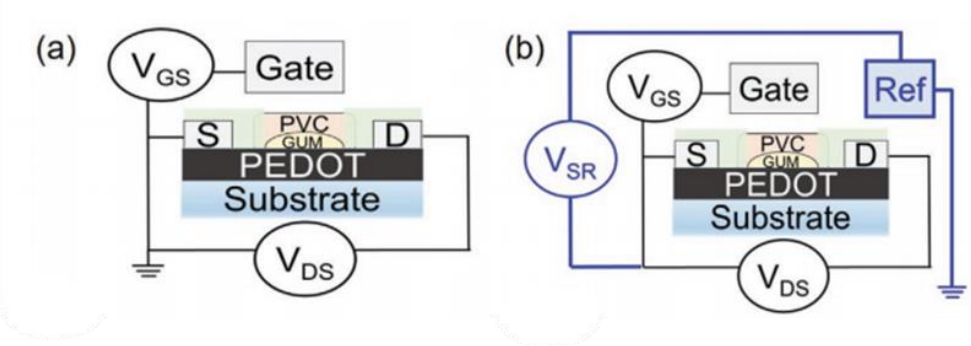

Figure 2.2. The device architecture of (a) conventional and (b) dual-gate OECTs

In this work, we propose a dual-gate configuration for OECTs, as depicted in Figure 2.2, in order to overcome the limitations of the conventional OECT structure. The device fabrication and experimental details are summarized in the following sections. In typical OECTs, it has three electrodes (gate, source, and drain), in which the source electrode serves as the ground. The potential across drain and source electrode was supplied by V_{DS} and gate bias by V_{GS}. In dual-gate configuration, the fourth electrode was added and served as the ground, supplied by additional power supply V_{SR}. Those electrodes and channel share the same conductive electrolyte (seawater). Consequently, the operating of this novel dual-gate OECTs is controlled by three input voltages (V_{DS}, V_{GS} and V_{SR}). Thus, the conductance of PEDOT channel is now modulated by both gate and reference gate through V_{GS} and V_{SR}. Those electrical characterization details and operating principle would be introduced in the next section.

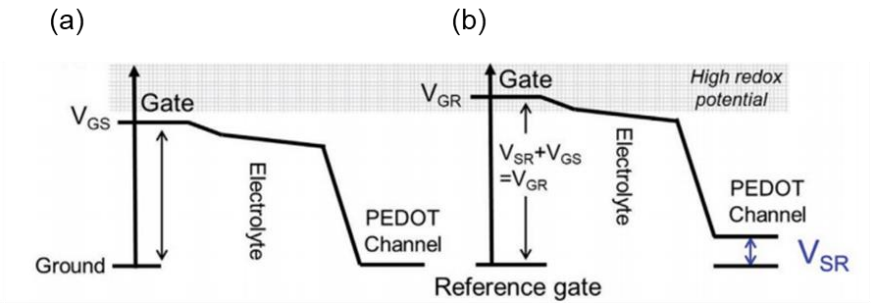

Figure 2.3. Operating potential diagram of (a) conventional OECTs or (b) dual-gate OECTs

The schematic of operating potential diagram for both configurations are displayed in Figure 2.3. The role of V_{GS} is served to control the electrochemical state of channel as shown in Figure 2.3a under the principle of capacitance ratio relationships. In order to induce a high redox potential on the gate for performing sensing functionality, it is conceivable to apply a higher V_{GS}, either negative or positive depending on the desired electrochemical redox reaction. However, giving the extreme small capacitance ratio (10^{-3} and less), it requires tremendous V_{GS} to induce electrochemical state of gate occur in high redox potential regime, which is unavoidable to cause severe damage to channels. The role of V_{SR} in the dual-gate configuration has been clearly demonstrated as a ‘’step’’ in the form of operating potential diagram shown in Figure 2.3b. The electrochemical potential of gate and channel is now with respect to a new ground point, which is served by new added fourth electrode (reference gate). Therefore, the electrochemical potential of channel is still governed under the gate bias V_{GS} while the electrochemical state of gate and channel is adjusted accordingly with new input variable V_{GR} ($=V_{GS}+V_{SR}$) or V_{SR}, respectively. In this new guideline, gate potential can reach into high redox potential regime while the electrochemical state of channel is controlled mainly under applied V_{SR}. In this work, we inherently interpret the high redox potential as oxygen reduction reactions (ORRs) and employ them for detecting levels of dissolved oxygen in seawater in the following sections.

2.2 Device fabrication and electrodes fabrication

We propose a novel and simple technique to develop OECTs and dual-gate OECTs by stencil printing.

OECTs Fabrication:

Glass substrates were cleaned by sonication in isopropanol and then in acetone. Kapton tapes were used as stencil masks to define the channel and electrode dimensions. PEDOT:PSS (Clevios P1000) was spin-coated onto the mask-covered substrate at 2000 rpm. After removing the stencil mask, the PEDOT:PSS film was annealed at 120 °C for 30 min. Subsequently, the film was immersed in concentrated sulfuric acid for 15 min to remove PSS, followed by rinsing with deionized water for three times to remove the residual acid. Silver/silver chloride ink (Ercon part #E2414) was deposited onto the PEDOT film to define source and drain electrodes. Silicone (Ecoflex) was stencil printed to encapsulate the electrodes and define the channel dimensions to be 1 cm in width and 0.2 cm in length. After the silicone has completed crosslinking, the xanthan gum electrolyte was drop-cast onto the defined channel area. A piece of the PVC-based membrane was placed over the channel area and pressed onto the electrolyte. Finally, silicone was applied again to seal the membrane edge.

ORRs Catalysis and Electrodes Fabrication

The Pt-C gate electrode was fabricated by electrodepositing a small amount of platinum on the conductive carbon cloth (AvCarb MGL190). A commercial Pt carbon cloth (FuelCellStore, 0.3 mg cm^{-2} 40% Pt) was used as the Pt source. It served as the working electrode to which potential cycles were applied versus Ag/AgCl, and the carbon cloth was the counter electrode. The potential cycles were swept from 1.2 to 0.8 V for 30 times in aqueous electrolyte made from Instant Ocean, and Pt was found to be incorporated into the counter carbon cloth electrode. For the reference

electrode, AcC was selected because it was more stable than Ag/AgCl in marine environments. The AcC slurry was prepared by mixing activated carbon powder (Kuraray Chemical, YP50F) and polyvinylidene fluoride binder at 9:1 weight ratio. The mixture was added to N-methyl-2-pyrrolidone solvent to reach 60–70% solid content by weight. Then, the slurry was evenly deposited onto the carbon cloth and annealed at 80 °C for 1 h. The two gate electrodes were attached adjacent to the PEDOT channel to complete the OECT. The gate electrode dimensions were 1 cm × 0.5 cm.

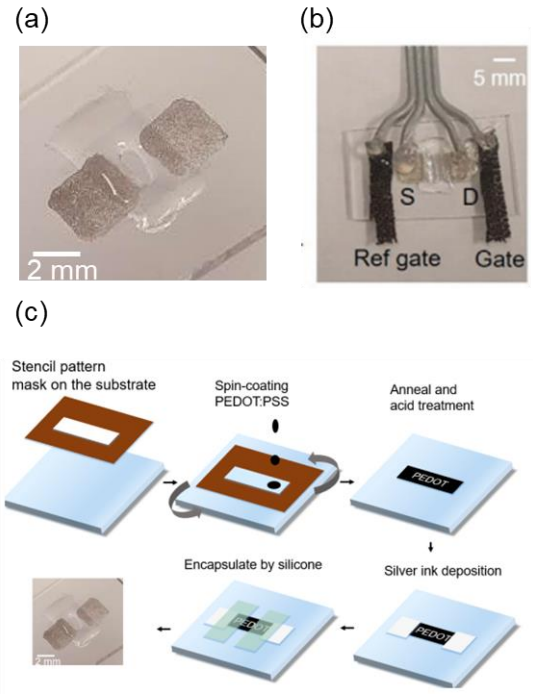

Figure 2.4. OECTs fabrication. (a) The deposed channel by stencil printing technique. (b) Dual-gate OECTs with gate and reference gate. (c) Flow in OECTs fabrication

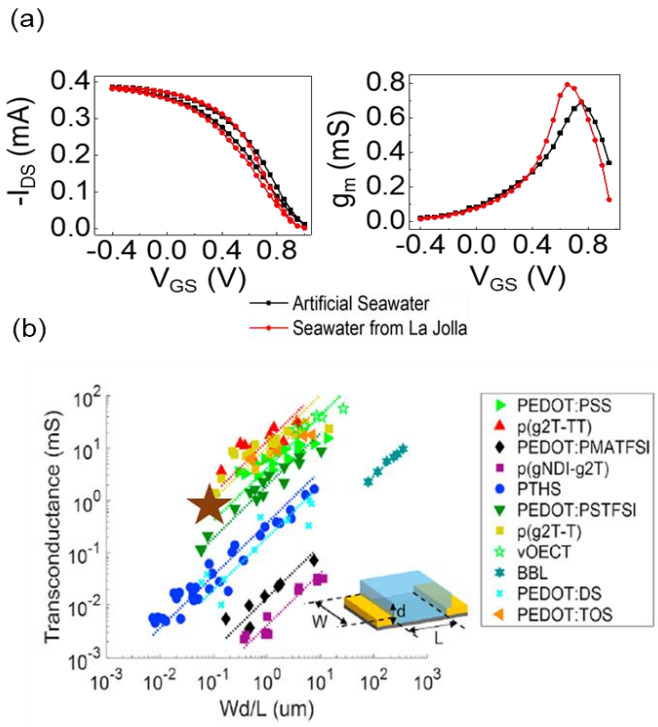

Figure 2.5. Performance of fabricated conventional OECTs by stencil printing. (a) OECTs transfer characteristics. Black line represents the device working under artificial seawater. Red line represents the one under actual seawater taken from La Jolla Cove (b) Performances of conventional OECTs by stencil printing technique (brown star) comparison with other works[16].

Xanthan Gum Electrolyte and Polyvinylchloride (PVC)-Based Membrane Preparation

The chemicals were purchased from Sigma-Aldrich and used as received, unless noted otherwise. The xanthan gum electrolyte was prepared by dissolving 5 g xanthan gum powder in 50 mL of 1 m sodium sulfate aqueous solution. The PVC-based cocktail membrane was prepared based on a formulation in ref.[33] but excluding the hydrogen ionophore. The mixture consisted of 1 mL tetrahydrofuran, 59 mg of 2-nitrophenyl octyl ether, 29.5 mg of PVC, 0.44 mg of sodium tetrakis[3,5-bis(trifluoromethyl)phenyl]borate, and 10.3 mg of tetrakis(4-chlorophenyl)borate tetradodecyl-ammonium salt (ETH 500). The solution was drop-cast onto a glass slide and allowed to dry over a day, to form stand-alone thin films that would be transferred onto OECT channels.

2.3 Electrical characteristics and behavior

The electrical characteristics of conventional OECTs and dual-gate OECTs, their dependence on dissolved oxygen levels, and the instability of OECTs have been summarized in the three sections below.

2.3.1 Electrical characteristics of OECTs or dual-gate OECT

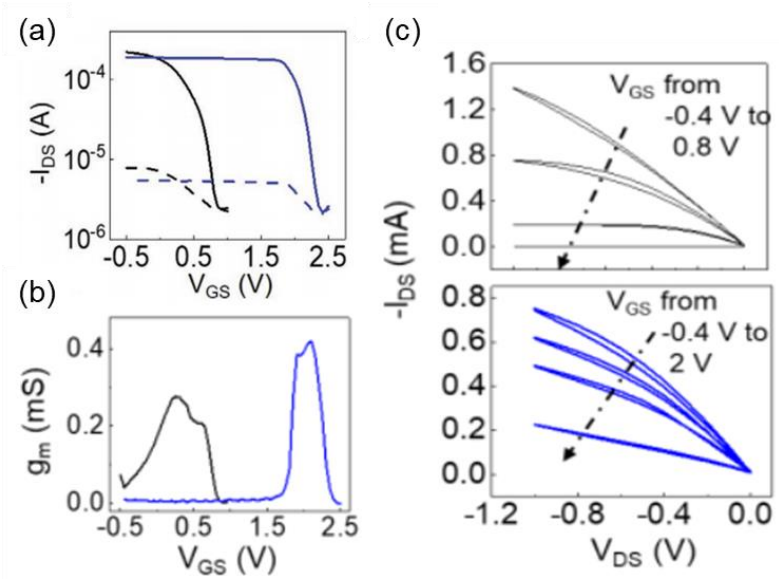

Figure 2.6. Electrical characteristics of OECTs (black) and dual-gate OECTs (blue). (a) Transfer characteristics. (b) Transconductance (g_m). (c) Output curves

Typical electrical characteristics have been carried out for both structures in Figure 2.6. In conventional OECTs with PEDOT as the channel and Pt-C carbon cloth as the gate, it operates in depletion mode. In this mode, a positive V_{GS} induces cations to migrate inside the semiconducting film, causing PEDOT to de-dope and reducing its conductance as shown in Figure 2.6a-c with black curves. In the dual-gate OECTs with V_{SR}=0 V, they exhibit typical depletion behavior like conventional OECTs. However, with V_{SR}=-0.6 V, the threshold voltage (V_T) can be effectively shifted from 0.8 to 2.4 V as blue curves in Figure 2.6a-c. The carrier mobilities were derived to be ~2 $cm^2V^{-1}s^{-1}$. The leakage current (I_{GS}) for both structures is approximately 2 orders of magnitude

smaller than I_{DS}, clearly indicating the electrical behavior of dual-gate OECTs has been effectively modulated by the gate and reference gate.

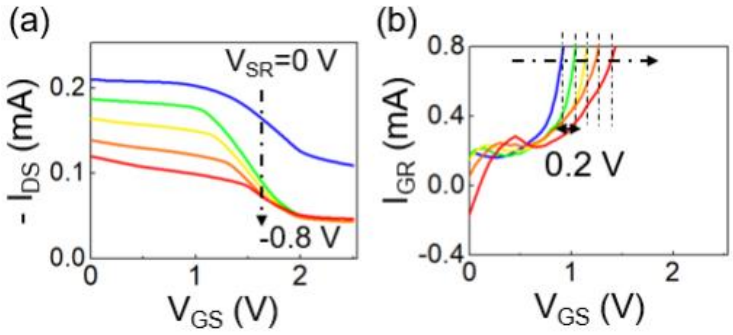

Figure 2.7. The (a) I_{DS} or (b) I_{GR} of dual-gate OECTs in different V_{SR}

The I_{DS} dependence with V_{SR} has been summarized in Figure 2.7. Transfer characteristics of a dual-gate OECT are recorded with varied V_{SR} from 0 to -0.8 V. A slight change of V_T due to the voltage of transition point becomes more positive as more negative V_{SR} applied. Interestingly, the transition point is a function of the gate overoxidation onset potential, in related with the I_{GR} (current between gate and ref gate) verse V_{GS} shown in Figure 2.7b. In a dual-gate OECT, V_T became the function of the gate oxidation potential, controlled by V_{SR} in term of V_{GR} ($V_{GR}=V_{GS}+V_{SR}$), not limited by the channel capacitance. The p-type behavior in the extended V_{GS} indicates that the channel conductance is still modulated by different gate redox state, and range of gate potentials have been successfully expanded by the reference gate. This demonstrates a design principle that the figure-of-merits of OECTs can be further optimized by the redox state of the dual gate, independent of the intrinsic properties of the channel.

2.3.2 Failure conventional OECTs operation in high redox potential regime

The issues for conventional OECTs operated under the high potential regime (ORRs) have been carefully analyze through transfer characteristics. The deposited PEDOT films have demonstrated

its dependence on different level of dissolved oxygen (DO) with working voltage over -0.4 V (*vs* Ag/AgCl) by CV in Figure 2.8a. Similarly, in the operation of conventional OECTs, V_{GS} was set to 0.4 V with V_{DS}=-0.2 V, resulting in a sensitivity of 11.3 μA/ppm-cm^2 in the dissolved oxygen (DO) range of 2-12 ppm as shown in Figure 2.8b. This dissolved oxygen dependence is not in the category of high redox potential regime defined in the earlier section. Instead, the operating OECTs shall be biased away from the regime and thus reducing the interferences from channels overoxidation when the gate electrode (Pt-C) performs DO detection.

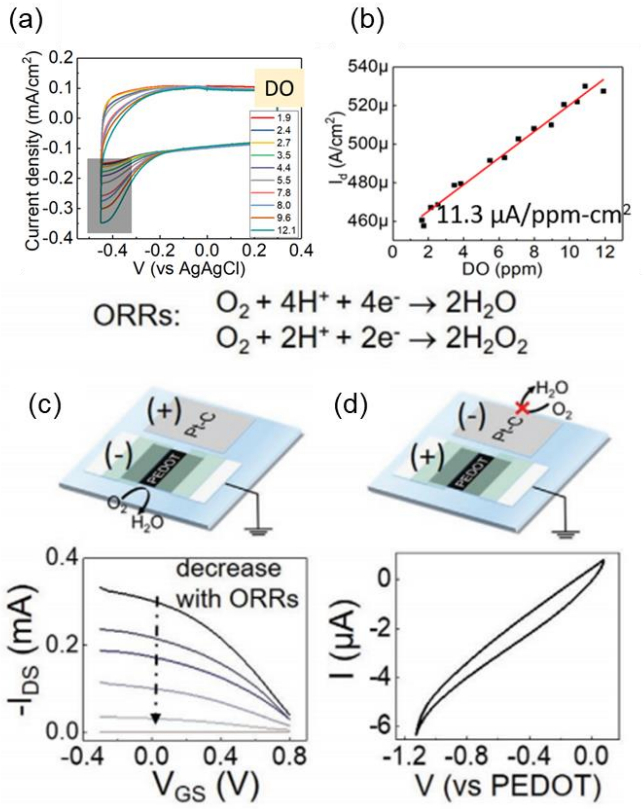

Figure 2.8. PEDOT films relationships with dissolved oxygen. (a) CV of PEDOT films in dependence with DO (ppm). (b) A calibration curve of DO under conventional OECTs operation. (c) Transfer characteristics after biasing under V_{GS}=0.8 V for 200s. (d) ORRs not occurring on gate, as indicated by the low redox current. The drawings show the applied voltage polarity. The dissolved oxygen concentration was ≈6 ppm.

However, we observed poor cycling stability of PEDOT films during DO detection as shown in Figure 2.8c. After biasing under V_{GS}=0.8 V for 200s, the transfer characteristics (with V_{DS}=-0.2

V) was performed. It clearly shows the decaying conductance of PEDOT channel until its conjugated properties was loss. Hence, Pt-C gate was attempted to be utilized in the role of DO detection, in other words, used to perform ORRs during OECTs operation. Yet, as shown in Figure 2.8d, the capacitance ratio of Pt-C and PEDOT channels (smaller than 10^{-3}) leads to poor control of ORRs reaction occurring onto the Pt-C. As clear evidence, the redox current is too small to allow for the detection of dissolved oxygen, even though a potential of over 1.2 V was applied between Pt-C and PEDOT channel (similar to V_{GS}).

2.3.3 Dual-gate OECTs in high potential regime (ORRs)

We have demonstrated the capability of dissolved oxygen detection in dual-gate OECTs by inducing ORRs in Pt-C gate while modulating PEDOT channel within the capacitive regime. The conductance of PEDOT channel is responding to different levels of dissolved oxygen as receiving I_{DS} in Figure 2.9a. Before delving into the signal amplification form dual-gate OECTs, we first extrapolate the relationship between Pt-C gate and AcC reference gate in Figure 2.9b. Their dependence on the levels of DO would serve a critical role in dual-gate OECTs operation. The onset potential of ORRs occurrence has been found at ~-0.9 V, as two terminal electrodes system that Pt-C serves as working electrode and AcC as counter/reference electrode. The role of I_{GR} and V_{GR} is simply a redox current and working voltage of Pt-C with respect to AcC ground point. In dual-gate OECTs operation with V_{SR}=-0.6 V, the transfer characteristics in Figure 2.9c demonstrates that the I_{DS} increases with increasing DO concentration in V_{GS} more negative than -0.3 V. The value of V_{GR} [-0.9 =(-0.3,V_{GS})+(-0.6,V_{SR})] is corresponding to the ORRs potential found in Figure 2.9b. The receiving I_{DS} current has also shown corresponding increment than increment of I_{GS}. In conclusion, the combination of the Pt-C gate and AcC reference electrode acts as a single functional "gate" electrode in conventional OECTs, where their redox behavior can be

amplified by doping/dedoping of the deposited channel, leading to different conductance levels. As a result, by using a combination of different electrode systems, it is possible to induce almost any high redox potentials reactions and amplify the resulting signals through the already developed conventional OECTs architecture.

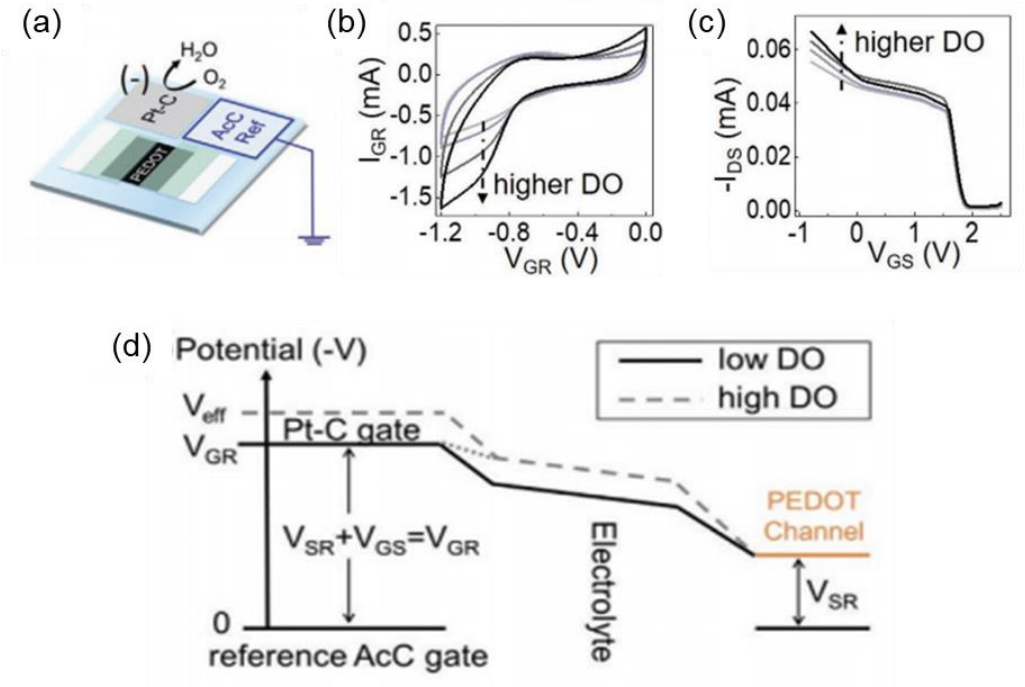

Figure 2.9. (a) ORRs occur on the dual-gate OECTs. (b) Redox current (I_{GR}) between Pt-C and AcC reference (ground). (c) Transfer characteristics of dual-gate OECTs with V_{SR}=-0.6 V in different level of DO. (d) Schematic potential diagram.

The operating principle of dual-gate and PEDOT channel has been displayed in the form of potential diagram illustrated in Figure 2.9d. The channel potential can be placed at a level between the gates as the orange level set by V_{SR}. While the applied voltages V_{GS} and V_{SR} are independently adjustable, they add up to V_{GR} which determines whether the Pt-C electrode would undergo ORRs as we have some preliminary evidence in transfer characteristics.

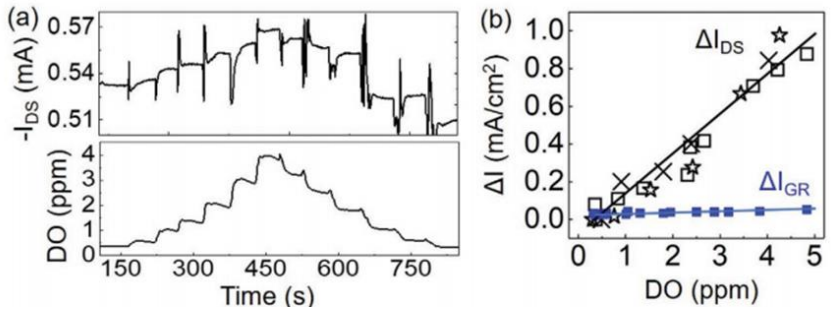

Figure 2.10. Dual-gate OECTs responses in dissolved oxygen. a) Top: I_{DS} of the dual-gate OECT in seawater, as the dissolved oxygen concentration was varied. Bottom: corresponding measurement by the commercial calibration probe. (b) Sensor calibration curve measured at $V_{GS} = -0.3$ V, $V_{SR} = -0.6$ V, and $V_{DS} = -0.2$ V for three different devices, each with a different symbol. The black and blue colors represent the I_{DS} (222 µA cm^{-2} ppm^{-1}) and I_{GR} (5.7 µA cm^{-2} ppm^{-1}) responses, respectively.

The real-time device response to DO concentration was further calibrated at fixed gate voltages. $V_{SR} = -0.6$ V was applied to keep the PEDOT channel below the ORRs onset potential and prevent over-oxidation in the PEDOT channel; $V_{GS} = -0.3$ V was used to bring the total potential on the Pt-C gate to $V_{GR} = -0.9$ V, to induce ORRs that modulated I_{DS}. Figure 2.10a shows the dual-gate OECT repetitive response as a function of dissolved oxygen concentrations over time. The oxygenation level of the seawater sample was concurrently monitored by a commercial meter (Hanna model #HI98194) and was varied between 0.3 to 4 ppm by bubbling oxygen or nitrogen gas into the seawater. Figure 2.10b presents the dual-gate OECTs I_{DS} versus dissolved oxygen concentration, and the ratio of current to analyte concentration determines the device sensitivity. The average sensitivity of the three devices is 222 µA cm^{-2} ppm^{-1} with deviations of ±12%. We reported the current change with the baseline current subtracted [ΔI = I (x ppm) – I (0 ppm)]. The detection threshold was measured to be 0.3 ppm, and the sensors showed super-Nernstian sensitivity higher than prior thin-film electrochemical sensors in Table 2.1. In other types of sensors, such as fluorescence quenching or switchable-trace-amount oxygen sensors, the readouts are amplified by integrated circuits and reached lower detection limits than our device but at the expense of large device volume. It is noted that the gate current I_{GR} in our devices was equivalent

to the current readout in other oxygen sensors based on conventional cyclic voltammetry. At its maximum the I_{GR} response was only 5.7 μA cm^{-2} ppm^{-1}, as shown in Figure 2.10b. By comparison, the I_{DS} sensitivity is 38 times better than the I_{GR} response, thus showcasing the benefit of channel modulation that enabled signal amplification in dual-gate OECTs.

Table 2.1. Electrochemical dissolved oxygen sensors with thin film form factors.

Working Electrode	Sensitivity	Response range	Detection limit	Electrolyte	Ref
Printed Au	42.5 μA/cm^2-ppm (0.03 μA/ppm)	0-8 ppm	0.11 ppm	KNO_3	(Moya, A. et al,2016)
Hermin/pyrrole	20.7 μA/cm^2-ppm (20.7 μA/ppm)	2-7 ppm	2 ppm	Tap water	(Hsu, L. et al,2014)
Platinum/nickle-salen polymer	49.86 μA/cm^2-ppm (3.54 μA/ppm)	3.95-9.2 ppm	0.71 ppm	KCl	(Martin, et al, 2012)
SiO_2/SnO_2/MnPc	4.6 μA/ppm	0.2-8.1 ppm	0.02 ppm (Calculated, not measured)	KCl	(Santos, et al, 2011)
Nanoporous gold	1.29 μA/cm^2-ppm (0.632 μA/%)	0-71.8 % (0-5.73 ppm)	2.83 % (0.23 ppm, converted)	KNO_3	(Sukeri, et al, 2015)
Dual-gate OECT	OECT amplification: 248 μA/cm^2-ppm (9.92 μA/ppm) Cyclic voltammetry: 5.74 μA/cm^2-ppm (5.74 μA/ppm)	0.3-4 ppm	0.3 ppm	Seawater	Our work

2.4 Equation derivations

In the dual-gate configuration, the effect of V_{GS} and V_{SR} on the channel source-drain current I_{DS} can be expressed by the following relations:

$$I_{DS} = \frac{Wd}{L}\mu C^*(V_T - V_{eff} + \frac{1}{2}V_{DS})V_{DS} \qquad \text{(Equation 1)},$$

$$V_{eff} = -V_{SR} + V_{GS}\frac{(1+\beta)}{(1-\beta\gamma)}\gamma - \frac{kT}{ze}\frac{(1+\beta)(1+\gamma)}{(1-\beta\gamma)}\ln Q_r + \text{constant}_2 \qquad \text{(Equation 2)},$$

where W is the channel width, d is the semiconductor thickness, L is the channel length, μ is the mobility, C* is the volumetric capacitance. The V_{eff} term is the effective bias on the channel, with dependence on the applied voltage levels V_{GS} and V_{SR} and the Faradaic reaction quotient Q_r that is proportional to the analyte concentration. The coefficient $\beta = C_{PEDOT}/C_{AcC}$ is the capacitance ratio of the PEDOT channel to the AcC reference gate, and $\gamma = C_{Pt\text{-}C}/C_{AcC}$ is the capacitance ratio of the Pt-C gate to the AcC reference gate. The parameter T is the temperature, k is the Boltzmann constant, e is the electron charge, and z is the number of electrons transferred in the redox reaction.

The two gate electrodes, Pt-C and AcC reference, apply different levels of gate modulation to the channel. The following derivation of Equation 2 was built upon References [18,19]. The potential shift of Pt-C due to Faradic reactions is represented by the Nernstian equation. The potential difference between the electrolyte and Pt-C can be expressed as:

$$E_{Pt\text{-}C} = \frac{V_{GR}}{1+\gamma} + \frac{kT}{ze}\ln Q_r + constant_1. \text{ (Equation 3)}$$

The potential difference between Pt-C and AcC is V_{GR}. Therefore the potential of AcC (denoted as E_{AcC}) will be the difference between V_{GR} and $E_{Pt\text{-}C}$:

$$E_{AcC} = V_{GR} - E_{Pt\text{-}C} = \frac{V_{GR}}{1+\gamma}\gamma - \frac{kT}{ze}\ln Q_r + constant_2. \text{ (Equation 4)}$$

With our dual-gate configuration, the potential difference between the PEDOT channel and AcC reference is V_{SR} (with the condition that V_{DS} is small compared to V_{SR}). We set the potential of PEDOT as proportional by a factor of (1+β) to the potential E_{AcC} (Equation 4):

$$\frac{V_{SR}}{1+\beta} = \frac{V_{GR}}{1+\gamma}\gamma - \frac{kT}{ze}\ln Q_r + constant_2. \text{ (Equation 5)}$$

Since $V_{GS} + V_{SR} = V_{GR}$, therefore

$$V_{SR} = (V_{GS} + V_{SR})\frac{(1+\beta)}{(1+\gamma)}\gamma - \frac{kT(1+\beta)}{ze}\ln Q_r + constant_2$$

$$V_{SR}(1 - \frac{(1+\beta)}{(1+\gamma)}\gamma) = V_{GS}\frac{(1+\beta)}{(1+\gamma)}\gamma - \frac{kT(1+\beta)}{ze}\ln Q_r + constant_2$$

$$V_{SR}\frac{1+\gamma-\gamma-\beta\gamma}{(1+\gamma)} = V_{GS}\frac{(1+\beta)}{(1+\gamma)}\gamma - \frac{kT(1+\beta)}{ze}\ln Q_r + constant_2$$

$$V_{SR}\frac{1-\beta\gamma}{(1+\gamma)} = V_{GS}\frac{(1+\beta)}{(1+\gamma)}\gamma - \frac{kT(1+\beta)}{ze}\ln Q_r + constant_2$$

An effective gate voltage (V_{eff}) is introduced to represent equivalent voltage needed to achieve same I_{DS} current in the absence of Faradaic effect:

$$V_{eff} = -V_{SR} + V_{GS}\frac{(1+\beta)}{(1-\beta\gamma)}\gamma - \frac{kT(1+\beta)(1+\gamma)}{ze(1-\beta\gamma)}\ln Q_r + constant_2,$$

which is the expression of Equation 2. This is for the range where $\gamma \leq 1$. This derivation clarifies the ratio of gate modulation from adjusting the voltages V_{GS} and V_{SR}. The capacitance ratios β and γ can be adjusted by tuning electrode dimensions or materials. Note that there are opposite signs in front of V_{GS} and V_{SR}, so they have opposite modulation effect on V_{eff}.

Similar to Equation 3, the potential difference between Pt-C and PEDOT is V_{GS}:

$$E_{Pt\text{-}C} = \frac{V_{GS}}{1+\alpha} + \frac{kT}{ze}\ln Q_r + constant_3.$$

The coefficient $\alpha = C_{PEDOT}/C_{Pt\text{-}C}$ is the capacitance ratio of the PEDOT channel to the Pt-C gate. From Equation 4, the electrolyte potential of AcC (E_{AcC}) would be equal to $E_{Pt\text{-}C}$ (with the condition that electrolyte resistance is relatively small):

$$\frac{V_{GR}}{1+\gamma}\gamma - \frac{kT}{ze}\ln Q_r + constant_2. = \frac{V_{GS}}{1+\alpha} + \frac{kT}{ze}\ln Q_r + constant_3$$

Since V_{GS} +V_{SR} =V_{GR}, therefore

$$\frac{(V_{GS}+V_{SR})}{1+\gamma}\gamma - \frac{kT}{ze}\ln Q_r = \frac{V_{GS}}{1+\alpha} + \frac{kT}{ze}\ln Q_r + constant_4$$

$$\frac{V_{SR}}{1+\gamma}\gamma - \frac{kT}{ze}\ln Q_r = \frac{V_{GS}}{1+\alpha} - \frac{\gamma}{1+\gamma}V_{GS} + \frac{kT}{ze}\ln Q_r + constant_4$$

$$\frac{V_{SR}}{1+\gamma}\gamma = \frac{(1+\gamma-\gamma-\alpha\gamma)}{(1+\alpha)(1+\gamma)}V_{GS} + 2\frac{kT}{ze}\ln Q_r + constant_4$$

$$\frac{V_{SR}}{1+\gamma}\gamma = \frac{(1-\alpha\gamma)}{(1+\alpha)(1+\gamma)}V_{GS} + 2\frac{kT}{ze}\ln Q_r + constant_4$$

An effective gate voltage (V_{eff}) is introduced to represent equivalent voltage needed to achieve same I_{DS} current in the absence of Faradaic effect:

$$V_{eff} = -V_{SR} + \frac{1+\gamma}{\gamma}\frac{(1-\alpha\gamma)}{(1+\alpha)(1+\gamma)}V_{GS} + 2\frac{1+\gamma}{\gamma}\frac{kT}{ze}\ln Q_r + constant_4 \quad \text{(Equation 6)}$$

The above Equation 6 is for the limit where γ >1. Note that the boundary limit for Equation 6 is a rough estimate, and the further validation efforts would be carried out in the future.

We further examine Equation 2 by assuming that the channel is modulated in the capacitance regime (then the Faradaic term could be discarded) and β is very small (β ~0.00045 was obtained from the EIS measurements in Figure 2.11a), such that the effective gate voltage can be simplified to the following:

$$V_{eff} = -V_{SR} + V_{GS}\gamma + constant_2, \quad \text{(Equation 6)}$$

Equation 6 denotes the modulation effect by the two gates when there is no Faradaic reaction. The relationship of V_{eff} and γ derived in Equation 6 can be confirmed through analyzing the measurements in Figure S3c. The transfer characteristics were recorded with V_{SR}= 0 V as V_{GS} was

varied (blue curve), and V_{GS}= 0 V as V_{SR} was varied (red curve) as shown in Figure 2.11b. The subthreshold slope of the blue curve (V_{SR}=0) is apparently smaller than the red curve (V_{GS}=0), indicating that the channel conductance is influenced less by the V_{GS} than by the V_{SR}, due to the factor $\gamma = C_{Pt\text{-}C}/C_{AcC}$ (the capacitance of the Pt-C gate is smaller than the AcC reference gate in our device as shown in Figure 2.11a).

The measured I_{DS} in Figure 2.11b were used to extract V_{eff} by Equation 1. In Figure 2.11b, the difference between every step change in the applied bias V_{GS} or V_{SR} was denoted as ΔV. Corresponding to each ΔV step, the difference in the extracted V_{eff} was calculated and plotted as ΔV_{eff}. In Figure 2.11b, the blue curve was $\Delta V_{eff} \propto \gamma \, \Delta V_{GS}$, while the red curve was $\Delta V_{eff} \propto \Delta V_{SR}$. By the relationship

$$\frac{(\Delta V_{eff}/\Delta V_{GS})}{(\Delta V_{eff}/\Delta V_{SR})} = \gamma, \text{ (Equation 7)}$$

we can extract the γ factor from the slopes in Figure 2.11b. The extracted γ is 0.3, which is similar to another independent measurement in Figure 2.11a (γ = 0.2). Thus we confirm that the extracted relationship in Equation 6 matched well to physical measurements.

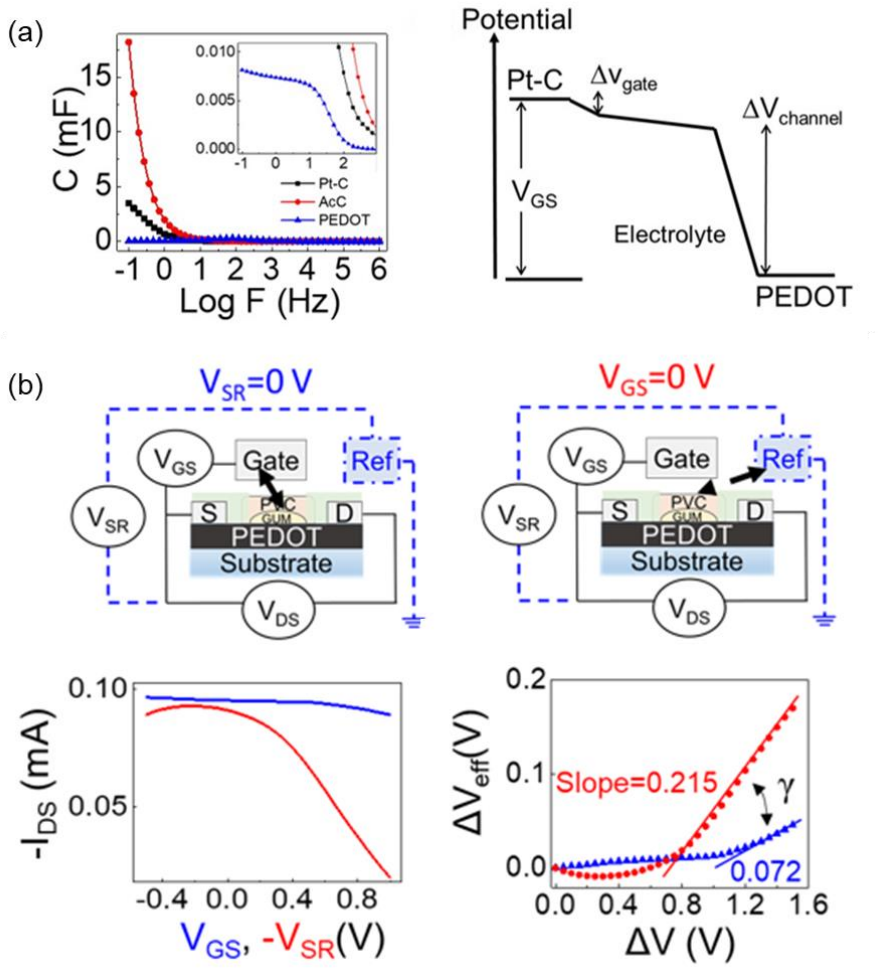

Figure 2.11. The design of experiments for derived equations. (a) Capacitance of electrodes in this work. (b) Dual-gate modulation

2.5 Applications

2.5.1 Application for saltwater green macro-algae

The dimensions of our OECT dissolved oxygen sensor are much more compact and less intrusive than typical electrochemical probes, and the OECT sensor provided local measurements within confined environments such as amid a saltwater green macro-algae (Chaetomorpha Chaeto) in Figure 2.12. Macroalgae are prevalent in reef environments, and they are also grown in aquariums for water purification or to develop a sustainable energy source substitute for fossil

fuels. Photosynthesis in macro-algae is triggered by light and produces oxygen. Figure 2.12 demonstrates that our OECT sensor was able to monitor real-time changes of the dissolved oxygen level, as evidenced by the increased oxygen concentration upon light exposure of the macro-algae.

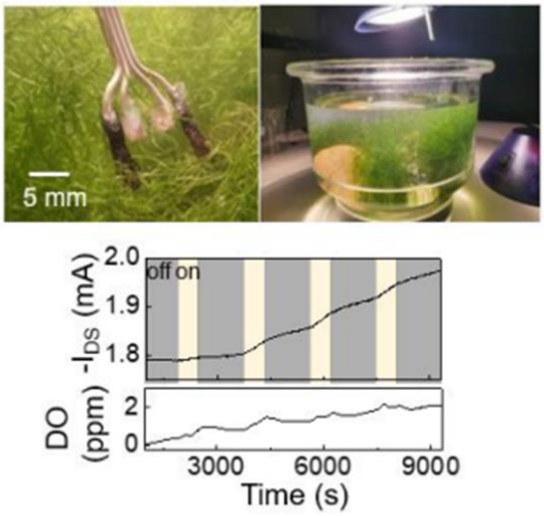

Figure 2.12. Dual-gate OECT monitored the release of dissolved oxygen through photosynthesis in seaweed.

2.5.2 Cross-talking investigation of dual-gate OECTs

It is crucial to investigate the potential cross-talking effect of dual-gate OECTs for their in-situ applications. Therefore, we have examined the potential interferences caused by factors such as light, pH, and temperature, which are common disturbing factors for current sensor technology. Furthermore, we also first investigate the effect from electrostatic discharge that is crucial for device storage. In Figure 2.13a, light sensitivity of device was less than 0.27% change in current upon illumination, and therefore light response was negligible. Sensor response was mostly due to oxygen level change. We measured the effect of pH changes on the oxygen sensor in Figure 2.13b. The dual-gate OECT I_{DS} showed less than a 0.7% change when pH was adjusted between 6 and 9 (broader than the typical pH range in the ocean), our dual-gate OECT sensor was more sensitive to dissolved oxygen than pH changes, indicating that our devices exhibited specificity to the

intended analyte. In Figure 2.13c, electrostatic discharge (ESD) measurement was carried out, in which 2 kV was applied onto the channel surface while source and drain are both grounded. The device can tolerate multiple discharge events, and then it stopped working after 20 times of shocks.

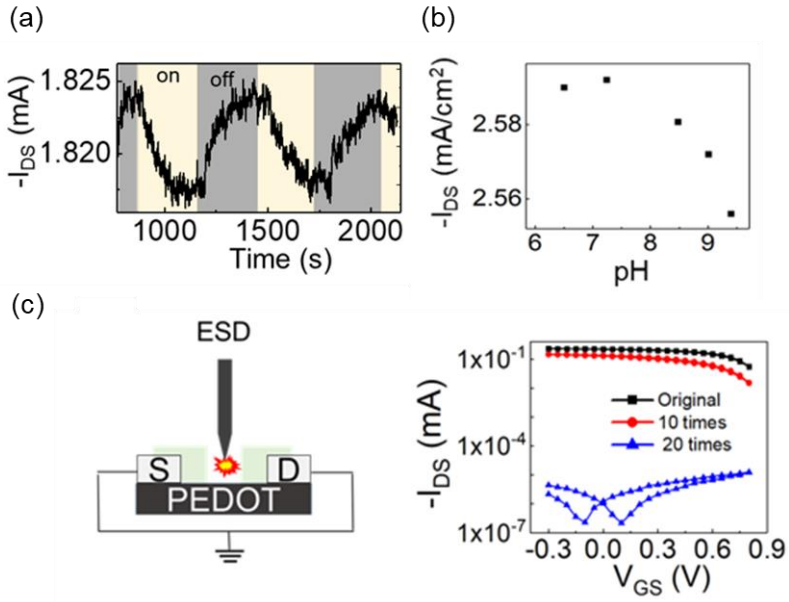

Figure 2.13. Cross-talking effect (a) Light (b) pH and (c) ESD measurements

2.5.3 Detection capabilities and stability

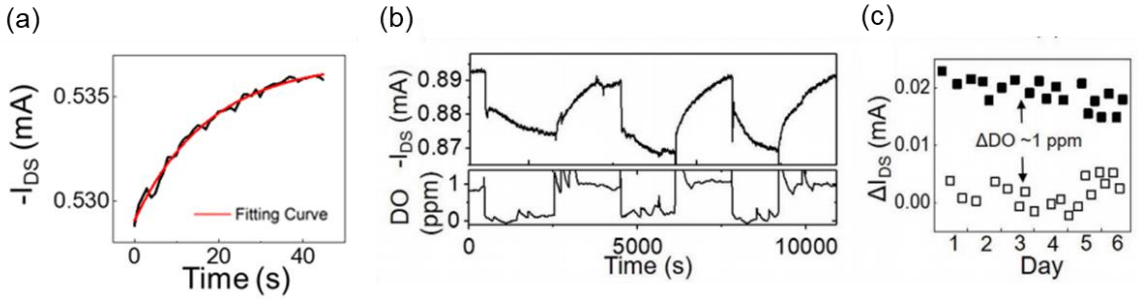

Figure 2.14. The operating stability in dual-gate OECTs. (a) Settling time of dual-gate OECTs. (b) Step DO variation from ~0 to 1 ppm. (c) Corresponding results over 5 days.

The detection capabilities of dual-gate OECTs have been extracted in the aspect of response time, step DO variation and long-term device operation in Figure 2.14. The dual-gate OECT I_{DS}

response versus time, as the DO level was switched from 0.4 to 0.5 ppm through bubbling oxygen into the seawater with stirring condition. The device was operating at V_{SR}= -0.6 V and V_{DS}= -0.2 V, V_{GS} = -0.3 V. The exponential fit gave a time constant of 17.7 as the settling time in Figure 2.14a. We characterized the stability of a dual-gate OECT submerged in seawater over five days. The dissolved oxygen concentration of the seawater was periodically adjusted between 0 and 1 ppm, as shown in Figure 2.14b. The sensor response in Figure 2.14c clearly distinguished the two levels. As a proof of concept, the dual-gate OECTs dissolved oxygen sensor has demonstrated stable operation in seawater for 5 days. Those measurements discrepancy was possibly contributed from sensor placement, stirring conditions or intrinsic low response time, require compliments in the future.

2.6 Conclusion

The dual-gate OECTs in this work provides a simple but effective approach to extend the electrochemical stability window over 2 V. This novel device design facilitates high redox potential reactions between the gate and reference gate, while modulating the deposited channel within a capacitive potential range to maintain the semiconductor stability. We presented the analytical equations for I_{DS} modulation in dual-gate OECTs. Complementary to the search for new channel materials to improve stability, the dual-gate strategy is applicable to existing semiconductors and simple to implement just by including an additional electrode. Thus, this work enables the use of conventional PEDOT materials in the challenging task of high redox potential regime.

As a miniaturized *in-situ* sensor, the dual-gate OECTs showed a detection limit of 0.3 ppm dissolved oxygen concentration in seawater. Below 5 ppm, the sensitivity was 222 $\mu A\ cm^{-2}\ ppm^{-1}$. The device was capable of monitoring oxygenation changes due to saltwater macro-algae under

photosynthesis cycles. Signal drift and interference by pH changes were characterized, and the OECTs dissolved oxygen sensor has demonstrated stable operation in seawater for over 5 days. In addition to monitoring dissolved oxygen, the dual-gate OECTs sensor can be extended to other analytes, to reduce the size, weight, and cost of sensor systems and enable non-intrusive studies of marine ecosystems.

Chapter 2, in part, is a reprint of the material as it appears in Advanced Electronic Materials. Shuo-En Wu, Lulu Yao, Alan Shiller, Andrew H Barnard, Jason David Azoulay and Tse Nga Ng. 2021. Dual-Gate Organic Electrochemical Transistors for Marine Sensing. The dissertation author was the primary investigator and author of this paper.

CHAPTER 3: POINT-OF-USE PRINTED NITRATE SENSOR WITH DESALINATION UNITS

3.1 Challenges and proposed solutions for anion detection in seawater

Printed integrated ocean sensor should possess the capability of monitoring multiple environmental parameters in real-time. In order to facilitate *in-situ* real-time monitoring, electrochemical sensors based on ion-selective membranes (ISM) offer the advantages of reduced size, weight, and cost for the development of systems that can be more readily integrated into the propose printed integrated ocean sensor platform. However, anion measurements based on ISMs are vulnerable to chemical interferants. In the current technology, low sensitivity and poor detection limits are observed in potentiometric ISM sensors when used to examine wastewater or seawater with high chloride concentrations.

To address this challenge, various desalination technologies such as reverse osmosis, electrodialysis, and distillation have been attempted. However, these mature techniques have limitations such as the lack of selective removal of anions or being too bulky to integrate into our proposed integrated ocean sensor. From a materials science standpoint, it is necessary to undertake complex materials design, and in most cases, the performance of such materials is still sensitive to manufacturing conditions. Additionally, these materials often exhibit poor anion sensitivity even when the chloride concentration in seawater is much lower than its actual value.

To selectively remove chloride, a desalination approach based on a microfluidic platform has been demonstrated by oxidizing chloride anions on silver electrodes resulting in AgCl solids. This reversible electrochemical process is specific to the removal of chloride from solution without the loss of nitrate. Prior microfluidic desalination prototypes involve machining of plexiglass or molding of polydimethylsiloxane: however, this poses challenges for embedding electronic components[34,35].

Here, we present a microfluidic platform built with cutting and lamination of poly(ethylene terephthalate) (PET) films, which are compatible with additive printing of electronic materials so that electrochemical units can be easily incorporated into different layers within the microfluidic platform.

3.2 Microfluidics platform design and fabrication

In this section, platform design/fabrication, connector/motor assembly and nitrate sensor preparation are presented in detailed.

3.2.1 Microfluidics platform design

The conceptual structure of our microfluidic device consists of drain channel, tandem desalination units and downstream nitrate ISM sensor as shown in Figure 3.1a. The purpose of the compartments is to minimize the chloride concentration in the incoming seawater and enable potentiometric nitrate detection in the subsequent continuous flow. The sample inlet was split into two separate streams, with one connected to a wide drain channel for displacing inline air bubbles and regulating flow rate to be 3.5 μL/s, while the other channel entered the desalination process. After undergoing electrochemical desalination, the two streams would gradually separate into a concentrated seawater stream (deep blue) and a desalinated seawater stream (light blue). Subsequently, the desalinated seawater flows into the potentiometric ISM sensor for the detection of changes in nitrate concentration. As such, the sample treatment and detection were implemented in one integrated, credit-card size compact platform. In Figure 3.1b, the two tandem desalination electrochemical cells were patterned from layers 2 to 9, with Nafion ion-exchange membranes serving as separators embedded between layers 3 and 4, as well as between layers 7 and 8. The desalination units were stacked on top of each other, to minimize the device area footprint, while each unit increased the stack thickness by less than 0.5 mm. The serpentine channel in layer 10

increased the distance between the desalination unit and the sensor to mitigate parasitic voltage coupling. The sensor with an ISM of nitrate ion-exchange matrix was placed on top of layer 11 to complete the fabrication. Detailed layout of each layer has been summarized in Figure 3.2a.

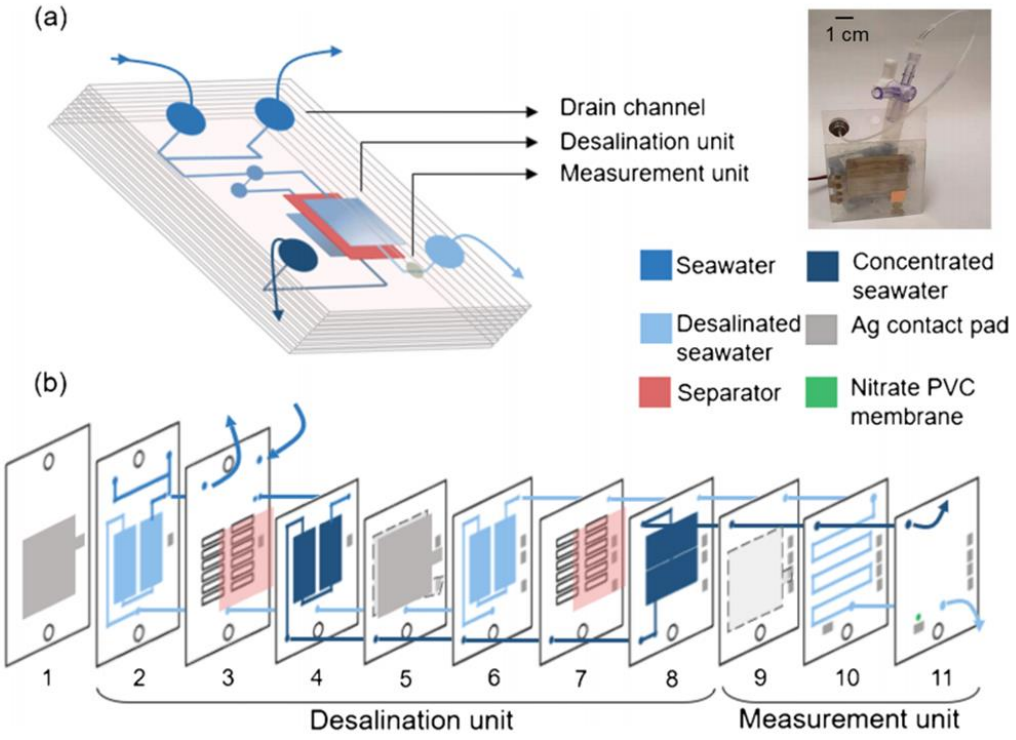

Figure 3.1. Proposed Microfluidics platform (a) Schematics of the microfluidic platform with electrochemical desalination units preceding the nitrate sensor. (b) Detailed configurations and flows inside the platform

The experimental setup was custom-made using easily accessible materials. Seawater was fed through a Teflon tube joint connected to a mini water pump submerged in a tank. The microfluidic device was connected to the Teflon tube using a magnetic gasket holding the tube and a magnetic plate under the device, as shown in Figure 3.2b. The mini water pump designed for aquariums and fountains was purchased from Ledgle and was run at 5 V during the experiment. The flow rate was tuned to be ~ 3.5 µl/s into the desalination cells. Samples in this work were artificial seawater

prepared using Instant Ocean Sea salt to reach a salinity of 31 g/kg, and the concentration of nitrate in the samples was adjusted by adding sodium nitrate into the water tank. The samples were pumped through a Teflon tube joint into the microfluidics device. The Teflon tube joint was held in place by magnetic force between magnetic gaskets (TJ250B, Amazing Magnets) and a magnetic plate sandwiching the microfluidic device. Magnetic gaskets were further soaked by the AF Teflon solution to reduce the potential corrosion in the future use.

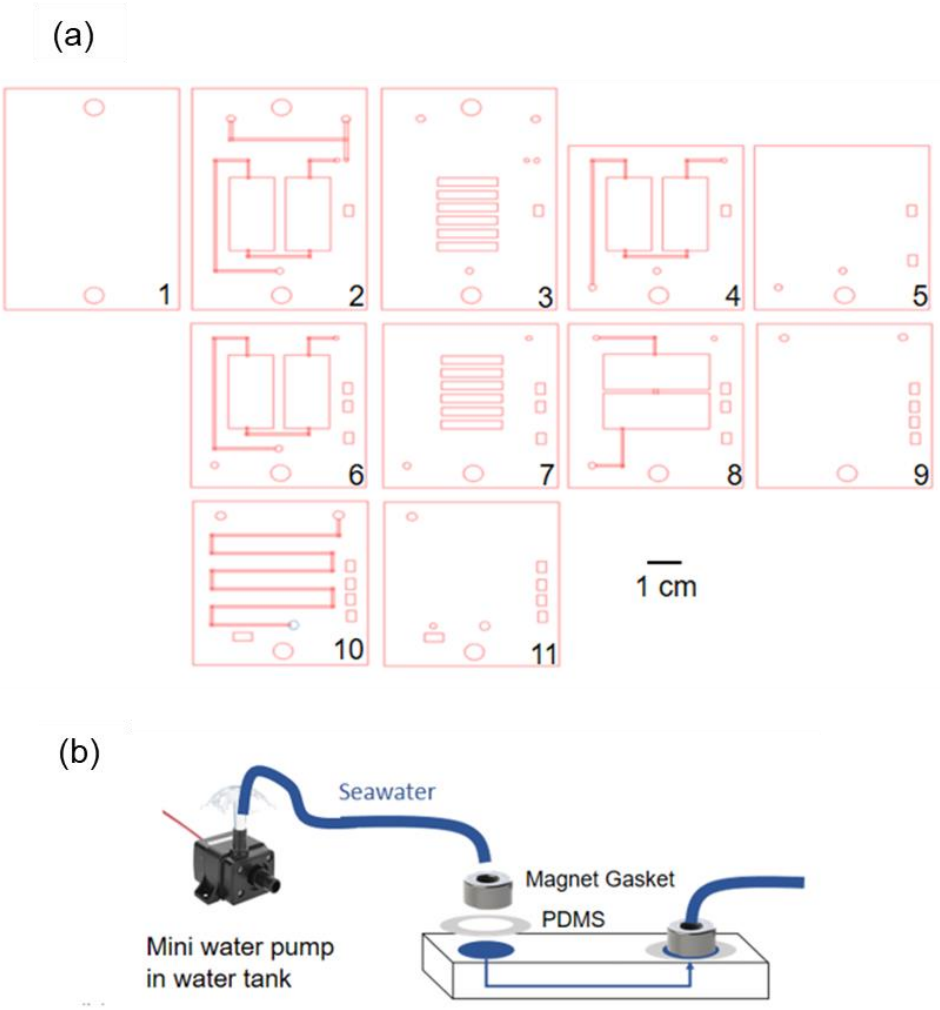

Figure 3.2. Setup for microfluidics experiments. (a) The cut-out pattern of each layer to be laminated into the microfluidic platform. (b) A schematic of the water pump connection to the microfluidic platform by magnetic gaskets (with magnetic plate underneath)

3.2.2 Microfluidics platform fabrication

We used low-cost patterning and assembly techniques, including digital cutting, stencil printing, and heat lamination, as summarized in Figure 3.3. First, 130 μm thickness of PET films were blade-cut by Silhouette® plotter to define the flow channels (500 μm width and 130 μm height), electrode via holes, alignment holes and contact pad (0.3×0.2 cm). Then, Ag/AgCl ink was stencil printed as working electrode and counter/reference electrode in layer 1, 5 and 9 (desalination unit) with dimension of 2.5×3 cm, external reference electrode in layer 10 with dimension of 0.2×0.1 cm. After removing the stencil mask, Ag/AgCl ink was dried at 85℃ for 30 minutes. Subsequently, Nafion separators (part# 221) with thickness of 25.4 μm and areas of 4 × 4 cm^2 were inserted, and the entire stack of films were pressed between glass slides at 150 °C until the PET films looked transparent. The heat laminated the layers together by melting the adhesives on the PET films. The PET films came with the adhesive pre-attached for lamination.

Subsequently, the nitrate sensor electrode was attached on the top layer, followed by silicone encapsulation. The nitrate sensor was based on the configuration of a potentiometric electrochemical cell. We placed the sensor after the lamination step to avoid sensor degradation by high temperature, and this sequence also allowed facile exchange of sensors without the need to reassemble the microfluidic structure.

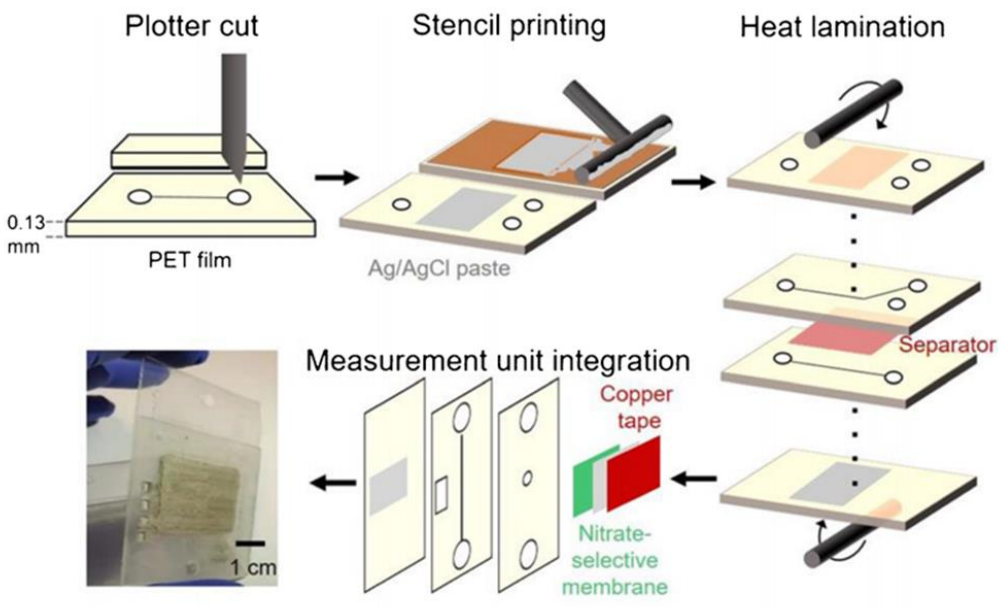

Figure 3.3. Schematics of fabrication methods for the microfluidic device

3.2.3 Solid nitrate ISM sensor preparation

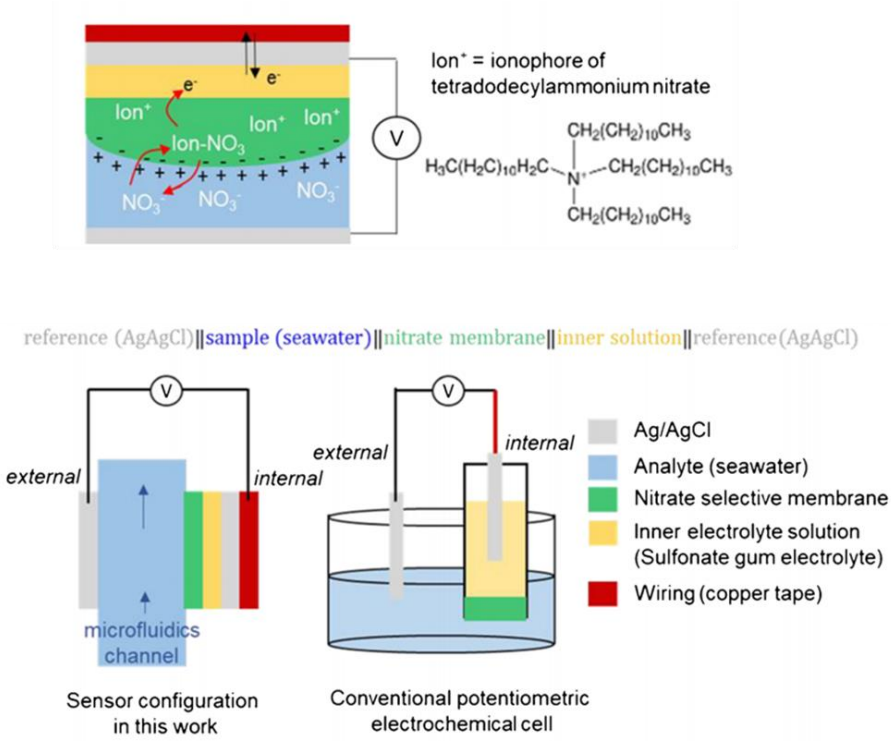

Figure 3.4. Configuration/components of solid-state ISM nitrate sensor and its working principle compared with conventional potentiometric electrochemical cell.

The configuration of solid nitrate ISM sensor is based on a potentiometric electrochemical cell as shown in Figure 3.4. The nitrate selective membrane was a modified version of a cocktail formulation with the host matrix polyvinylchloride (PVC). The cocktail was prepared[36,37] by mixing 1 ml of tetrahydrofuran, 64 mg of 2-nitrophenyl octyl ether, 32 mg of PVC, and 4 mg of tetradodecylammonium nitrate (TDAN). The selectivity coefficients of TDAN to different ions are listed in Table 3.1. The chemicals were purchased from Sigma-Aldrich and used as received. The solution was drop cast onto a glass slide and allowed to dry over a day to form stand-alone films. Meanwhile, a piece of copper tape that would serve as the current collector was cleaned by acetone to remove the surface adhesive, and then Ag/AgCl ink was printed on the clean surface and annealed at 120 °C for 30 min to serve as the internal reference electrode of the sensor. To enable adhesion between the electrode and the nitrate-selective membrane, we used a gum electrolyte. The gum electrolyte was a solid-state film prepared by dissolving 1 g xanthan gum powder in 10 ml of 1 M sodium sulfate aqueous solution[38]. The gum electrolyte served as an interface for charge exchange between the nitrate-selective membrane and the internal reference electrode. A thin paste of gum electrolyte~100 μm was spread onto the Ag/AgCl electrode, followed by placement of the PVC nitrate-selective membrane. This sensor stack was put on the flow channel with the membrane in contact with the sample. The ion-exchange process at the membrane surfaces would lead to a potential difference if nitrate concentrations were not equal across the two sides of the ion-selective membrane. Thus, the analyte concentration was inferred by measuring the potential difference across the nitrate-selective membrane. The nitrate sensor was calibrated with a NIST-certified nitrate standard solution (40.0 mg/L NO_3-N in de-ionized water as received from Sigma-Aldrich) in Figure 3.5.

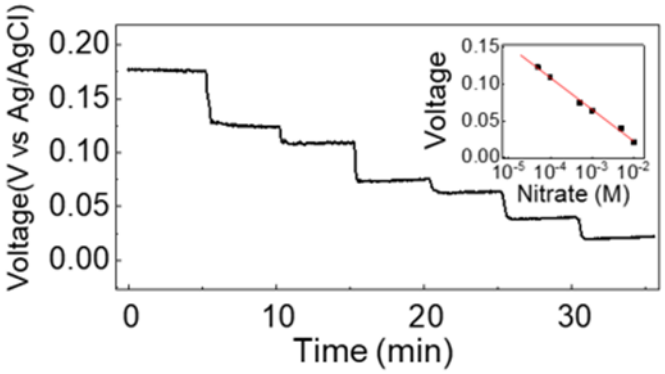

Figure 3.5. Calibration of a printed nitrate sensor using a NIST-certified standard nitrate solution (40.0 mg/L $NaNO_3$ in deionized (DI) water, Sigma-Aldrich) adjusted by dilutions with DI water. The calibration shows a sensitivity of 49 mV/dec with 1mM supporting electrolyte NaCl in DI water.

Table 3.1. Selectivity coefficients of tetradodecylammonium nitrate (TDAN) in 0.01 M background interfering ions (T=25°C)[37]

Interfering ions	Selectivity coefficients (K_{ij})	Log K_{ij}
Cl^-	1.2×10^{-3}	-2.9
SO_4^{2-}	1.4×10^{-4}	-3.8
Br^-	6.9×10^{-2}	-1.2
I^-	3.8	0.6
$H_2PO_4^-$	2.6×10^{-3}	-2.6
HCO_3^-	5×10^{-4}	-3.3
NO_2^-	2×10^{-2}	-1.7
Acetate	6.9×10^{-3}	-2.2

3.3 Desalination and dynamics

The ability of the microfluidics platform to desalinate seawater is a critical factor in achieving high sensitivity for nitrate detection, especially in complex seawater matrices. To address this, we utilized silver/silver chloride ink to selectively remove chloride ions under continuous seawater flow within the microfluidics platform. In this section, we discuss the principle of desalination, the dynamics of chloride removal, and platform stability with the cycle of desalination runs.

3.3.1 Desalination principle and dynamics

The principle of chloride removal is based on the silver (Ag) reaction on the chloride (Cl^-) and become solid silver chloride ($AgCl_{(s)}$). According to the previous design on electrochemical

desalination cells, the cation-exchange Nafion film would be inserting between Ag electrodes[39,40]. The desalination voltages were performed in positive or negative potential alternatively as shown in Figure 3.6a. On the electrode at a positive potential, silver reacted with chloride ions selectively and formed silver chloride precipitates, resulting in chloride removal and reduction of water salinity in this compartment. In the complementary compartment with the electrode at a negative potential, chloride ions were released by silver chloride reduction, leading to an increased salinity in water on this side. Thus, the electrochemical process adjusted the chloride concentration and the associated salinity of the input seawater. The channel with increased Cl^- was directed to a discharge outlet, and the flow path of the de-chlorinated water was connected to the downstream sensor. Before performing the effective desalination process, the Nafion film requires a pre-soaking step of 10 minutes in seawater to reach saturated moisture and hence have a stabilized potential during desalination performs. Figure 3.6b shows the activation of the Nafion films by examining their potential with respect to the reference electrode (Ag/AgCl).

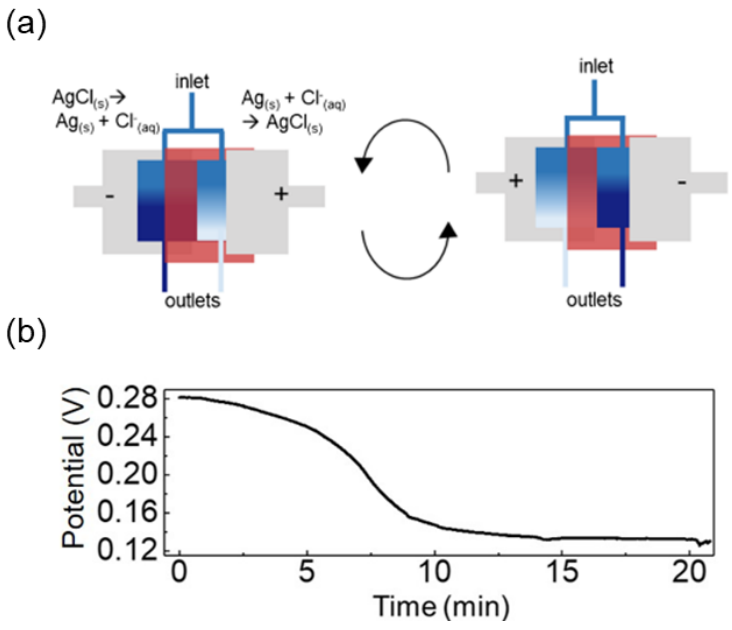

Figure 3.6. Selective chloride removal. (a) Schematics of the electrochemical desalination cell with Ag/AgCl ink. The blue areas indicate flow channels, and the red square is the Nafion separator. (b) The Nafion membrane was activated by soaking under seawater.

Figure 3.7a shows CV of the Ag/AgCl electrode pair in artificial seawater of salinity 31 g/kg. The peak current and redox potentials were symmetric upon cyclic voltage sweeps, indicating that the electrochemical reactions were reversible. The wide peak-to-peak separation (1~2 V depending on the scan rate) was due to the sample solution resistance and manifested as an ohmic drop across the electrode pair. The potential for initiating desalination was around 0.5 V between the Ag/AgCl electrodes, and current magnitudes increased with a higher voltage scan rate. The peak current (log I) versus scan rate (log V_s) followed a power law relation log(I)=log(a)+log(Vs), as presented in Figure 3.7b , with fitted values of a=0.048 and b=0.45. The b value showed that the current was proportional to the square root of scan rates ($I \sim V_s^{0.5}$), indicating the desalination process here was a diffusion-controlled reaction according to the Randles–Sevcik equation[41,42].

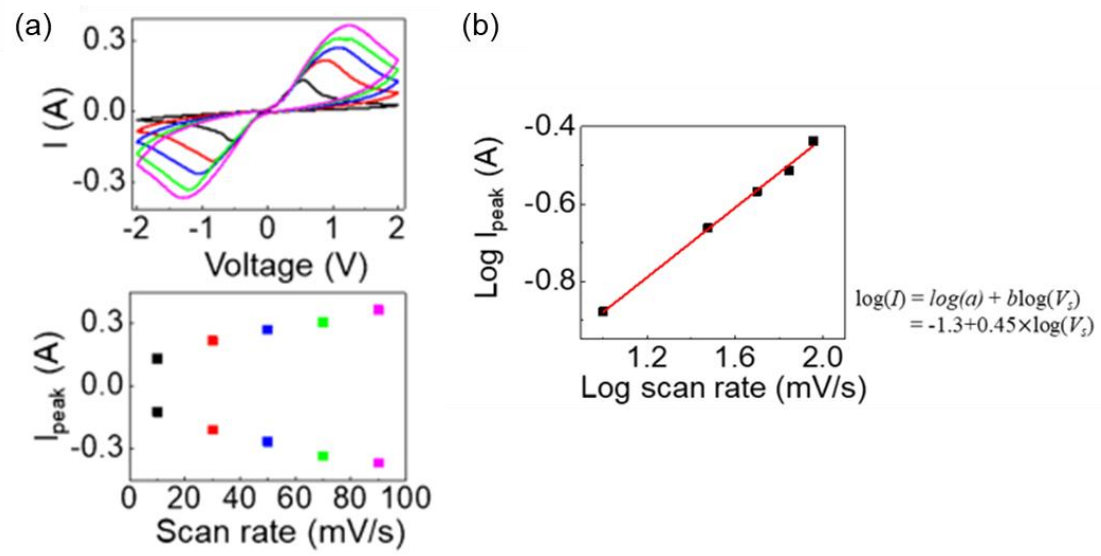

Figure 3.7. Dynamics of chloride removal by silver paste. (a) Top: cyclic voltammetry at scan rates from 10-90 mV/s, in increments of 20 mV/s. Bottom: peak current obtained from the above data versus scan rates. (b) Extracted relationship between log(I_{peak}) and log(scan rate).

3.3.2 Desalination efficiency and nitrate sensitivity in different chloride background

Figure 3.8a shows how the water salinity level changes with the applied voltage. The sample flowed continuously at a rate of approximately 3.5 µl/s into the desalination cells. The electrode

was subjected to a constant voltage for 5 minutes and then turned off for 2 minutes to allow the compartment to be replenished with untreated seawater. Following a 2-minute replenishing period, the electrodes were subjected to another 5 minutes period with the same voltage magnitude but with the opposite polarity to the previous one, to reverse the Ag/AgCl reactions and refresh the electrode surfaces for the subsequent desalination cycle. At the end of each biasing condition, the apparent salinity was measured in line with a calibrated refractometer. The apparent salinity (PSU) decreased from the initial values of 31 to 15, 12, and 6, at 1 V, 1.5 V, and 2 V, respectively, for the compartment with the electrode at positive biases. When negative potentials were applied to refresh the Ag/AgCl electrode, the apparent salinity increased to 43, 46, and 45, at -1 V, -1.5 V, and -2 V, respectively. A smaller salinity change is observed during regeneration (from the unprocessed sample with 31 g/kg to 45 g/kg, a change of 14 g/kg) than during desalination (from 31 g/kg to 6 g/kg, a change of 25 g/kg). We hypothesize that the initial Ag/AgCl ratio in our electrodes may not be equally composed and could contain a lower proportion of AgCl. As a result, less AgCl is reduced during the regeneration process, resulting in the release of fewer Cl^- ions and a smaller salinity change. Furthermore, we determined the desalination efficiency by calculating the ratio of salt removed to the initial salt concentration, based on the measured changes in chloride concentration after passing through both stages. Converting apparent salinity to NaCl molar concentration, 31 g/kg=0.5 M and 6 g/kg=0.1 M, the amount of NaCl removed from the seawater sample at 2 V was 0.4 M as concluded in Figure 3.8b. Thus, the desalination efficiency can reach 0.4 M /0.5 M=80% in our tandem microfluidics device.

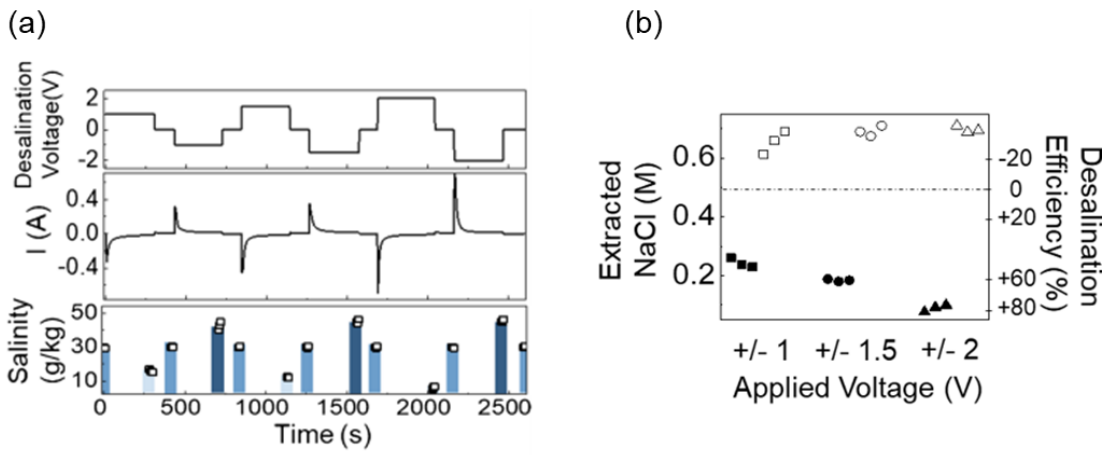

Figure 3.8. Evaluation of desalination efficiency in microfluidics platform. (a) Applied voltage on the desalination cell electrodes (top), corresponding measured current (middle), and measured salinity at the channel outlet (bottom) as a function of time. The data points of salinity were measured at the end of a period under a fixed voltage. The colors of the bars are guides to the eye, in which light blue indicates the sample is desalinated, medium blue is untreated (cell at 0 V), and dark blue is at a higher salinity level than the input sample due to regeneration of the electrode. (b) Measured NaCl concentration and the corresponding desalination efficiency with respect to the applied voltage.

The sensitivity of the solid-state nitrate ISM sensor is strongly affected by the concentration of background chloride ions. Figure 3.9 summarizes the calibration of the sensor under different background NaCl (M) concentrations. The theoretical sensitivity of the nitrate ionophore is 51.9 mV/dec according to Nernst relationship ($\frac{kT}{ze} log Q_r$), which is similar to the sensitivity of our fabricated solid-state nitrate ISM sensor, measured to be 48.7 mV/dec under 0.001 M Cl^- ions solution. This result represented the feasibility of our proposed solid-state ISM nitrate sensors with the gum electrolyte. Furthermore, the sensitivity decreases significantly with an increase in background chloride concentration, until it is completely loss under 0.5 M Cl^-, which is equivalent to chloride molar composition in seawater. The efficiency of electrochemical desalination in our microfluidic platform was found to be 80%, resulting in a concentration of ~0.1 M Cl^- in the desalinated seawater. Therefore, the ideal nitrate sensitivity in our desalination platform shall be 12.9 mV/dec as we extracted from Figure 3.9.

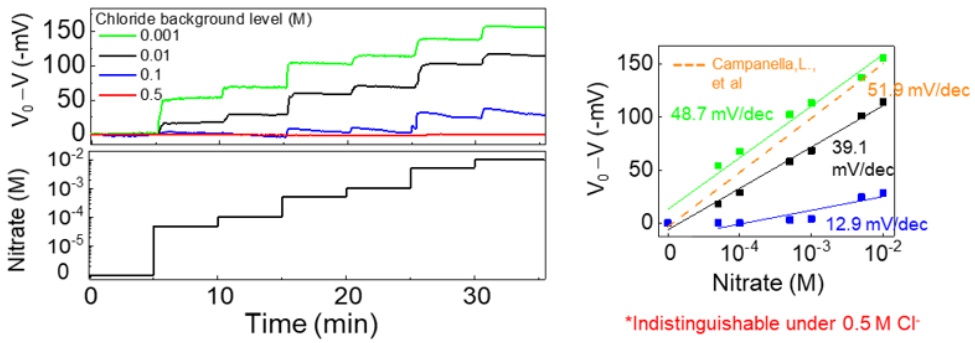

Figure 3.9. The nitrate ISM sensor sensitivity depends on the level of background chloride concentration.

3.3.3 Desalination cycles and its stability

The recovery of $AgCl_{(s)}$ and Ag redox reactions in our proposed microfluidics platform was evaluated through cycles of the desalination process. Previous results showed that a pair of silver/silver chloride electrodes can reach almost 99% recovery under well-controlled experimental conditions. However, we identified some issues that compromised the recovery of Ag under microfluidics platform operation, which are summarized in Figure 3.10. As expected, in Figure 3.10a, the recovery of the silver/silver chloride electrodes can last for over 100 cycles and more (without Nafion separator), with distinguishable oxidation and reduction peaks at 1 V and -1.5 V, respectively. However, in the first few runs of CV, the widen of peak-to-peak distance indicates an increase in cell resistance, resulting from the reconstructing of silver/silver chloride morphology and more insulated precipitated $AgCl_{(s)}$ on the surfaces of electrodes until reached to dynamic equilibrium state. This finding is consistent with the previous results[43] that desalination voltages are necessary for at least 1 V to acquire effective desalination efficiency.

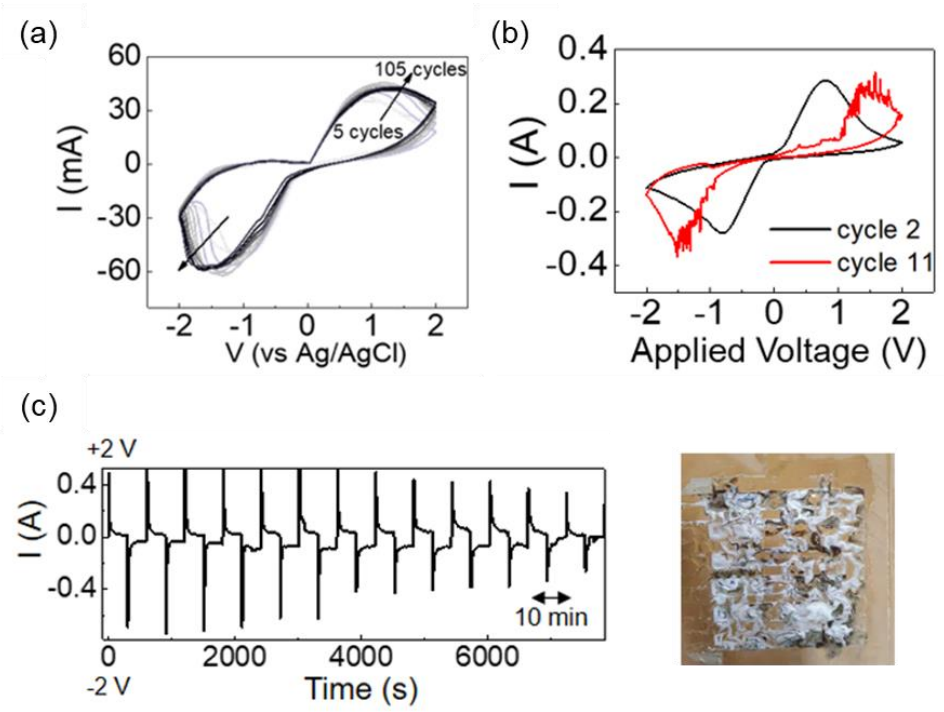

Figure 3.10. Operating stability of Microfluidics platform. (a) CV of the desalination electrode pair, without placing a Nafion separator in between. Shift of the redox peaks indicates a gradual deposition of AgCl on the electrodes, resulting in a higher cell resistance with increasing CV cycles. (b) CV taken with a Nafion membrane between the electrode pair. (c) Current responses measured across the desalination electrode pairs, as +/- 2 V was alternately applied in each 10 minutes cycle. Ion-exchange membrane contamination due to deposition of silver complexes.

Figure 3.10b shows the results of inserting a Nafion film between pairs of silver/silver chloride electrodes and performing several CV scans in a static electrolyte environment. In contrast to Figure 3.10a, the cell resistance significantly increased after only 11 cycles, and the redox currents became tricky. Redox instability observed in Figure 3.10b was due to the insoluble AgCl precipitated on the surface of Nafion membrane, which could not be removed by applying a recovery voltage. The growth or regrowth of insoluble $AgCl_{(s)}$ is directionless, making it easy to accumulate and block the small space between the silver/silver chloride electrodes and Nafion film, due to narrow size of microfluidic design. In our *in-situ* employed microfluidics platform, the feeding flow is continuous within the desalination cells. Thus, the blocking from precipitated $AgCl_{(s)}$ can be mitigated by the flow rate control as shown in Figure 3.10c. The desalination

voltages were performed at ± 2 V for each 10 minutes. As it clearly showed the decreasing of redox current after 4000s, the desalination efficiency was drop from 80% to 50 %. After experiments, the Nafion film was taken out and we could clearly see the severe contamination on Nafion film with different levels of re-deposited $AgCl_{(s)}$. There is a trade-off between desalination efficiency, the size of desalination cells and lifetime of separator. Therefore, future desalination microfluidics designs should aim to strike a balance between these factors.

3.4 Cross-talking effect from desalination units

During the integration of desalination units and the nitrate ISM sensor, it is important to carefully plan the channel distance between the two to mitigate parasitic voltage coupling. This is particularly important because seawater acts as a conductive electrolyte (even for 80 % desalinated seawater) between the electrodes in contact with it. Previously, voltage cross-talking has been reduced by physically isolating channels using mechanical valves or by introducing air bubbles. However, to reduce the complexity of fabrication and control electronics, we have chosen to simply extend the distance between the desalination units and the sensor. By using a long serpentine path in Figure 3.11a, we increase the electrical resistance and thus create a sufficient voltage drop to make the voltage cross-talking negligible. A pulse of 0.5 V was then applied to the desalination electrodes, and the electrolyte path-length resistance was represented by a variable resistor $R_s(D)$ in the equivalent circuit model, where D was the distance parameter. Fixed resistors included the resistance of the electrodes, separator, and nitrate-selective membranes. Figure 3.11b displays the cross-talking voltage (ΔV) measured at the sensor electrodes as the desalination units were turned on and off. The extent of cross-talking was calculated as a percentage (%), defined as $\% = \Delta V/V_{desal}$, where V_{desal} was the applied desalination voltage (0.5 V in this measurement, a small potential to avoid the complexity of redox reactions occur in the desalination cell). The cross-

talking % decreased to less than 1% and became negligible when the channel path-length was longer than 20 cm. Therefore, we used a serpentine length of 27 cm as the connection path between the desalination units and the nitrate ISM sensor to minimize parasitic voltage coupling.

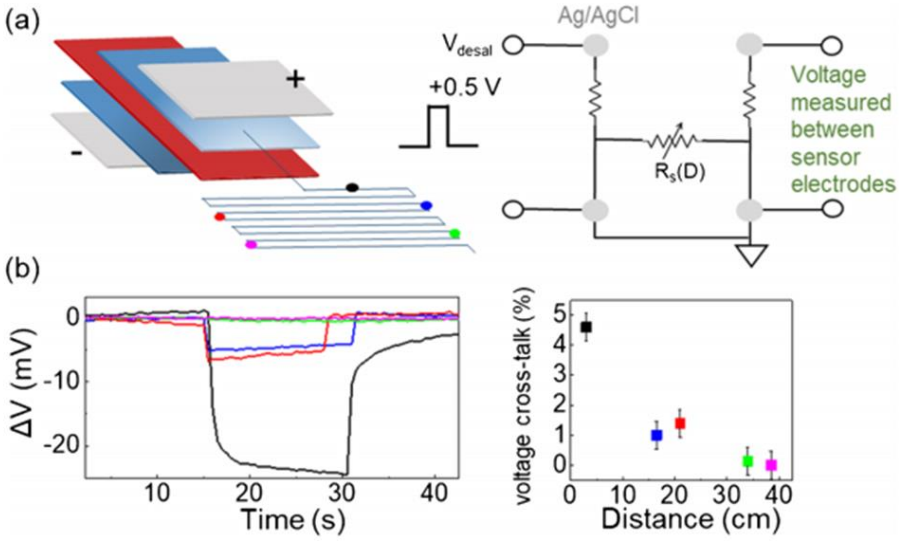

Figure 3.11. Cross-talking within platform. (a) Schematic of the voltage coupling measurements at increasing path lengths away from the desalination unit as indicated by the different color points. An equivalent circuit model representing the path between desalination electrodes and sensor electrodes is shown on the right. (b) Measured open-circuit voltage at the sensor electrodes when desalination electrodes were at 0.5 V. The data point colors correspond to the locations in part a.

The voltage dependence of the nitrate ISM sensor is extracted as:

$$\Delta V = \frac{kT}{ze} ln Q_r + [\Delta V_{desal} - \frac{\int Idt}{C_{AgCl}} - V_s(D)] + \text{constant}, V_s(D) \propto R_s = \frac{\rho D}{A}$$

where $\frac{kT}{ze} ln Q_r$ is Nernstian term related with analyte concentration (nitrate), the parameter T is the temperature, k is the Boltzmann constant, e is the electron charge, and z is the number of electrons transferred in the redox reaction. C is the capacitance of Ag/AgCl reference electrode in nitrate ISM sensor and $V_s(D)$ is the potential difference between WE and Ref electrode.

The equation can be further simplified if the cross-talking voltage, as it has been minimized and would be a constant voltage offset even if it was present:

$$V = \frac{kT}{ze} ln Q_r - \frac{\int Idt}{C_{AgCl}} + \text{constant},$$

The term ∫ Idt is the transferred charge during the desalination process and ∫ Idt is dependent on the redox current I integrated over time. As a result, the second term accounts for the small gradual voltage shift during the detection period, which is caused by the ongoing desalination process. The desalination process changes the chloride concentration in the sample and the silver electrode capacitance during the electrochemical process, resulting in a small voltage shift over detection time.

3.5 Application for *in-situ* nitration detection in seawater

After integrating the potentiometric nitrate sensor with the desalination units, we evaluated the sensitivity and detection limit of the microfluidic platform for nitrate analytes in seawater. Without using the desalination units, it was difficult to distinguish changes in nitrate concentration in seawater, only the background drift of the sensor open-circuit voltage as shown in Figure 3.12.

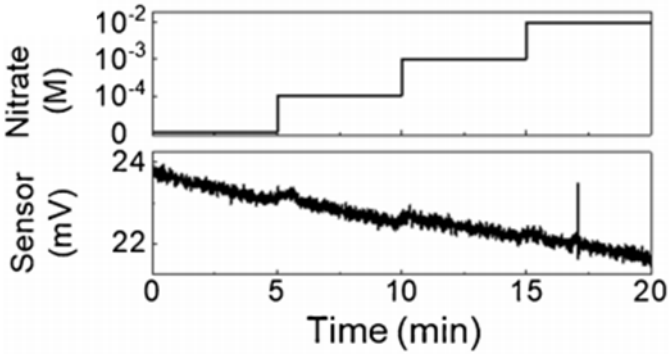

Figure 3.12. Indistinguishable nitrate response without performing desalination.

When the desalination units were used to remove most of chloride, the sensor response to changes in nitrate concentration is much more apparent in Figure 3.13a. With 2 V at the desalination units, the sample flowing into the nitrate sensor was de-chlorinated, and the sensor voltage was measured to change from 19.4 to 1.9 mV as the nitrate concentration was varied from 10^{-4} to 10^{-2} M. After the analyte detection period, the applied voltage to desalination units was switched to −2 V for reducing AgCl back to Ag for the next cycle of desalination and detection. The device settling time after turning on the desalination units was around 8 min. The sensor during this regeneration period was not sensitive to nitrate concentration, with the voltage changing by <8 mV, in comparison to >18 mV response for 10^{-3} M nitrate when there was minimal chloride interference during desalination. The blue points in Figure 3.13a mark the open-circuit voltage measured at the end of each period of desalination, are presented in Figure 3.13b to extract the sensitivity and limit of detection for nitrates. For our platform, the sensitivity was 11.3 mV/dec for nitrate concentration between 10^{-3} and 10^{-2} M, and the detection limit was 0.5 mM with an average sensitivity of 9.8 mV/dec in Figure 3.13c comparing three fabrication batches.

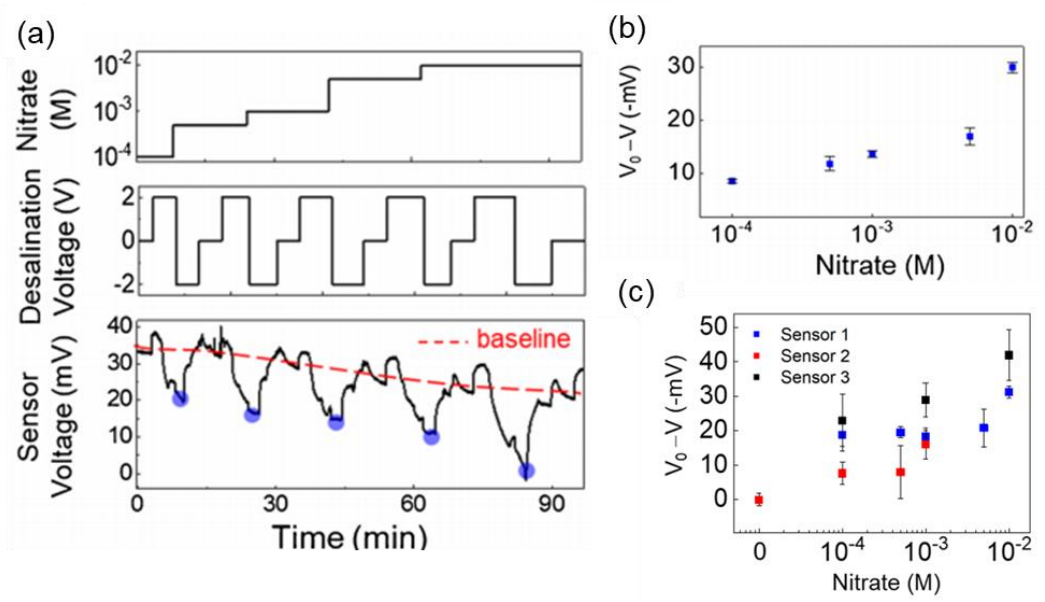

Figure 3.13. Real-time nitrate detection. (a) in-situ Nitrate response with proposed microfluidics platform, alternatively desalination voltages are on or off. (b) Extracted nitrate response from a. (c) Comparison of responses across sensors made in different fabrication runs. The error bars were obtained from running each sensor for three different trials.

The microfluidics platform also demonstrated a similar response when the input nitrate concentration is changed across two orders of magnitudes over a shorter interval time as shown in Figure 3.14. As a result, we have summarized prior works on nitrate response, which have been limited by the high background levels of chloride. We also demonstrated the feasibility of our proposed microfluidics platform prototype under high background chloride concentration in Table 3.2.

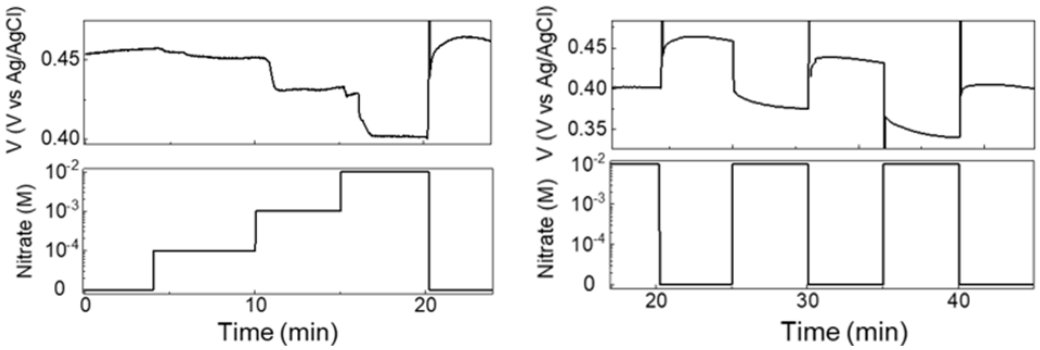

Figure 3.14. Microfluidics platform response in step change of nitrate concentration under continuous flow.

Table 3.2. Potentiometric nitrate sensor performances.

Ion-exchanger	Sample	Range (M) /LOD(μM)	Sensitivity (mV/dec)	Response time	Ref
Tridodecylmethyl ammonium nitrate (TDMAN)	Seawater (processed by desalination modules to 99.3% salt removal)	10^{-7}-10^{-3} /0.5[†]	-58.9* (*after 99.3 % desalination)	~30 mins	(Cuartero et al, 2015)
Tetradodecyl ammonium nitrate (TDAN)	Standard with 10^{-3} M Cl^- background	10^{-5}-10^{-2} /<10	-48.7	<15 s	This work
	Standard with 10^{-2} M Cl^- background	10^{-5}-10^{-2} /<10	-39.1		
	Standard with 10^{-1} M Cl^- background	10^{-4}-10^{-2} /500	-12.9		
	Seawater (originally ~0.5M, desalination to 80% salt removal, leading to ~10^{-1} M Cl^- background)	10^{-4}-10^{-2} /500[†]	-11.3* (*after 80 % desalination)	8 mins	
The sensors below operate in conditions with low Cl^- background					
TDMAN	Tap water	10^{-4}-10^{-2} /30	-57.9	<10s	(Tang, Wenzhi, et al, 2012)
Nitrate ionophore V	Tap/River/Ground/ Well water	10^{-6}-10^{-1} /0.63	-59.4	<5 s	(Pięk, Magdalena, et al, 2015)
Tetradodecylammonium chloride (TDACl)	Lake/River	10^{-7}-10^{-1} /2.5	-53.5	N/A	(Fayose, Tolulope, et al, 2017)
TDACl	Soil	5×10^{-5}-5×10^{-2} /11.3	~-59.2	N/A	(Choosang, Jittima, et al, 2018)
TDMAN	Tap/Well water	10^{-5}-10^{-1} /10	-52	< 25s	(Schwarz, et al,2018)
Trihexyltetradecylphosphonium chloride (THTDPCl)	Mineral/Tap water	10^{-5}-10^{-1} /2.8	-58.9	<10 s	(Wardak, et al,2016)

3.6 Conclusion

A low-cost, portable microfluidic platform has been developed to detect nitrate at millimolar levels in seawater. The cut-and-laminate fabrication process enables rapid and easy integration of

desalination units and ISM potentiometric sensors. The desalination efficiency was up to 80% using two tandem electrochemical cells. The channel length between the desalination and nitrate sensor was optimized to minimize voltage cross-talking. The point-of-use microfluidic platform showed the feasibility of inline analyte monitoring for challenging seawater samples with a ~ 31 g/kg salinity at the input. The sensitivity and detection limit of this platform can be improved by incorporating more desalination units in tandem to raise the desalination efficiency. The problem with precipitation on the desalination separator may be improved by using a higher flow rate and increasing the distance between the electrodes and the separator. The microfluidics system achieved a detection limit of 0.5 mM with a sensitivity of 11.3 mV/dec under continuous flow and able to fit the standard of U.S. EPA for nitrate concentration in drinking water (44 ppm (0.7 mM)). In addition to nitrate sensing, the platform described herein can potentially be extended to other analytes affected by high background chloride concentration, such as phosphate. Overall, our work demonstrates an approach to reduction in the size, weight, and cost of chemical sensor systems for saline waters.

Chapter 3, in part, is a reprint of the material as it appears in Microchimica Acta. Shuo-En Wu, Alan Shiller, Andrew H Barnard, Jason David Azoulay and Tse Nga Ng, 2022. Point-of-use printed nitrate sensor with desalination units. The dissertation author was the primary researcher and author of this paper.

CHAPTER 4: MULTIPLEXED PRINTED SENSORS FOR IN SITU MONITORING IN BIVALVE AQUACULTURE

4.1 Design principle of a novel flexible integrated ocean sensor

Here, we introduce a novel flexible integrated ocean sensor using stencil-printing, lamination, digital blade-cutting[44], and electrodeposition techniques. The sensor system incorporates three sensing functionalities as proof of concept, including dissolved oxygen (DO)[38], salinity, and an encapsulation-free OECTs curvature sensor in Figure 4.1. The fabrication process details are outlined in the following sections. The integrated sensor system operates based on the principle of electrochemical detector, which offers several advantages, such as reduced size, weight, and cost, making it suitable for non-intrusive monitoring systems.

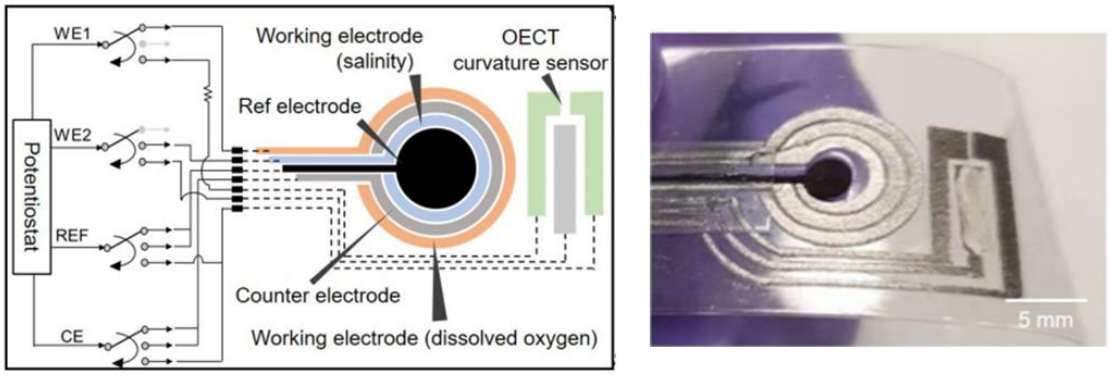

Figure 4.1. Schematics and photographs of the printed multiplexed sensors

The concentric rings represent electrodes for DO and salinity detection. This arrangement minimizes the footprint of the integrated sensors and uses the same reference and counter electrodes for both DO and salinity measurements, reducing the number of required components. The reference electrode is crucial for ensuring signal accuracy and minimizing signal drift over time. The seawater sample contained the target analytes and also acted as the conductive electrolyte in the electrochemical measurements. Of the two working electrodes, one was for

sensing the DO level based on the oxygen reduction reactions (ORRs), and the other was used to measure the seawater conductivity, which at a constant temperature is proportional to its salinity in g/kg. The potentials of the working electrodes (WE) were controlled with respect to the reference electrode (REF), and the corresponding redox or capacitive currents were collected through the counter electrode (CE). Next to the circular electrodes, an OECTs structure was designed to function as the curvature sensor to monitor physical movement of target object. The drain and gate electrodes were controlled by the two WE channels on the potentiostat, while the source electrode was connected to the REF and CE channels tied together for current read-out. This flexible integrated ocean sensor provides multiple parameters that might bridge the gap between the physiology of the target subject and their environmental conditions, which are currently inaccessible to bulky integrated ocean detectors.

4.2 OECTs curvature sensor

In order to accurately measure the movement of target objects *in-situ*, some mature options such as pressure or strain sensors could be utilized. However, they often experience degraded electrical behavior when exposed to moisture, unless additional encapsulation or hydrophobic interfaces are added[45–47], leading to increased complexity especially under complicated seawater conditions. Therefore, we developed an OECT with nanoporous semiconducting fibers that are advantageous for bending curvature measurements, specifically for seawater application. This section will outline the performance of OECTs curvature sensor, fabrication and integration, materials characterizations.

4.2.1 Electrodeposited PEDOT channels

The flexible PET substrate was chosen for the integrated ocean sensor for its easy availability, low cost, high mechanical strength, and flexibility. However, its intrinsic hydrophobic nature and

low melting point make it incompatible with many organic materials and fabrication techniques. We developed a method of electrodeposition to fabricate semiconducting fibers between a pair of deposited graphite electrodes (chosen for its superior electrochemical stability, flexibility and easy availability), which facilitated their inherent alignment. The semiconducting fibers were grown along the direction of an applied electric field until they bridged the electrodes. Then, the semiconducting fibers were aligned with the bending curvature to maximize their structural deformation and, in turn, their change in resistance with bending strain. This electrodeposition technique can greatly reduce the differences in surface energy and highly compatible with almost any hydrophobic substrate.

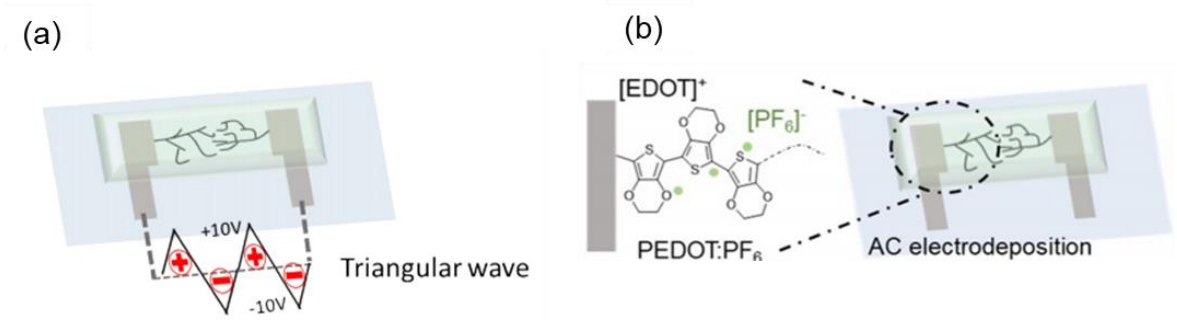

Figure 4.2. Electrodeposition of PEDOT:PF_6. (a) Schematic of the AC electrodeposition waveform. (b) Schematics of PEDOT:PF_6 formed by AC electrodeposition.

The electrodeposition process was performed by applying an AC waveform (triangular) as shown in Figure 4.2a. The resulting semiconducting fibers were characterized as poly(3,4-ethylenedioxythiophene)-hexafluorophosphate (PEDOT:PF_6), which was prepared using a mixed precursor solution of monomer $[EDOT]^+$ and $[PF_6]^-$ as shown in Figure 4.2b. The applied deposition voltages were dependent on respective graphite electrode as a two-electrodes configuration. The EDOT monomers were oxidized on graphite electrodes, initializing the forming cations radicals on the rest of monomers/oligomers units, which were charge balanced by PF_6

anions. Then, the sequential reaction with other EDOT+ monomers enabled the growth of the polymer chain across the electric fields[48–50] built between graphite electrodes. The tip growth of the fibers was more kinetically favorable due to the stronger local field compared to the flat edges of the electrodes.

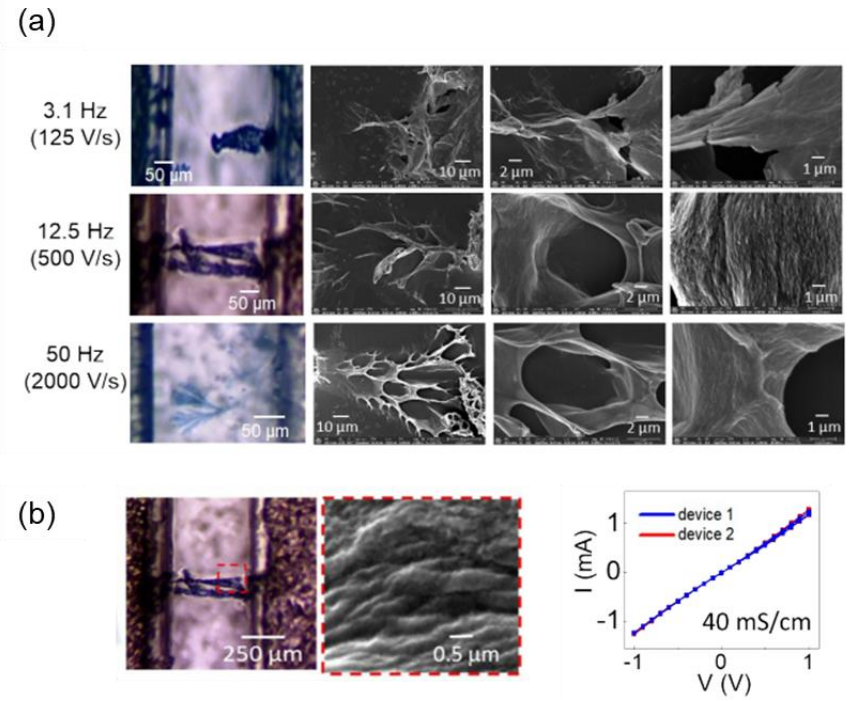

Figure 4.3. Morphology and electrical properties of deposited films. (a) Different deposition conditions lead to various morphology, characterized by scanning electron microscopy (SEM). (b) Forming fibers in this work with optimum growth

Figure 4.3a demonstrates that the morphology of the fibers was largely determined by the amplitude and frequency of the electrodeposition voltage waveform. Higher waveform frequencies (> 50 Hz) resulted in more bifurcation and branching, while lower frequencies (< 5 Hz) resulted in denser and wider strips. After evaluating various factors, we identified that a frequency of 12.5 Hz and an amplitude of ±10 V was the optimal parameter for forming thin fibers with a more porous surface and better conductivity, as observed in Figure 4.3b. The forming fibers conductance

was found to be 40 mS cm^{-1} (250 µm), and this result was reproducible across multiple deposition runs.

4.2.2 Electrical characteristic and mechanical analysis

The curvature OECTs sensor was then fabricated using the previously electrodeposited fibers as channels, with an additional Ag/AgCl gate electrode. The signal output can be further amplified through the OECT structure. Transfer and output characteristics were carried out to evaluate the fundamental OECTs behavior in Figure 4.4. To mimic the natural seawater environment, a seawater hydrogel (seawater-equivalent ionic strength of 0.6 M NaCl) was applied onto the curvature OECTs sensor for ease of experimentation. The OECTs was operated in depletion mode, and a positive gate bias was applied to de-dope the PEDOT:PF_6, reducing the channel conductance as shown in Figure 4.4b and c. The device had a maximum transconductance of g_m = 0.88 mS and an on/off ratio of ~500. The mobility capacitance product (µC*) was calculated to be 1.24 F $cm^{-1}V^{-1}$ s^{-1} with a geometry of a fiber width of 75 µm, channel gap of 250 µm, and two fiber channels. The performance of this OECTs is comparable to that of our previous device in Chapter 1 and consistent with the operating principle of OECTs.

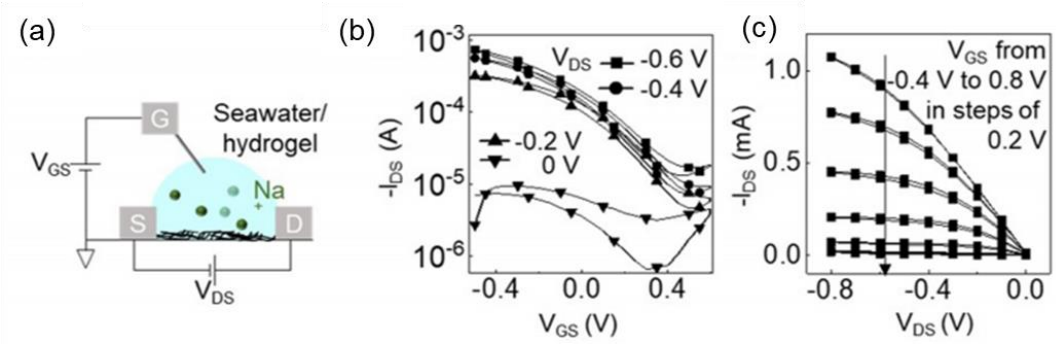

Figure 4.4. OECTs with deposited PEDOT:PF_6 channels. (a) Schematics of an organic electrochemical transistor with seawater hydrogel as the electrolyte. (b) Transfer and (c) output characteristic of a PEDOT:PF_6 electrochemical transistor in the flat state

Before evaluating the curvature performance of OECTs curvature sensor, it is important to ensure that the channel resistance is affected mostly by the bending level, instead by interference from contact resistance between the polymer/electrode interfaces or wire connections. The contact resistance of our OECTs curvature sensor was extracted by Y-function model[51] and was found to be 235.8 Ω in Figure 4.5a, which was consistent with the value obtained from electrochemical impedance spectroscopy (ESI) in Figure 4.5b. On the other hand, the channels resistance was approximately 1 kΩ at a gate bias V_{GS}= 0 V. This indicates that the resistance across the channels was higher than at the contacts, which is favorable for strain sensing as it allows for a large resistance change with the deformation of PEDOT:PF_6 channels.

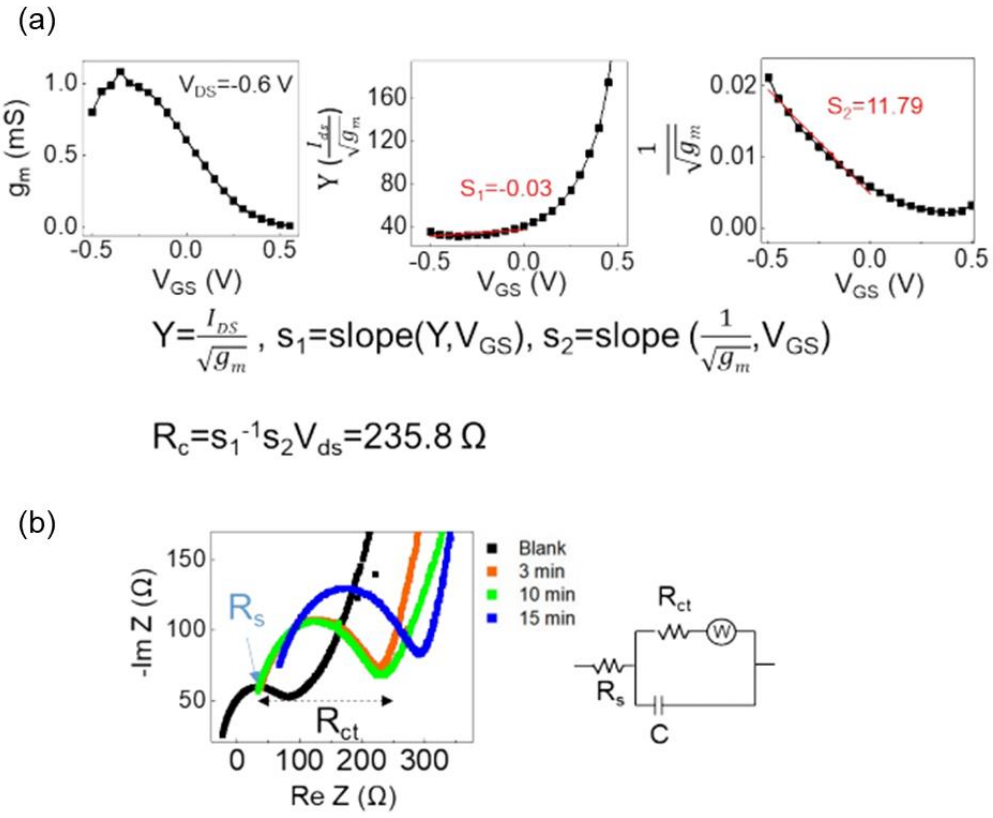

Figure 4.5. (a) Data fitting and calculations of contact resistance of OECTs through Y-function model analysis. (b) Nyquist plot of PEDOT:PF_6 after different deposition periods. R_s ~50 Ohm and ~200 Ohm as acquired from the plot. The R_s and R_{ct} was extracted according to the Randles-Ershler equivalent circuit[52].

The OECTs curvature sensor responses to bending level (curvature) has been evaluated from bending radius (r) 9 to 2 cm as shown in Figure 4.6a. It is evident from the results that the electrodeposited PEDOT:PF_6 channels exhibited good recovery from various bending states, until reaching an irreversible mechanical failure at a bending radius of 1 cm. The baseline shows a minimal drift of less than 6% over 6 minutes, which may be attributed to bias stress. This can be further minimized by adjusting the duty cycle or compensated by drift subtraction. Furthermore, the bending response was primarily due to the extension of channels in I_{DS}, as the level of I_{GS} remained constant at different bending levels in Figure 4.6b. The steady I_{GS} confirmed that the strain in the hydrogel, graphite electrodes, and interconnects did not induce a significant current response, only the semiconducting fibers were the major contributor to the I_{DS} change upon bending.

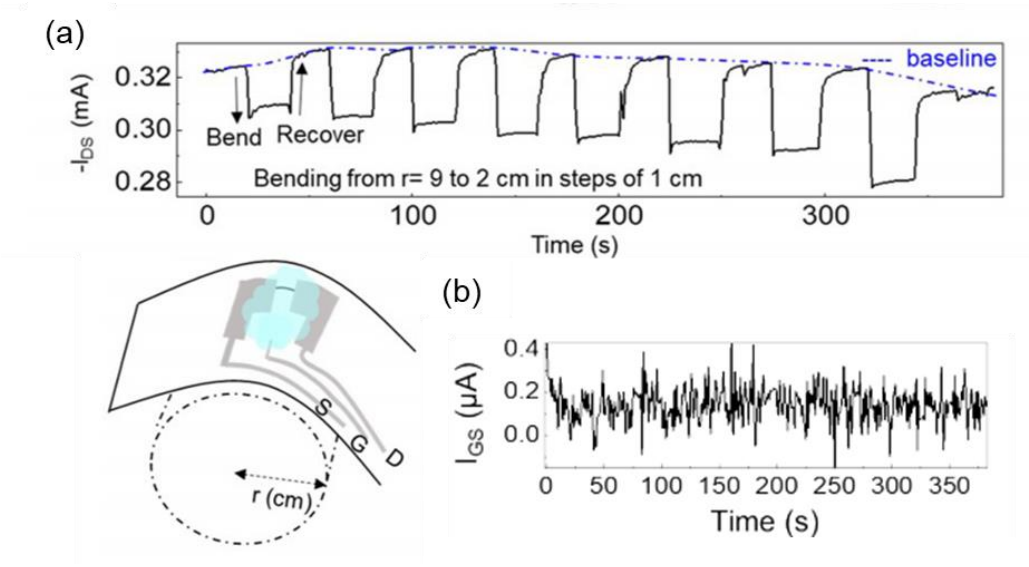

Figure 4.6. Bending response of curvature sensor. (a) I_{DS} versus time under various bending radii, with an illustration showing the experimental configuration for calibrating the curvature OECTs sensor. (b) real-time I_{GS} monitoring

The amplification of OECTs curvature sensor has been extracted by examining the transconductance (g_m) with respect to bending radius in Figure 4.7a. the g_m was reduced with

increasing curvature, comparable to other strain measurements on PEDOT films. This trend was generally explained by percolation effects[48], that the applied strain stretches the semiconductor, disrupts conductive paths, and hence decreases the g_m. This level is comparable to most of other similar prior works within this range of curvature. Furthermore, in Figure 4.7b, the bending signal showed a less linear relationship at V_{GS}=0 V compared to V_{GS}=-0.2 V, indicating the advantage of using the OECTs structure as a curvature sensor.

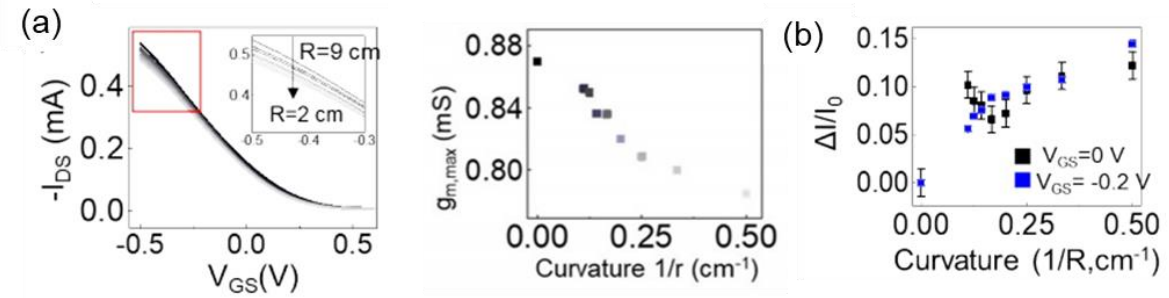

Figure 4.7. Curvature responses. (a) Transconductance (g_m) with respect to bending radius. (b) Signal response with V_{GS}=0 or -0.2 V, representing the signal amplification or not.

The calibration curves for the two OECT curvature sensors with their corresponding calculated surface strains are summarized and displayed in Figure 4.8a. These results demonstrate the high reproducibility of our proposed fabrication technique. The mechanical robust and fast response of device to different level of step curvature changes has been determined in Figure 4.8b. The OECT curvature sensor exhibits a rapid signal response even when the velocity of stage movement is modulated from 0.5 to 50 cm/s. Furthermore, the conductance of the device remains intact after the experiments, indicating the robust mechanical strength of the electrodeposited PEDOT:PF_6 fibers.

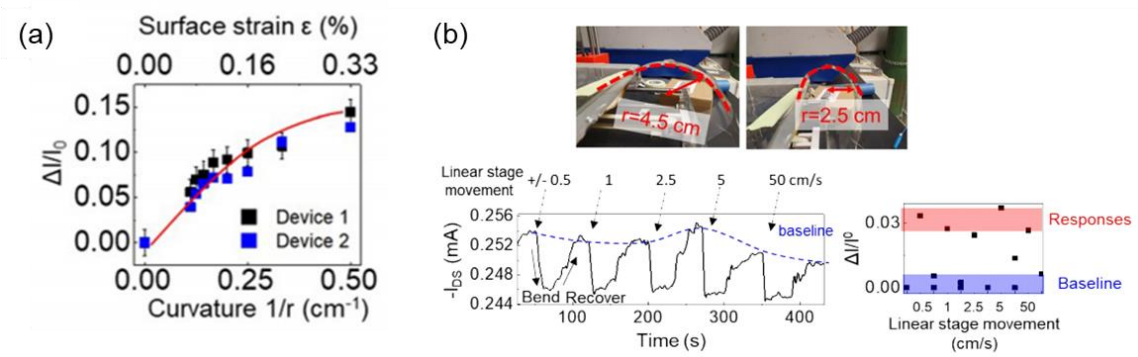

Figure 4.8. Reproducibility of curvature sensor. (a) Ratio of current change as a function of bending curvature. (b) Bending tests under different speeds, with the radii of curvature compressed from 4.5 cm to 2.5 cm as shown in the photographs.

The data $\Delta I/I_0$ versus curvature 1/r was fitted to the empirical exponential equation for the future *in-situ* application.

$$y = -a\ exp\left(-\frac{x}{b}\right) + c,$$

where fit parameters a = 0.153, b = 0.228 cm^{-1}, c = 0.155, with an excellent coefficient of determination R^2 = 0.97. Moreover, the gauge factor (GF) was also derived according to the equation[53].

$$\frac{\Delta I}{I_0} = GF \times \varepsilon, \varepsilon = \frac{d}{2r}$$

where ε is the surface strain, d is the substrate thickness equivalent to 130 μm in this work. The sensor GF was ~35 when the radius of curvature was greater than 5 cm ($1/r < 0.2\ cm^{-1}$), and GF dropped to 20 with bending radius below 5 cm. While the achieved GF is not the highest reported in literature (but serve the second place) in Figure 4.9, it falls within the typical range of most OECT strain sensors. Moreover, this encapsulation-free OECT curvature sensor has remarkable advantage that can be operated with stability under seawater environment.

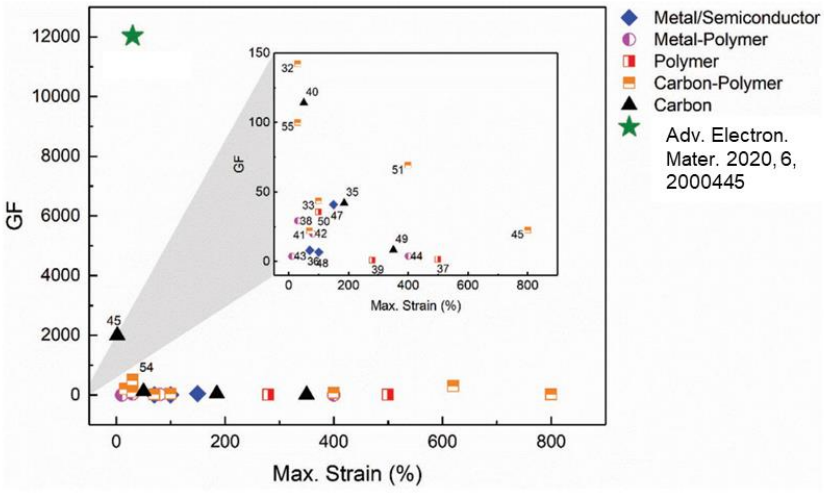

Figure 4.9. Reprint diagram of GF vs Strain (%) from ref[54]

The strain response in bending direction was also determined as shown in Figure 4.10. The OECT curvature sensor showed a uniaxial strain response, with a much lower resistance change when the applied strain was perpendicular to the fiber length, highlighting the importance of fiber alignment with the bending strain direction to maximize the effect of structural deformation and enhance GF.

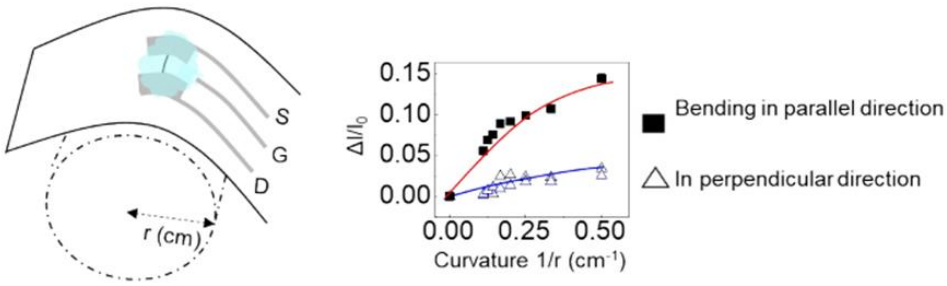

Figure 4.10. OECTs curvature sensor bending in perpendicular to direction.

4.3 Environmental sensors integration and sensitivity calibration

This section will outline the novel integration technique and sensors calibration curves for the environmental sensors (DO and salinity). As mentioned in the 4.1, the environmental sensors would share the common reference and counter electrode for the device footprint and stable reference signal overtime. Device integration and fabrication flow has been summarized in the Figure 4.11.

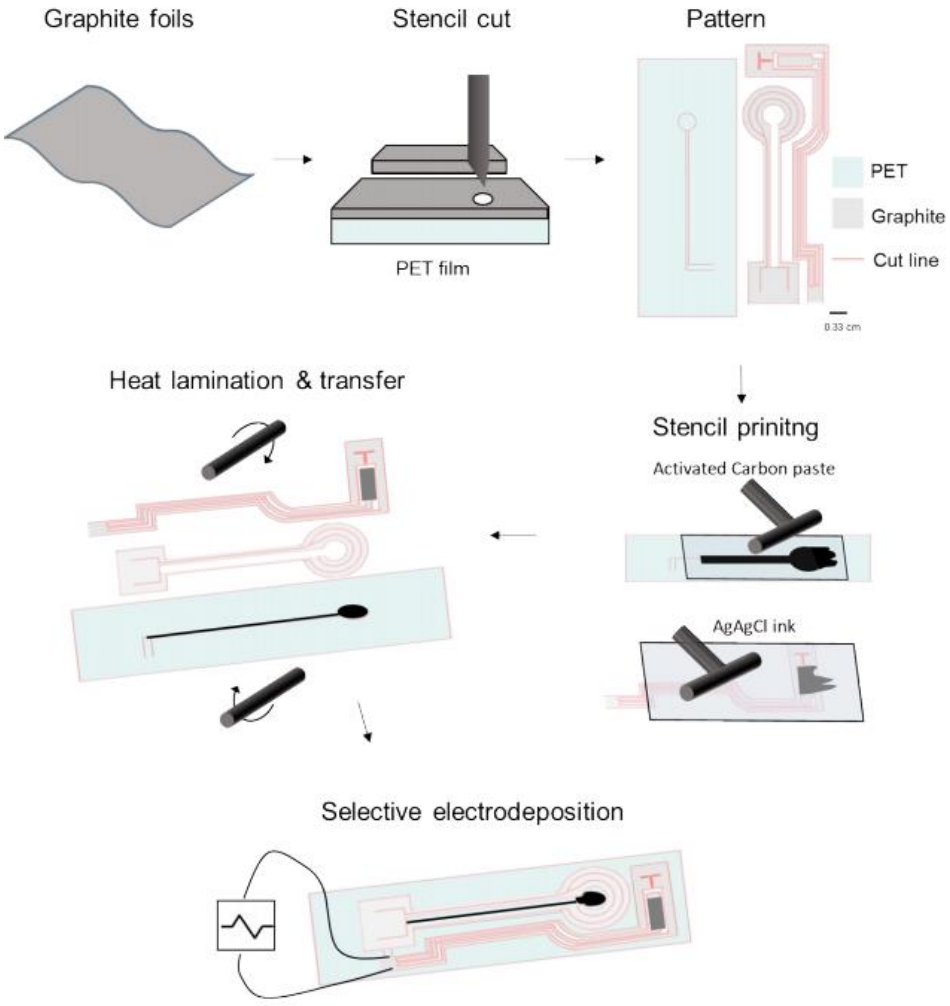

Figure 4.11. The fabrication flow for integrated ocean sensor

The design of concentric-ring electrodes for amperometric DO and salinity sensors minimized the device footprint. Each ring was separated by a gap of 125 μm from neighboring rings. The electrode patterns in Figure 4.11 were cut from graphite foils by a digital blade-cutter (Silhouette Cameo). The graphite cut-outs were laminated onto the PET substrate by pressing them together at 150 °C for ten seconds. Then Activated carbon (AcC) was deposited onto the surface of the reference electrode by stencil printing to increase electric double layer capacitance in the reference electrode for DO and salinity sensors. The gate electrode of the OECTs curvature sensor was modified by stencil printing Ag/AgCl ink (Ercon part #E2414), which reduced the series resistance of the gate for an applied voltage to drop mainly across the electrolyte and semiconductor channel. The stencil-printed materials were dried at 85 °C for 20 minutes.

Subsequently, two electrodeposition processes were carried out, one on the working electrode of the DO sensor and the other on the OECTs to form semiconducting fibers for channels. For the DO sensor, the reaction catalyst was platinum, and the working electrode surface was modified by electrodepositing platinum nanoparticles from a platinized carbon cloth (40%, Pt-C) through a linear sweep voltammetry scan, applying 1.2 to 0.8 V for five cycles scanning at -50 mV s^{-1} on the platinized carbon cloth. Electrodeposition of semiconducting fibers to bridge the OECTs channel (250 μm in length) was done through a mixed solution of 10 mM 3,4-ethylenedioxythiophene (EDOT) and 1 mM tetrabutylammonium hexafluorophosphate ($TBAPF_6$) in propylene carbonate solvent. The deposition voltage was a triangular waveform of ±10 V switching at 12.5 Hz, applied between the two graphite source and electrodes. The deposition time was around 10 minutes until the deposition current reached saturation. Finally, the graphite interconnects were connected to aluminum wires through silver paste. The bonding area between

the sensor tag and the aluminum wires was encapsulated by silicone elastomer (Ecoflex) to avoid contact between the wires and seawater during measurements.

4.3.1 Salinity sensor calibration

The integrated ocean sensor was used to calibrate its sensitivity to different salt concentrations in seawater. This salinity sensor works on the principle of electrochemical detection, which leverages the inherent properties of ionic conductivity to determine the amount of salt present in a target ocean sample. The salinity sensor detected the ionic current ($I_{salinity}$) through seawater samples using graphite electrodes (served as WE and REF/CE) at a bias of -0.2 in Figure 4.12a. The calibration of $I_{salinity}$ versus salinity is shown in Figure 4.12b at the temperature of 23 °C. The sensitivity was extracted to be 0.013 μA cm^{-2} per g kg^{-1}. The working range is 4-40 g kg^{-1}.

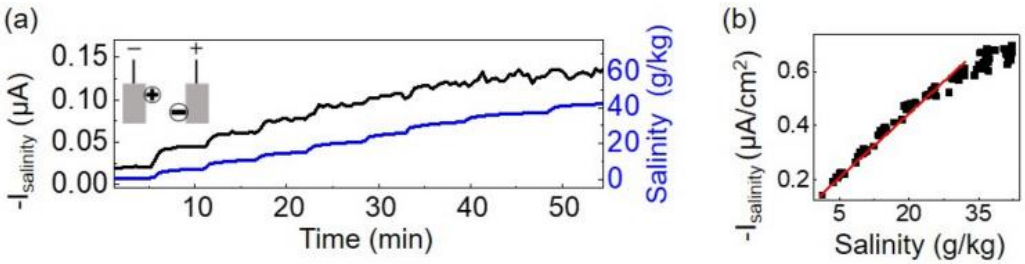

Figure 4.12. Salinity sensor. (a) Current measurement by the printed salinity sensor biased at −0.2 V (black) and readings from the commercial meter (blue) as the sample salinity was increased over time. The inset illustrates the ionic current between sensor electrodes. (b) Calibration characteristics showing the sensor current density versus salinity

4.3.2 Dissolved oxygen (DO)

The integrated ocean sensor was used to calibrate the sensitivity of dissolved oxygen (DO) in seawater. This DO sensor is based on the electrochemical detection principle, specifically inducing the oxygen reduction reactions (ORRs) with a three-electrode system consisting of a working electrode, reference electrode (AcC), and counter electrode within this integrated sensor design.

The deposited Pt-C serves as the working electrode, and a bias of -0.8 V was found to induce ORRs, as shown in Figure 4.13a. This onset potential is within the range of ORRs potentials found in Chapter 1. Note that the accuracy of amperometry measurements is closely related to the ionic strength, which is mostly determined by the amount of salt in seawater in this study. Therefore, the calibration of DO sensitivity should consider the different ranges of salinity. Then, the reaction current I_{DO} was measured under a potential of -0.8 V with respect to the reference electrode of AcC. The change in I_{DO} was recorded as DO concentration was adjusted by gas purging or by adding salt, as shown in Figure 4.13b. The sensitivity of DO sensor was 2.42 μA ppm^{-1} in Figure 4.13c, with no significant interference from changing salinity between 7.5-28 g kg^{-1}. The response of the DO sensor slightly increased only when the salinity exceeded 38 g kg^{-1}, which is attributed to the higher background ionic current. Based on our analysis, the detection limit of this amperometric DO sensor was determined to be 0.5 ppm.

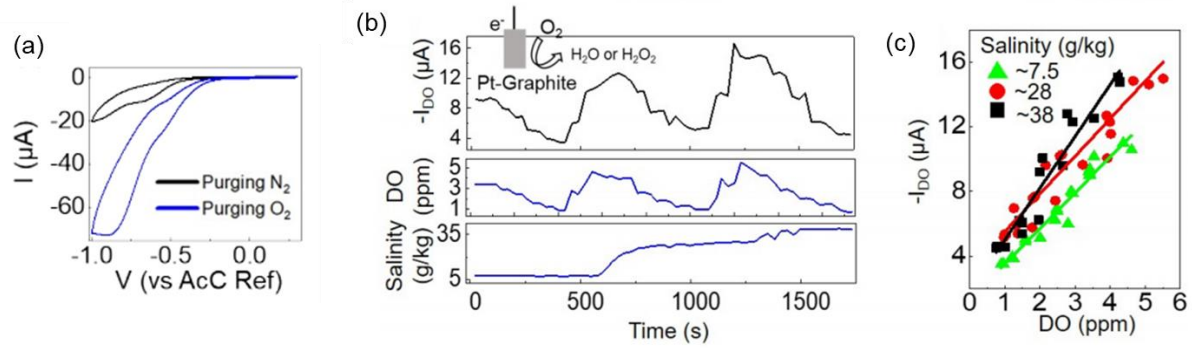

Figure 4.13. Dissolved sensor. (a) Current-voltage measurements using a three-electrodes system to determine onset potential of ORRs. (b) Current measurement by printed dissolved oxygen sensor biased at -0.8 V (black) and readings from the commercial meter (blue), as oxygen concentration and salinity were adjusted. The inset illustrates oxygen reduction reaction at the sensor working electrode. (c) Calibration characteristics showing the sensor current versus dissolved oxygen concentration at three levels of salinity

As a result, we summarize the performance of integrated ocean sensor in the Table 4.1.

Table 4.1. Performance summary in integrated ocean sensor

Sensor	Detection accuracy	Detection limit	Detection range	Sensitivity	Device size
Curvature	±0.5%	1 cm^{-1}	0.11–0.5 cm^{-1}	GF of 35 to 20	0.3 cm^2
Salinity	±0.7 g kg^{-1}	4.3 g kg^{-1}	4–40 g kg^{-1}	0.013 μA cm^{-2} per g kg^{-1}	0.2 cm^2
Dissolved oxygen	±0.2 ppm	0.5 ppm	0.5–6 ppm	2.42 μA ppm^{-1}	0.32 cm^2

4.4 Multiplexer and program

To obtain real-time data from our integrated ocean sensor, we developed a custom Multiplexer control system (MUX) with external potentiostat. The purpose of using MUX was to reduce interferences between the operations of different sensors and requiring only one external potentiostat. This section will provide a detailed overview of the MUX's operating principle, noise interference between MUX channels, and wiring connections. In this work, the MUX board circuit was designed to interface with the integrated ocean sensor, allowing for sequential readout of the sensors that was controlled by the external potentiostat. The connections to sensors have been already summarized in detail in Figure 4.1. The MUX board circuit used in this work included four 8-to-1 multiplexer chips (74HC4051) and a Nano-Arduino purchased from Sparkfun. The multiplexer channels were controlled by the Nano-Arduino through three select-lines (S0, S1, and S2), which were connected to the Arduino analog outputs A0, A1, and A2. The output channels of the multiplexers were connected to a portable potentiostat (Metrohm μ300) for data acquisition. The 5 V required to power the Nano-Arduino and multiplexers were supplied by a computer. The multiplexer circuit was soldered onto a small piece of gold-plated printed circuit board and served as digital switches between channels. The example of 4:1 MUX operation has been displayed in Figure 4.14a.

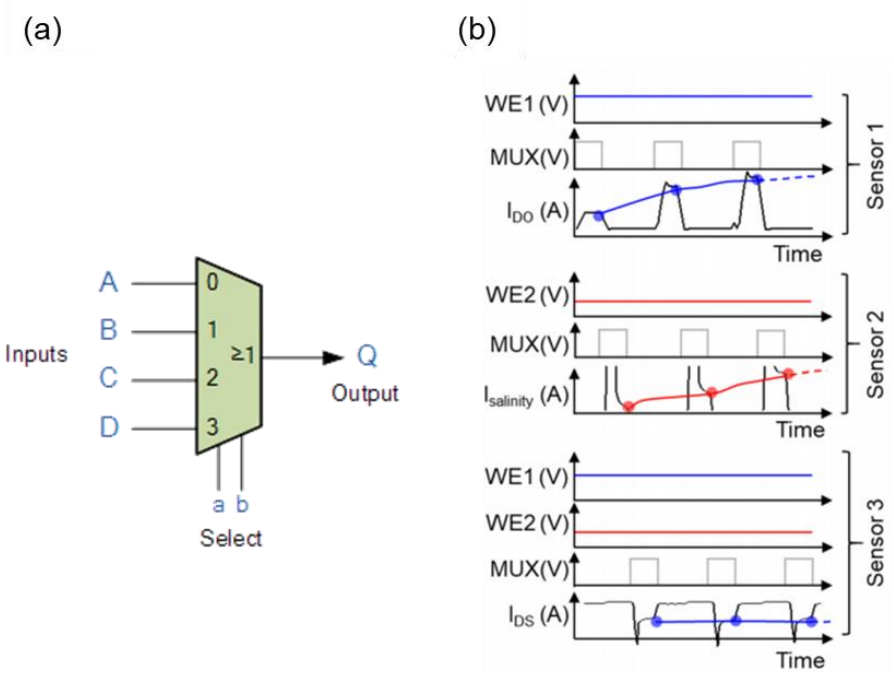

Figure 4.14. Multiplexer operation. (a) Example of MUX operation. (Taken from electronics-tutorials.com) (b) Timing diagram of control and measurement signals for three sensors, under sequential readout switched by the multiplexer circuit interfacing with the potentiostat. The solid dots indicate steady-state measurement points near the end of each sampling period.

The sequential data acquisition for three sensors in our customized integrated MUX system has been demonstrated in Figure 4.14b. The timing diagram displays the sequence of switching the multiplexer control signals (MUX) to each sensor. The MUX signal was activated at the selected sensor, and the bias on the WE channel was delivered to the active device, while the current at the CE channel was measured. The MUX was programmed to have a 10-second on-period, and the readout data near the end of each period was used to ensure accurate detection, as the transient current spikes from voltage switching had settled, and the sensor had reached a steady state. The detailed circuit board and control program has been shown in Figure 4.15.

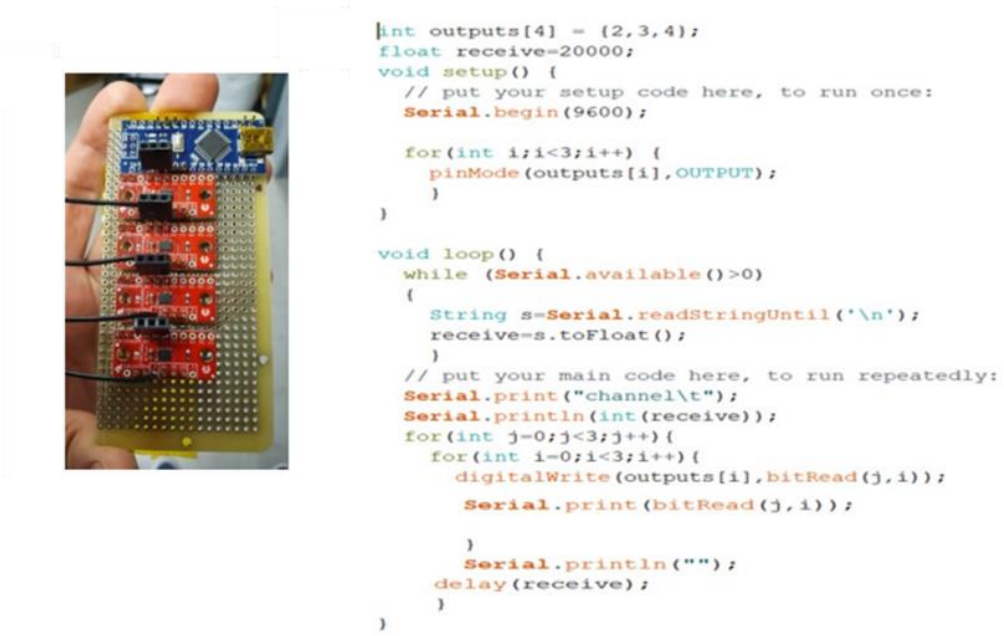

```
int outputs[4] = {2,3,4};
float receive=20000;
void setup() {
  // put your setup code here, to run once:
  Serial.begin(9600);

  for(int i;i<3;i++) {
    pinMode(outputs[i],OUTPUT);
    }
}

void loop() {
  while (Serial.available()>0)
  {
    String s=Serial.readStringUntil('\n');
    receive=s.toFloat();
    }
  // put your main code here, to run repeatedly:
  Serial.print("channel\t");
  Serial.println(int(receive));
  for(int j=0;j<3;j++){
    for(int i=0;i<3;i++){
      digitalWrite(outputs[i],bitRead(j,i));
       Serial.print(bitRead(j,i));

       }
       Serial.println("");
    delay(receive);
     }
}
```

Figure 4.15. The MUX circuit board and codes in Arduino program

To ensure accurate readings and reduce interferences between sensors, it is important to investigate the intrinsic MUX channel leakage during switching, especially given the shared reference and counter (and source/drain in the curvature sensor) electrode out of proposed design. Therefore, the noise standard deviation from neighboring channels were determined to be around 3.5 nA while we applied the largest potential (-0.8 V) in the adjacent channels, as shown in Figure 4.16a. The resolution of data acquisition in this work was determined to be below 10 nA, which allowed for clear differentiation of μA level signals from stimuli. The switching speed of the MUX system is significantly faster than the few-second response time of the sensors, as demonstrated in Figure 4.16b.

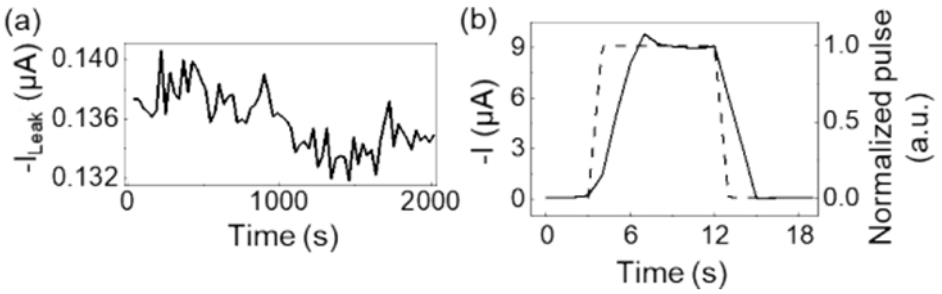

Figure 4.16. Channels leakage in MUXs. (a) Leakage current from neighboring MUX channels. (b) Device response time upon switching. The solid line was the device current, and the dashed line was the triggering pulse.

4.5 Application for oyster gape openings under stimulus

The integrated ocean sensor was now applied on oysters, as illustrated and photographs in Figure 4.17, as they are reef-building organisms that provide habitat for various commercially and environmentally important organisms, such as fish and crustaceans. Non-intrusive, compact integrated ocean sensor that can be attached to marine species like oysters are in high demand to gather local environmental data and correlate it with organism physiology, migration behaviors, and compensatory responses to adverse conditions.

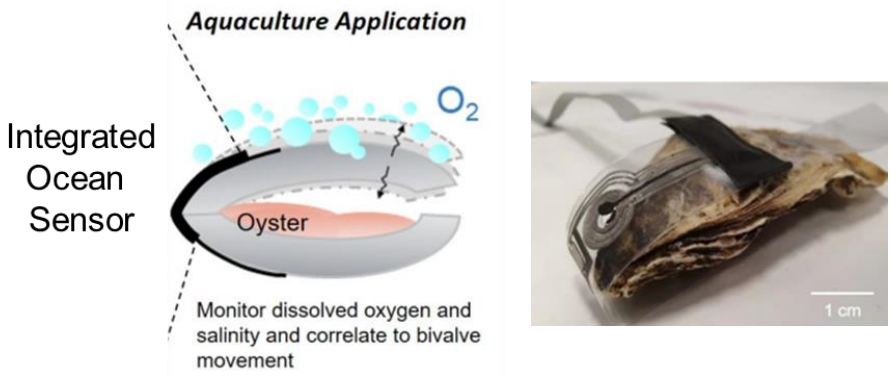

Figure 4.17. Schematic and photographs of integrated ocean sensor on oyster. Measurements would carry out in the water tank filled with artificial seawater.

The oyster was chosen for this study due to its stationary nature and the fact that the gape opening responds clearly to changes in various dissolved oxygen levels. The integrated ocean

sensor, consisting of dissolved oxygen and salinity sensors as well as a curvature sensor, was used to monitor the surrounding environment and the level of gape opening of the oyster, as illustrated in Figure 4.17. Figure 4.18a depicts a still frame of the oyster's response to oxygen purging, providing evidence of its gape behavior in response to dynamic oxygen levels and illustrating the generality of this biological response. In Figure 4.18b, only the curvature sensor was used on the oyster and the level of dissolved oxygen was calibrated using commercial probes. The oyster exhibited active gape opening and closing when the DO level was above 3 ppm, as indicated by the increasing fluctuation frequency. Compared to video recording, the curvature sensor consumed significantly less power and could operate in the dark without disturbing the circadian cycle of the organisms.

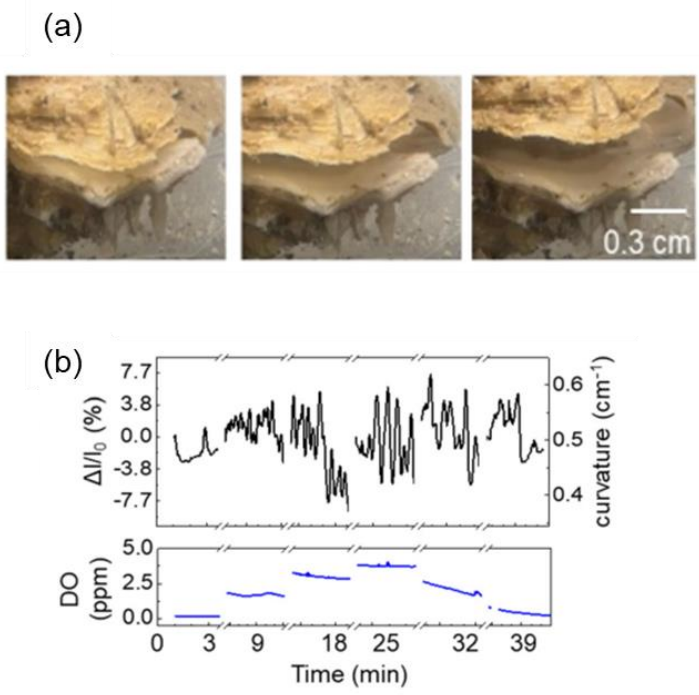

Figure 4.18. Oysters demo (a) Frame of oyster gape opening in dissolved oxygen stimulus. (b) Changes in curvature tracking the oyster gape under different dissolved oxygen levels with data sampling at 1 Hz.

The resolution of gape opening was capable to be distinguishable in sub-mm level by the previous noise deviation results. The curvature sensor readout channel had a noise level of 0.01 μA with the current signal centered at 52 μA. Using the ratio of $I_{noise}/I_0 = 0.01/52 = 2 \times 10^{-4}$, the noise around the curvature measurement was calculated to be 1/r ±0.002 cm^{-1}. For instance, when the measured $\Delta I/I_0 = 0.136$ corresponding to a curvature of 0.477 cm^{-1}, the curvature accounting for noise uncertainty was 0.477 ±0.002 cm^{-1}. Hence, the upper and lower bounds of curvature 1/r were 0.479 cm^{-1} and 0.475 cm^{-1}, respectively, which translated to radii of 2.088 mm and 2.105 mm, respectively shown in Figure 4.19.

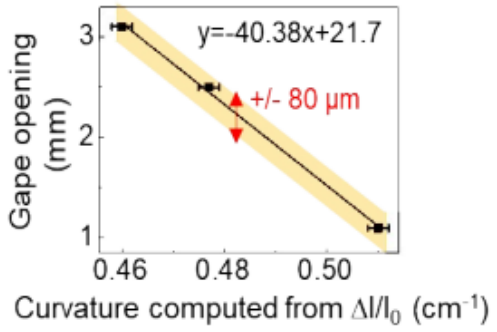

Figure 4.19. The correlation between the gape distance extracted from photographs and the measurements obtained from the curvature strain sensor attached to the oyster shell. The shaded region represents the uncertainty levels of the measurements.

Figure 4.20 displayed an observation period of over 80 minutes, during which the integrated ocean sensor was used to measure DO, salinity, and curvature simultaneously. The top, middle, and bottom data lines represent the curvature sensor, dissolved oxygen sensor, and salinity sensor, respectively, while the blue data lines are from nearby commercial sensors. The MUX switching with the timing sequence was used to record the data. Consistent with earlier trials, increased DO levels led to more frequent oyster gape movements. The salinity readings remained constant and unaffected by gas purging, as the salinity level was not adjusted in this trial. While the long-term

stability of the integrated ocean sensor will be evaluated in future studies, the materials used in this work have previously manifested promising stability in week-long studies carried in marine environments or saline conditions.

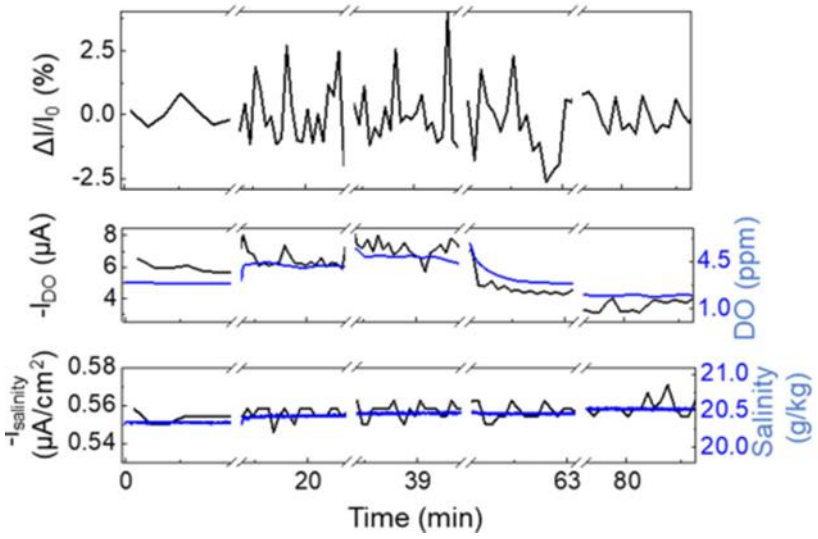

Figure 4.20. The integrated ocean sensor was used to measure the oyster's gape responses to changes in dissolved oxygen concentration and salinity, with a sampling rate of 0.016 Hz. The OECTs was biased at V_{GS} = −0.2 V and V_{DS} = −0.5 V, while the salinity and DO sensors were biased at −0.2 V and −0.8 V, respectively. The blue data lines in the figure represent measurements taken using a commercial multimeter to validate the accuracy of the printed sensors.

4.6 Conclusion

This study demonstrated the possibility of using an integrated ocean sensor system for monitoring various environmental parameters in aquaculture research in a cost-effective manner. The multiplexed setup allowed for the simultaneous detection of salinity and DO, and with the potential to add sensors for other parameters such as pH and temperature. The curvature sensor based on electrodeposited semiconducting PEDOT:PF_6 was robust and stable in seawater without the need for encapsulation. The small and non-intrusive ocean sensor can be potentially attached to multiple bivalves for group behavior studies and field use in the future. If a high percentage of bivalves close their gapes, it could serve as a prominent indicator of severe environmental

conditions when accounting for statistical variations in the sensors. Overall, this work demonstrated the design and fabrication processes to implement flexible electronics as compact data collection tools in marine studies.

Chapter 4, in part, is a reprint of the material as it appears in Nanoscale. Shuo-En Wu, Napasorn Phongphaew, Yichen Zhai, Lulu Yao, Hsun-Hao Hsu, Alan Shiller, Jason David Azoulay and Tse Nga Ng, 2022. Point-of-use printed nitrate sensor with desalination units. The dissertation author was the primary researcher and author of this paper.

CHAPTER 5: RETINOMORPHIC MOTION DETECTOR FABRICATED WITH ORGANIC INFRARED SEMICONDUCTORS

5.1 Challenges for underwater motion detection

Monitoring the movement, vibration, and interaction of target objects in seawater is crucial for some fields of marine studies. Different kinds of position trackers have been developed over the decades to gather diving parameters for marine species. However, the bulky size and power consumption of these trackers pose a challenge and limit their use. Recently, there is a growing demand for high-speed motion detection in various applications such as autonomous vehicles, robotics, and surveillance systems. To address this need, neuromorphic electronic systems have been developed as a promising alternative to traditional CMOS-based systems[23]. These artificial visual perception systems, also known as retinomorphic devices, function as both sensors and processors, allowing them to detect sudden stimuli, store signals, and process multi-dimensional information in one single component simultaneously. Although various active inorganic/organic materials or prototypes with integrated memory/computation have been used to show the concept of retinomorphic applications, the detection wavelength range is mostly limited to the UV-vis region, will potentially lead to inaccurate data acquisition for marine species research. To overcome this challenge and enhance the validity of acquired data in marine studies, it is essential to develop an organic retinomorphic infrared detector that can response to changes of short-wavelength infrared light (SWIR), which offers the potential advantages, such as energy-efficient, event-driven information processing, scalability, and high temporal resolution to noise.

5.2 SWIR retinomorphic device configuration, design and features

This section provides detailed information about concept of device design, device fabrication and features of device in electrical behaviors. We develop an organic retinomorphic device capable

of capturing a SWIR light stimulus within only few microseconds (μs), remarkable signal-to-noise response (SNR~3) under ultra-weak light pulse at 8 nW/cm^2. The design of this prototype is based on a resistor-capacitor (RC) circuit, which utilizes the capacitive-resistor effect to detect changes in light signal.

5.2.1 Device configuration

Figure 5.1 shows a schematic diagram of the fundamental RC high-pass configuration, which comprises a capacitor (MIScap) and a resistor. Capacitor MIScap is fabricated based on Photodiode structure. A multilayered photodiode is fabricated with organic bulk heterojunction (BHJ) active layer in the blend with narrow bandgap of semiconducting p-type polymer CDT-TQ (AN9) and n-type acceptor $PC_{70}BM$, n-SnO_2 and MoO_3 served as electron and hole collecting layer, transparent ITO and silver as cathode and anode, respectively. This multilayered photodiode has been demonstrated to be highly sensitive to infrared light in the NIR-SWIR wavelength range of 600 to 1550 nm in our previous works[55,56]. The structure of MIScap is built upon conventional Photodiode; an electrical insulated AF teflon was inserted in-between MoO_3 and Ag layer. The role of teflon will be served as capacitance layer to store/discharge carriers from neighbor terminals. Therefore, MIScap shares the architecture of Metal-Insulator-Semiconductor, as we attempt to draw the similar functionalities with well-known Metal-Oxide-Semiconductor (MOS) capacitor.

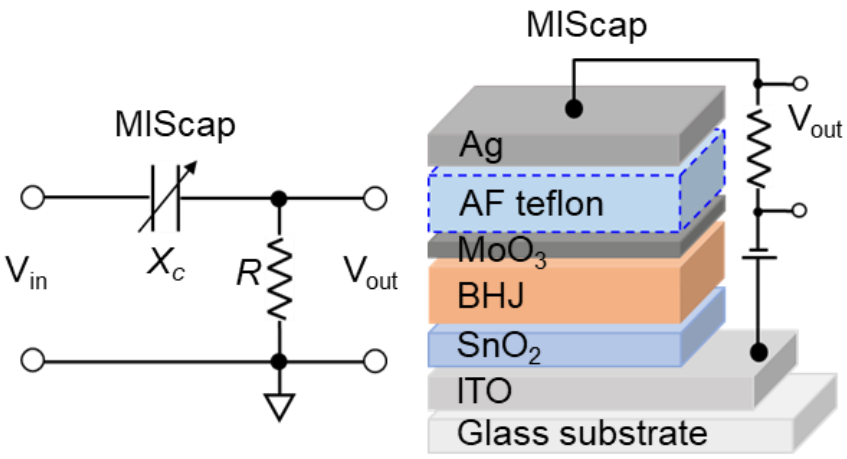

Figure 5.1. Schematics of high-pass configuration and structure of infrared photoresponse capacitor (MIScap).

In this work, MIScap is taken as the capacitive component in series with external load resistor (R) to constitute proposed high-pass RC filter circuits. Note that retinomorphic sensor constitute by MIScap with external load R. During device operation, the input voltage (V_{in}) was applied across the capacitor MIScap and load resistor R. Upon the irradiance from incident light on MIScap, change of reactance (X_L) leads to proportional change of V_{out} (V_{in}-X_L) in the load resistor R, reflecting signals displacement over the short period of time in μs timeframe. Therefore, we took V_{out} as a new indicator to evaluate the retinomorphic sensor performances under dynamic infrared light conditions in the following section.

5.2.2 Materials synthesis and device fabrication

Materials preparation

The narrow bandgap polymer (poly(4-(5-(4-(3,5-bis(dodecyloxy)-benzylidene)-4H-yclopenta[2,1-b:3,4-b0]dithiophen-2-yl)thiophen-2-yl)-6,7-dioctyl-9-(thiophen-2-yl)-[1,2,5]thiadiazolo[3,4-g]quinoxaline))(CDT-TQ) was synthesized on the basis of ref[55]. The acceptor [6,6]-phenyl-C_{71}-butyric acid methyl ester ($PC_{70}BM$) was purchased from Ossila Ltd. The AF teflon solution was purchased from Chemours (AF2400) and ready-to-use after received. The

CDT-TQ, $PC_{70}BM$ and Camphoric acid (CA) were blended at 2:4:1 weight ratio dissolved in 1,2-dichlorobenzene at a concentration of 28 mg mL^{-1}. An additive 1,8-diiodooctane was added to the blend at a volume ratio of 3%. This BHJ blend solution was stirred at 70 °C for at least 24 hours in the glovebox. The precursor solution of SnO_2 was prepared by dissolving $SnCl_2 \cdot H_2O$ in ethanol at concentration of 0.07 M, and then stirred in a water bath at 80 °C for 8 hours[55,56].

Device Fabrication

ITO substrates were preclean by detergent, deionized water and sonication by isopropanol and acetone. The electron-transport layer SnO_2 was prepared through spin-coating the precursor solution at 3000 rpm for 40 s, followed by annealed at 180 °C for 1 hour with thickness ~20-40 nm. The substrates were then transferred to a nitrogen-filled glovebox for further deposition. The BHJ blend solution was spin-coated at 2000 rpm for 40 s on top of the SnO_2 layer to form a film with a thickness of 200 nm. Afterwards, for MIScap, the teflon solution was spin-coating atop of BHJ layer at 1500 rpm for 40s in three times and left to stand overnight. Consequently, 10 nm molybdenum oxide (MoO_x) and 100 nm Ag layer were thermally deposited through a shadow mask, defining an active area of 0.09 cm^2 for both retinomorphic sensor and Photodiode. All the devices were encapsulated and placed in the ambient condition for further characterization. Energetic diagram of materials and their structure has been summarized in Figure 5.2.

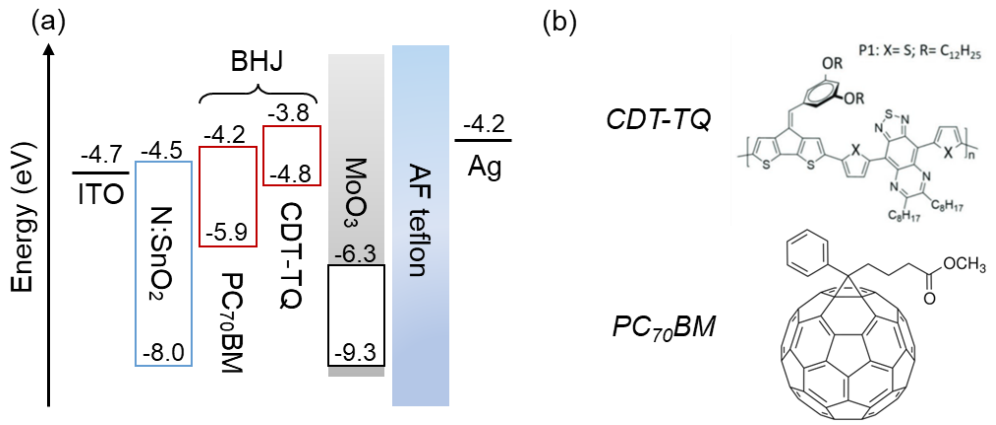

Figure 5.2. (a) Energy diagram for the materials used in this work. (b) Molecular structure of donor and acceptor in BHJ.

5.2.3 Device features on light stimulus

To demonstrate the fundamental difference of Photodiode and retinomorphic sensor, Figure 5.3 compares the electrical characteristics of Photodiode in current and retinomorphic sensor in V_{out} with a pulse of 500 Hz light on/off under light intensity ΔP=8 mW/cm^2. The current in Photodiode exhibited a typical clear onset and became saturated within a few ms during timeframe of irradiance. Instead, V_{out} of retinomorphic sensor only produced the temporal spike behavior after light on or off within few μs, signifying a fundamental difference in working principle between Photodiode and retinomorphic sensor. The spike behavior can be interpreted as a delay in the signal response due to the resistive-capacitive effect from the external load resistor R and the capacitor MIScap after triggered by a light pulse. Thus, retinomorphic sensor is featured to be only responding to changes in illumination levels rather than static illumination.

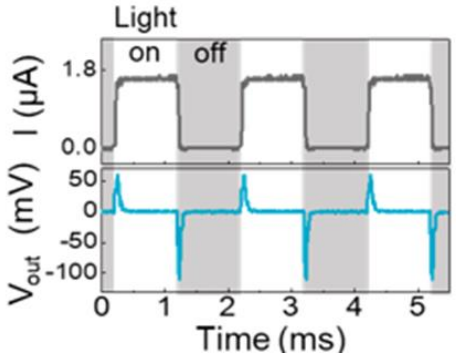

Figure 5.3. Characteristics between regular Photodiode (Black) and retinomorphic sensor (Blue) with a pulse of light.

5.3 Intensity modulated photovoltage spectroscopy (IMVS)

Given the total insulating electrical property of inserting teflon in MIScap structure, making it challenging to investigate the charge transporting/accumulating within the structure or photoresponse. The typical characterization techniques used in the study of photodiodes, such as I-V characteristics or electrochemical impedance spectroscopy (EIS), require photocurrent signals which are loss in MIScaps as shown in Figure 5.4.

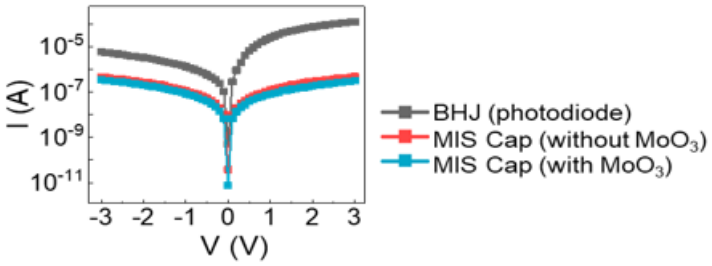

Figure 5.4. Failure analysis of MIScap on photoresponse by I-V characteristics.

As a result, we introduce the intensity modulated photovoltage spectroscopy (IMVS) to investigate light-induced capacitance effect by recording the shifting photovoltage (with phase shift φ) of MIScaps or Photodiode with modulated light source as shown in Figure 5.5a. IMVS is a widely used technique for studying charge properties in various types of solar cells and dye-

sensitized solar cells (DSSCs) under open-circuit condition[57]. The generated carriers by perturbing light irradiance create photovoltage variations to the ground, which can be measured and analyzed as principle of IMVS technique[58] depicted in Figure 5.5b. By analyzing the transfer function of light-to-voltage (perturbing illumination/perturbed voltage) in open-circuit condition, the characteristic recombination time constant (τ_{rec}) of charge within structure can be derived, hereby providing insight into the energetic state of the accumulating/transporting carriers in MIScaps.

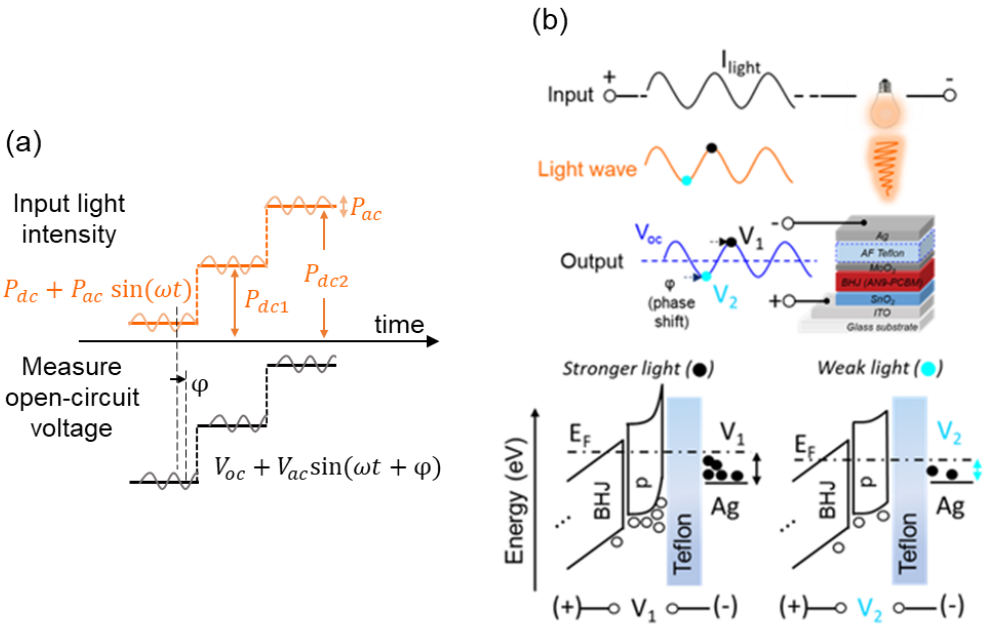

Figure 5.5. IMVS technique. (a) The operating principle of IMVS technique. (b) Schematic of perturbing light with respect to receiving device voltages output in IMVS technique.

To demonstrate the capability of the IMVS technique, three distinct device structures were analyzed and compared, as depicted in Figure 5.6a-c. The use of insulated teflon in MIScaps provided the advantage of reduced quenching from external circuits compared to Photodiode. Additionally, the inclusion of an extra layer of p-type semiconducting material (MoO_3 in this study) shall help to increase the distance between hole accumulation and recombination center, hence reducing the recombination rate as demonstrated in Figure 5.6b.

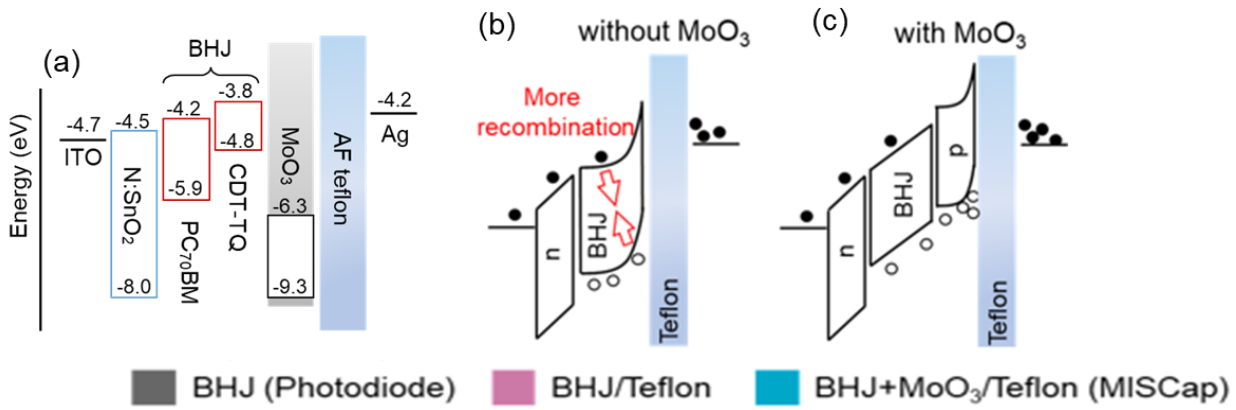

Figure 5.6. Device structures used for IMVS evaluation (a) Photodiode (b)MIScap without p-layer. (c) MIScap with p-layer.

A sinusoidal waveform of 980 nm infrared light with intensities ranging from 0.5 to 8 mW/cm^2 is employed. In Figure 5.7a, both devices exhibit a proportional increase in photovoltage with increasing light intensity, which eventually reached saturation at 8 mW/cm^2. These results are consistent with the findings in Photodiodes, where short-circuit currents (and its open-circuit voltage) have been shown to monotonically increase with light intensity[56,59]. As expected, the MIScaps shows a larger modulated voltage compared to Photodiode, indicating a more energetic charging state with larger potential offset across the teflon. Simultaneously, a summary of the relationship between the modulated light frequencies and intensities for all structures was presented in the form of Nyquist plot in Figure 5.7b. The plot clearly demonstrates a typical semicircular shape with a shrinking radius in higher light intensities as a function of applied frequencies by the derived transfer equations.

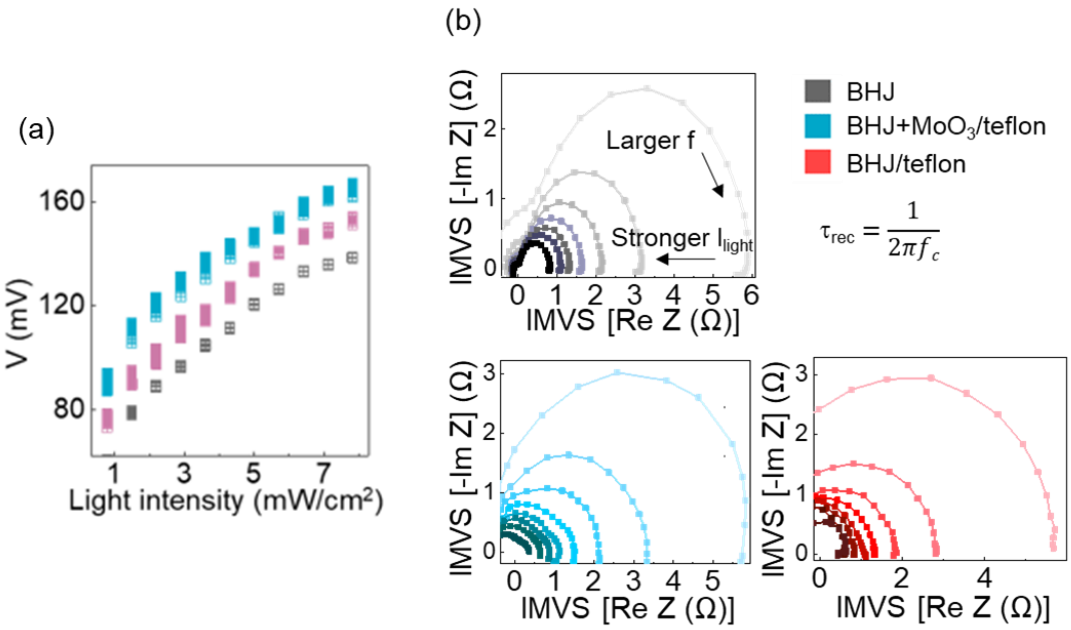

Figure 5.7. (a) Recorded voltages under controlled perturbing light condition for three structures. (b) Nyquist plot of capacitive reactance with respect to light intensity for all structures

The light-induced capacitive effect is highlighted by comparing the imaginary component of impedance with applied frequencies for all structures in Figure 5.8a. Photodiode has the dominant capacitive effect in frequency around 100 Hz, which is one order higher than MIScaps. This indicates that the regular Photodiode has effective charge extraction state as the neighboring Ag electrode is utilized for efficient charge collection during device operation. Instead, the charge collection pathways in MIScaps are blocked by teflon, leading to a null of charge extraction and hence higher charge transfer resistance at lower frequencies. Consequently, Figure 5.8b summarizes the longer carrier lifetime in MIScaps with that in the photodiode. The characteristic recombination lifetime τ_{rec} (=$1/2\pi f_c$, where f_c is taken from the lowest point of semicircle in the Nyquist relationship) is an important indicator that evaluate carrier recombination rate.

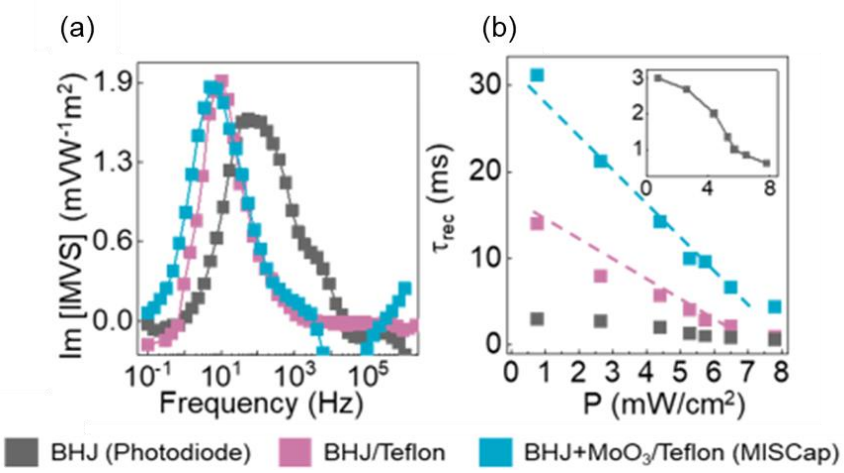

Figure 5.8. Results from IMVS. (a) Light-induced capacitive element investigation by imagery reactance verse applied frequencies. (b) Extracted characteristic recombination lifetime (τ_{rec}) for all structures.

Notably, we attempt to draw the relationship between τ_{rec} and light intensity for Photodiode and MIScaps, which might emphasize the fundamental differences in charge transport/accumulation between these two structures. In Photodiode, τ_{rec} has saturated in light intensity below 3 and above 7 mW/cm^2. Instead, τ_{rec} in MIScaps has a linear relationship when light intensity below 7 mW/cm^2. These relationships can be further explained based on the derived equations summarized below. The derivation of lifetime was taken from the ref[58], which is the simplest definition for a homogeneous system:

$$\frac{dn}{dt} = -U_n(n)$$

where n is volume density of electron. U_n (n) is recombination rate per unit volume as function of n. Therefore, a lifetime (τ_n) in term of recombination rate can be further derived to be:

$$\tau_n = -\frac{\Delta n}{U_n}$$

As expected, the characteristic τ_n is inversely proportional to the recombination rate. During the Photodiode operation, generated electrons would be collected through electrodes. Hence, we draw

a connection between accumulated charges and empirical equations commonly used in Photodiode studies that include incident light intensity and receiving photocurrent.

$$n \propto I = AP^{\theta}$$

where I is photocurrent, A is arbitrary constant, P is incident light intensity and θ is proportionality constant. This proportionality has built on the similarity of charge properties for both structures. In photodiode, n will be reflected to be photocurrent, collected by the electrodes[60]. In MIScap, n will be ensemble of charges, accumulated on the interfaces. As a result, we simply combine the equations above and derive the relationships for τ_n and light intensity P.

$$\tau_n = -\frac{A_1}{U_n} P^{\theta}$$

This relationship built the connection between τ_n from IMVS, recombination rate and θ related to trapping factors. Therefore, τ_{rec} is derived to be a function of recombination rate (U_n), light intensity (P) and proportionality constant (θ). This is the simplest homogeneous model that excludes the recombination rate from trapping factors and value of θ is associated with empirical equations in Photodiode studies that represent the presence of trapping states (generally <1). As a result, the saturated behavior of τ_{rec} in Photodiode is probably arising from the change of θ during different levels of traps involvement under various light intensities regime. Instead, the linearity between τ_{rec} and light intensity in MIScaps relationship might imply the device operation free from interfacial traps or neighbor electrodes influences (constant θ), only as function of recombination rate (U_n) associated with the locale densities of accumulated charges (n). Similarly, within MIScaps, the larger negative slope in MIScap with MoO_3 represents the smaller recombination rate than the one without. This derived relationship needs to be further confirmed in the future.

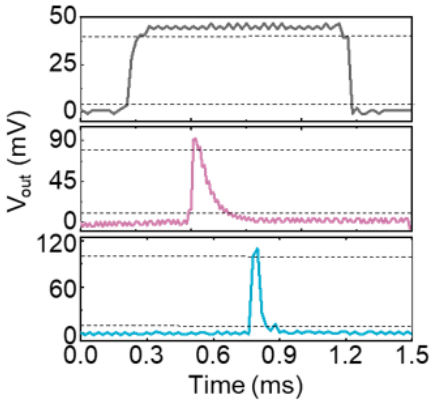

Figure 5.9. Responses for three structures within a temporal light pulse at 500 Hz

Three device structures were tested in a pulse of light and demonstrated their responses in Figure 5.9. With energetic barrier formation between MoO_3 layer and BHJ, reverse recombination has been effectively suppressed, therefore explain the positive correlation of extended charge lifetime and enhanced photoresponse of MIScap with MoO_3. These findings can be exploited in future organic retinomorphic device design principles.

5.4 Resistor-capacitor (RC) circuit analysis

The working principle of MIScap under high-pass configuration has been further delved. The signals output (V_{out}) of MIScap is adjustable with respect to external R from 10^3 to 10^6 Ω as shown in Figure 5.10b. Peak V_{out} is proportional to its response time, and after reaching the peak, V_{out} decays exponentially. These characteristics seem conform to the working principle of RC circuits.

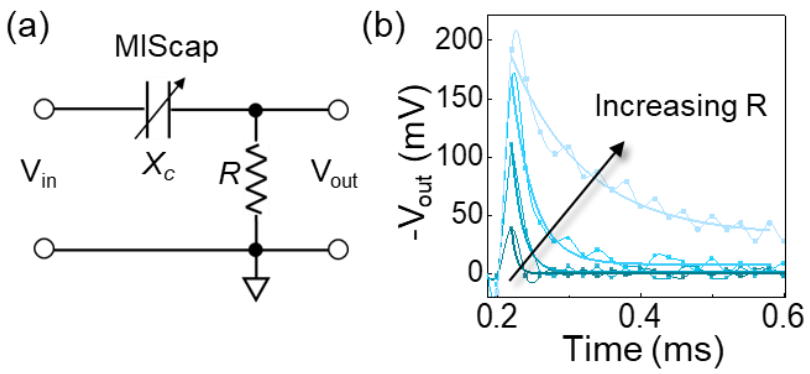

Figure 5.10. (a) RC high-pass circuit. (b) Signal outputs (V_{out}) with respect to external resistor (R) under ΔP =8 mW/cm^2 at zero bias.

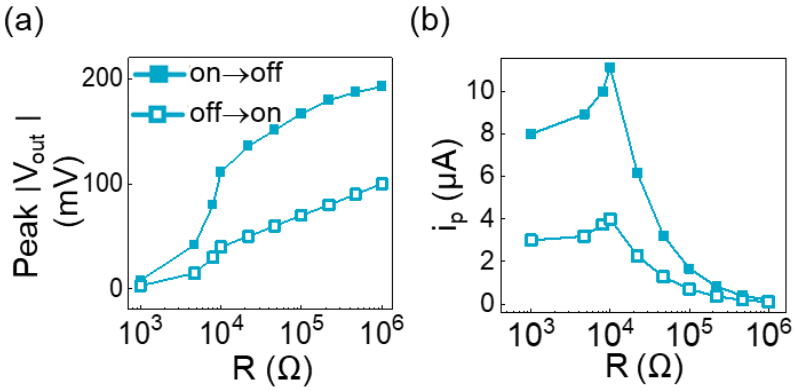

Figure 5.11. Output signal of MIScap with external load resistor R. (a) A summary of peak | Vout | during light on-off or off-on condition. (b) transient current on the external resistor (R).

To further analyze the connection between V_{out} of MIScap and principle of RC circuits, Figure 5.11a summarizes the peak V_{out} of MIScap with respect to R in constant applied frequency 500 Hz under two conditions: the light was turned on (off-on, empty mark) and the light was turned off (on-off, solid mark). The transfer function between V_{in}, V_{out}, X_c and R is derived based on principle of RC circuit as signal attenuation will be proportional to the ratio as below:

$$peak\ V_{out} = \frac{R}{X_c+R} V_{in} \ \ while \ \ X_c = \frac{1}{2\pi f C}$$

where f is applied frequency (Hz), C is the capacitance (F) and X_c is the capacitive reactance (Ω). Note that this relationship was built on the previous work[27] that peak V_{out} has been selected to

represent the change of V_{out} within the temporal timeframe(ΔV_{out}). Extracting the value of X_c is now crucial in order to validate if the relationships are based on equation above. Therefore, we employ electrochemical impedance spectroscopy (EIS) to extract the capacitance (C) of MIScap under dark or illumination condition in Figure 5.12a, this is a common technique to extract bulky/interfacial capacitance. However, the fitting lines obtained from EIS fail to match the curves in both conditions shown in Figure 5.12b.

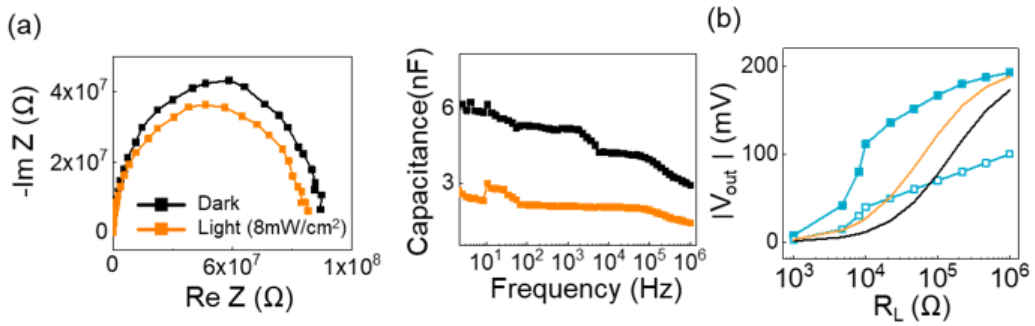

Figure 5.12. EIS measurements under light or dark condition. (a)Extracted capacitances (b) the comparison of experimental results with fitting lines from (a).

It is reasonable that transient capacitance behavior within few μs cannot be probed due to poor control of perturbing illumination condition under EIS measurements or the insulated properties of MIScap impede the current collection during EIS measurements. Instead, we manually fit each individual curve using equation with only the variables V_{in} and X_c, and found that the fitting curves perfectly match the V_{out}-R_L relationships as shown in Figure 5.10a, which implies the strong inherence of MISCap operation is still under principle of RC circuits. Those parameters are summarized into Table 5.1.

Table 5.1. Derived parameters from EIS or fitting results

V_{out} to R_L, as applied f=500 Hz	From EIS (Figure 5.12)			Fitting parameters in Figure 5.11a		
	V_{in} (V)	C (nF)	X_c (Ω)	V_{in} (V)	C (nF)	X_c (Ω)
Light on (on-off)		5	2×10^5	0.2	20	1.6×10^4
Dark (off-on)		2	5×10^5	0.1	9	3.5×10^4

Interestingly, C has been derived to be ~4-fold larger in fitting results than those obtained from EIS under either dark or illumination condition, this provides clear evidence that peak V_{out} effectively reflects the transient carrier involvement during device operation within a temporal timeframe once irradiance on or off upon BHJ. Moreover, the capacitance increments from the dark to light condition are found to be 2.5-fold higher in EIS, which is also consistent with the capacitance increment observed in the fitted results. Those similarities indicate that transient capacitance has solely originated from the photogenerated carrier inside BHJ instead of contributions from external. As a result, these findings lead to the novel principle that V_{out} from high-pass configuration can effectively reflect transient carrier movement/accumulating within sudden change of irradiance levels.

The dynamic behavior of transient carriers during light off-on or on-off conditions are extrapolated from the previous fitted results. During the off-on condition of MIScap, V_{out} reflects the accumulating process of holes from BHJ. During the on-off condition, V_{out} reflects the discharging process of holes back to the BHJ and subsequent recombination. As depicted in Figure 5.11a, V_{out} has smaller signals at off-on than at on-off by 2.25 ± 0.25 times, which is corresponding

to the change of fitting transient capacitance and fitting V_{in} as shown in Table 5.1. The role of fitting V_{in} is to represent the saturated open-circuit voltage (where charges across the Teflon layer create a potential difference with respect to the ground) that occurs under different level of light irradiance on MIScap, and hence determine the amplitude of transient capacitance. Therefore, transient capacitance caused by the movements of charges explains the opposite sign of V_{out} and its peak value during on-off or off-on condition. However, the role of transient capacitance still needs to be complemented in the future.

Due to the concept of voltage divider in high-pass configuration, the level of partial voltage drop on the MIScap varies with different R values. As a result, the effective bias on BHJ in MISCap can be directly adjusted by changing R. Therefore, the optimal operation of MIScap with R can be determined more effectively by analyzing the transient current (i_p) that occurs on R, as shown in Figure 5.11b. The largest i_p occurs when $R_L \cong 10^4\ \Omega$ and hence taken as the optimal configuration in this work. As a result, the working principle of MIScap was mostly determined by the principle of RC circuit. Its voltage responses to pulse of infrared light were summarized in Figure 5.13, the direction and magnitude of gray arrows represent the status of electrons in external circuit, flowing in or out to the ground.

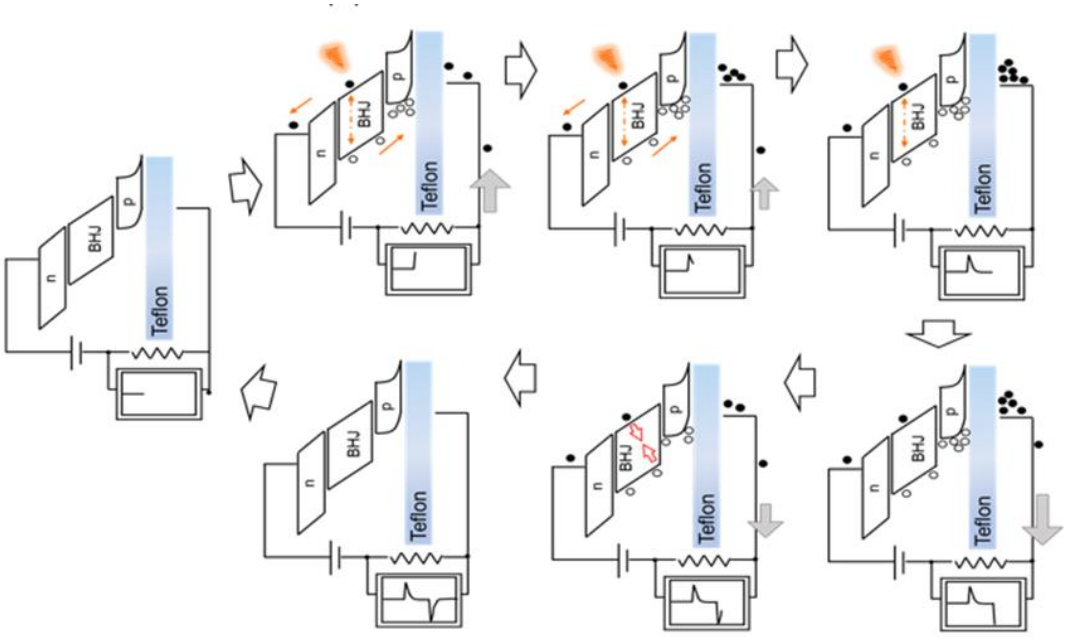

Figure 5.13. Voltage (V_{out}) response in retinomorphic sensor during different phase of a pulse of light. Its working principle is under operation of RC circuit with MIScap served as photosensitive capacitor.

5.5 Figure-of-merit photoresponse in MIScap (retinomorphic sensor)

This section provides a detailed discussion on the device performance of the MIScap structure with high-pass RC circuit (denoted as retinomorphic sensor in the following texts). A new indicator V_{out}, is introduced to investigate the photoresponse in retinomorphic sensor, and the results are summarized in this section. The advantage of retinomorphic sensor will be demonstrated and evaluated through the typical figure-of-merit photodiode parameters.

5.5.1 Dark current evaluation and LDR

One of most critical Figure-of-merits parameters in photoresponse performance is specific detectivity (D*). Therefore, the role of insulated Teflon in MIScap is further investigated by evaluating the level of noise current (I_{noise}) as one of the major components in D*. The specific detectivity (D*) was further determined as followed:

$$D^* = \frac{\sqrt{A\Delta f}}{NEP} = \frac{R\sqrt{A}}{S_n} = \frac{R\sqrt{A\Delta f}}{I_{noise}}$$

where R is spectral responsivity (A/W), A is active area in device (m^2), Δf is detection bandwidth (Hz), NEP is the noise equivalent power, S_n is noise spectral density ($A/Hz^{0.5}$) and I_{noise} is noise current (A). The major contribution to I_{noise} is the dark current, depending on the applied biases, materials properties, temperature and device structure[61]. Among those factors, the major component of dark current is resulted from carrier injection from the external circuits through electrodes as a function of bias, with negligible contribution from thermal generation in the active layer. Therefore, a common strategy to enhance device performances is to reduce dark current by implementing a hole or electron blocking layer that creates energy barrier to suppress charge injections from adjacent electrodes[62]. Similarly, the inserting Teflon in MISCap serves the same purpose to impede the carrier injection from the silver electrode given its absolute electrical insulation. As a result, in Figure 5.14a, the intrinsic dark current in Photodiode shall be greatly reduced in retinomorphic sensor operation.

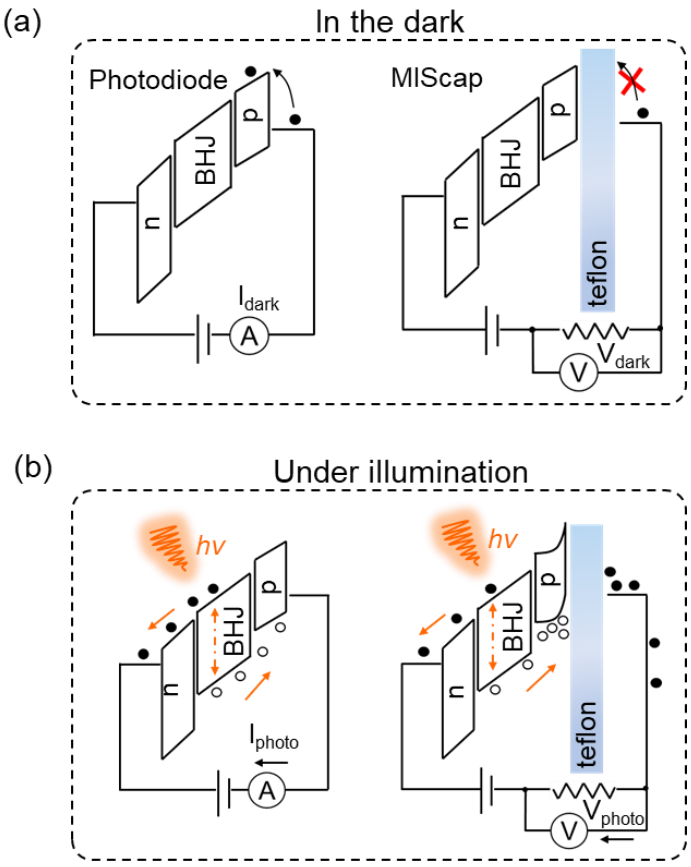

Figure 5.14. Operating principle of MIScap. (a) Inserting insulated Teflon in MIScap suppresses dark current contribution from external electrodes. (b) The effective charge extraction occurs in the Photodiode, instead charge accumulation in MIScap under irradiance.

In Figure 5.14b, under irradiance, receiving photocurrent (I_{photo}) in Photodiode exhibits a proportional response to light intensity, originated from the generation of hole-electron pairs by irradiance, separated and swept by the built-in effective bias in BHJ, and subsequently collected through electrodes. Instead within MIScap, the photogenerated charge (holes) is transported to the interfaces and accumulation persists at teflon interfaces, meanwhile the silver electrode (in the other side of Teflon) is extracting the equivalent amount of opposite charge (electrons) from the ground in order to reach charge balance on both sides of Teflon. As a result, V_{out} reflects the transient flow of electrons on external R in this dynamic process, V_{out} also represents the process of hole transporting or accumulating within MIScap.

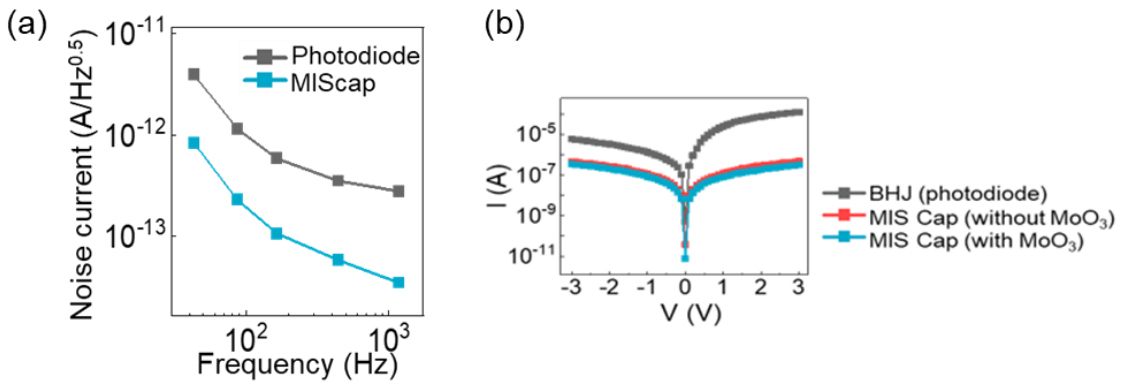

Figure 5.15. Reduced dark current in MIScap. (a) Noise spectra densities of Photodiode and MIScap. (b) IV characteristics for all structures under dark condition

Furthermore, the noise spectral density of MIScap has generally one order smaller than Photodiode in applied frequencies from 10^3 to 10^1 Hz in the level of 10^{-12}~10^{-13} (A/Hz$^{0.5}$) regime shown in Figure 5.15a. From the measured current-voltage characteristics in Figure 5.15b, MIScap also exhibits ~2 order smaller short-circuit current (in the level of 10^{-11} A) than photodiode (~10^{-9} A) under dark condition. Those findings clearly demonstrate the advantage of Teflon in MIScap in the role of suppressing intrinsic dark current.

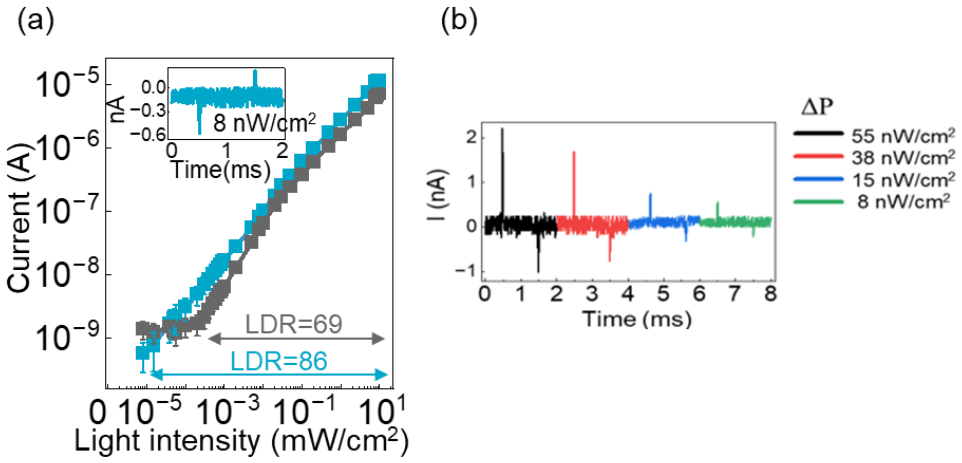

Figure 5.16. Weak light detection. (a) Photoresponse in Photodiode (black) or retinomorphic sensor (Blue) under incident light intensity. (b) Retinomorphic sensor real-time response under different levels of weak light

The capability of infrared light detection for both structures was determined under incident light intensities of 980 nm in Figure 5.16a. V_{out} signals in retinomorphic sensor were converted to photocurrent (for ease of comparison with a Photodiode as equation below. The Photocurrent signal (responsivity) was extracted from the received photocurrent or converted from V_{out}:

$$R_{photodiode} = \frac{(I_p - I_{dark})}{\Delta P}, R_{retinomorphic\ sensor} = \frac{(\frac{V_{out}}{R})}{\Delta P} \text{ (Eqn 2)}$$

where $R_{photodiode}$ or $R_{retinomorphic\ sensor}$ (A/W) is responsivity, I_p(A) is a received photocurrent under illumination, I_{dark} (A) is dark current under dark condition, ΔP (W/cm^2) is intensity of incident light and R(Ω) is an external resistor in high-pass configuration. Benefit from the effective dark current suppression, retinomorphic sensor exhibits better LDR (83.3) than Photodiode (69) in the range of <10^{-5} to 10^1 mW/cm^2. Furthermore, retinomorphic sensor shows the excellent detection capability with ultra-weak light pulse 8 nW/cm^2, as shown inset. retinomorphic sensor's real-time response under levels of weak light from 8-55 nW/cm^2 has been summarized in Figure 5.16b. Those findings are corresponding to the previous reports that figure-of-merits in photodetector performances can be greatly enhanced by suppressing dark current, which mainly overshadowed the light signals especially under ultra-low light intensity regime (below 10^{-3} mW/cm^2).

5.5.2 Cut-off frequency

Frequency range from 10^2 to 10^5 Hz was employed to characterize the responses in Photodiode and retinomorphic sensor under light pulse ΔP=8 mW/cm^2 as shown in Figure 5.17. It clearly shows less attenuation and shorter rising/falling time during retinomorphic sensor responses. Consequently, cut-off frequency (-3dB) of photodiode and retinomorphic sensor is determined to be 21k Hz and 50k Hz, respectively. The greater capacity of retinomorphic sensor is attributed to the effective representation of transient carrier movements/accumulating as discussed earlier.

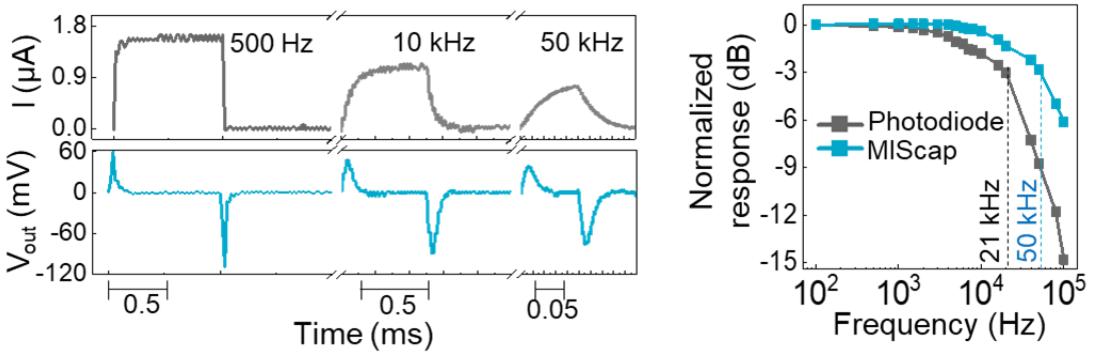

Figure 5.17. Levels of signals attenuation in different applied frequencies under light pulse ΔP=8 mW/cm^2.

5.5.3 Bias dependence

The effect of bias voltage (V_{in}) across MIScap and high-pass configuration have been further dissected and evaluated with $\frac{R}{X_C+R}$. The relationship between V_{in} and V_{out} was summarized into Figure 5.18a. Interestingly, V_{out} shows a gradual increase with a more positive bias ranging from -5 V to 3.5 V until reaching its peak value. This behavior is strikingly different from regular Photodiode operation, where optimum photoresponsivity always occurs at reverse potentials for few V. Hereby, those interesting findings on wide potential window can only be explained through level of charge accumulations occurs on the Teflon interfaces as a function of band bending at positive or negative V_{in} illustrated in Figure 5.18b. The wide range of V_{in} operating potential, spanning from -5 V to 5 V, suggests that the effective bias applied within the BHJ was not highly modulated due to significant voltage drop occurring on the Teflon layer. Combined with the same sign of V_{out} across this wide range of V_{in}, it is reasonable to derive the photosensitive MIScap performance that mostly determined by the level of band bending on the interface, which determines the number of accumulated hole as we draw the similarity of MOS capacitor that level of charge accumulations dependent on applied bias relative to its flat band voltage. V_{out} demonstrates different dependences in the positive or negative V_{in} regimes. We found that the

slope of V_{out}-V_{in} within V_{in}=0 to V_{in}=3.5 V is 0.011 corresponding to value predicted in $\frac{R}{X_c+R}$ as given and that V_{out} rolls off after more positive voltage applied. On the other hand, in the range of V_{in}=0 to V_{in}=-5 V, the slope of V_{out} to V_{in} relationship is smaller (0.005) and there is no rolling behavior. This finding is further supported by our assumption that the level of band bending on interfaces determines the level of the capacitive reactance until the unfavorable effective bias on BHJ probably lead to poorer charge dissociation, resulting in the degrading photoresponse over 3.5 V.

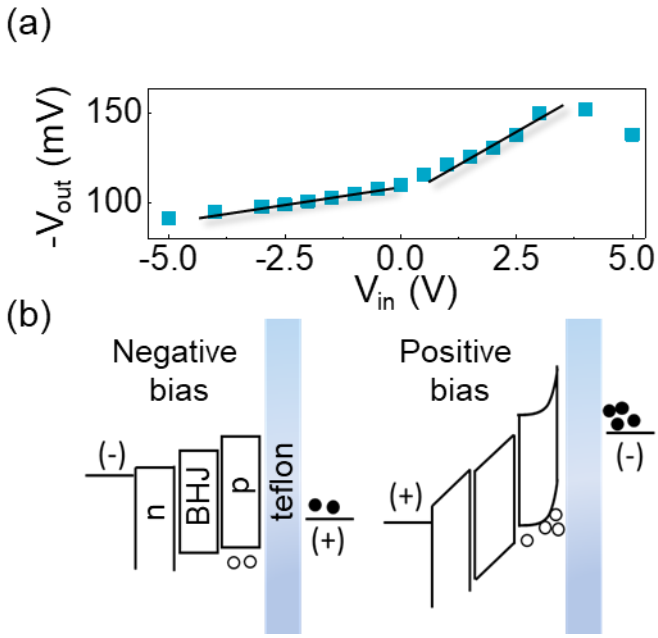

Figure 5.18. (a) V_{out} dependence with input bias (V_{in}). (b) Schematics of charge accumulation dependence on the level of band bending in different V_{in} regime

5.5.4 Infrared Photoresponse

The detectivity and incident light (wavelength as shown inset) of Photodiode and retinomorphic sensor (zero bias) under modulated frequency of 313 Hz and 500 Hz, respectively, is then determined in Figure 5.19. At the peak of 980 nm, the detectivity reaches 8.1×10^9 Jones for

MISCap and 2.8×10^9 Jones in Photodiode. Especially, the detectivity of MIScap can be able to reach 4.5×10^{10} Jones under ultra-weak light pulse 8 nW/cm^2. We successfully proposed a new indicator V_{out} in high-pass configuration to assess the superior figure-of-merit photoresponse performance of retinomorphic sensor than Photodiode.

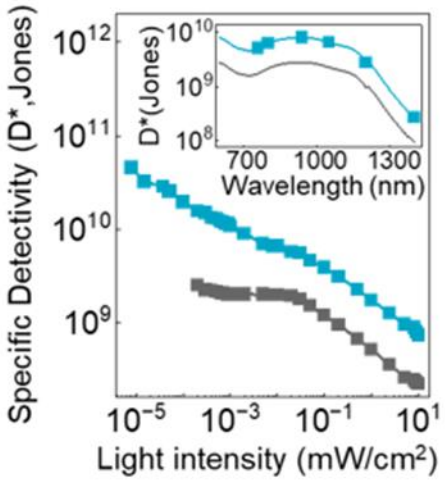

Figure 5.19. Specific detectivity under incident light intensity or wavelength for Photodiode (Black) or retinomorphic sensor (Blue).

5.6 Application on chopper rotation

Given the ultra-fast response of retinomorphic sensor to changes in illumination levels, we first employ retinomorphic pixels to determine the propagating wave after mechanical chopping carried out. As a proof of concept, we derive the spacings between pixels placement and time intervals in the chopper blade under fast rotation. The rate of chopper and design of chopper blade determine the waveform of propagating electromagnetic wave, which serve the crucial importance to investigate signals transmission or modulation in the optoelectronic applications[63]. Three retinomorphic pixels are positioned behind the rotating chopper blade with monochromatic 940 nm light source, and real-time data is collected using an oscilloscope, as depicted in Figure 5.20a. This setup is explained in detailed in Experimental Section. The retinomorphic pixels are irradiated

with 940 nm light pulses at a frequency of 1 kHz and a 50% duty cycle, which is modulated by the rotation speed of the chopper and the 50% area of mixed spacing in the entire chopper blade. Consequently, three MIScaps experience a sequential light-off-on-off condition, reflected in the voltage (V_{out}) signals and displayed on the oscilloscope screen. A customized MATLAB program is then introduced to present the data received from Figure 5.20b in order to visualize the movement of one of the spacings in the chopper blade at three different arbitrary timestamps. This allowed us to observe the clockwise movement of one spacing and its corresponding effect on the voltage signals. As a result, Figure 5.20c compares the voltage waveform of these three retinomorphic pixels. The time between the corresponding peaks of two curves (0.16 ms) can derive the displacement of the devices from traveling speed of chopper (set as 36 °/ms with 1k Hz chopper frequency). However, the displacement of phase was calculated to be 5.8° from the measurement, instead of 7.2° on the actual spacing between devices as shown in Figure 5.21. This 20% deviation might result from complex light scattering on glass substrates/printed holder, light beam focal, or specific waveforms induced by this intermixing chopper blade design, a further compliment of setup are required in the future but now these factors are beyond the scope of this work. In Figure 5.20d, we determine the resolution of retinomorphic pixels by extracting the full width at half maximum (FWHM) of voltage responses in temporal timeframe, where retinomorphic sensor prototype has demonstrated the remarkable potential to track fast infrared light signals up to ~11.6 kHz. We have successfully present first organic retinomorphic protype that is capable of tracking high speed movement of target subject in the SWIR range, which might bring the technological advance to the current developing optoelectronic application.

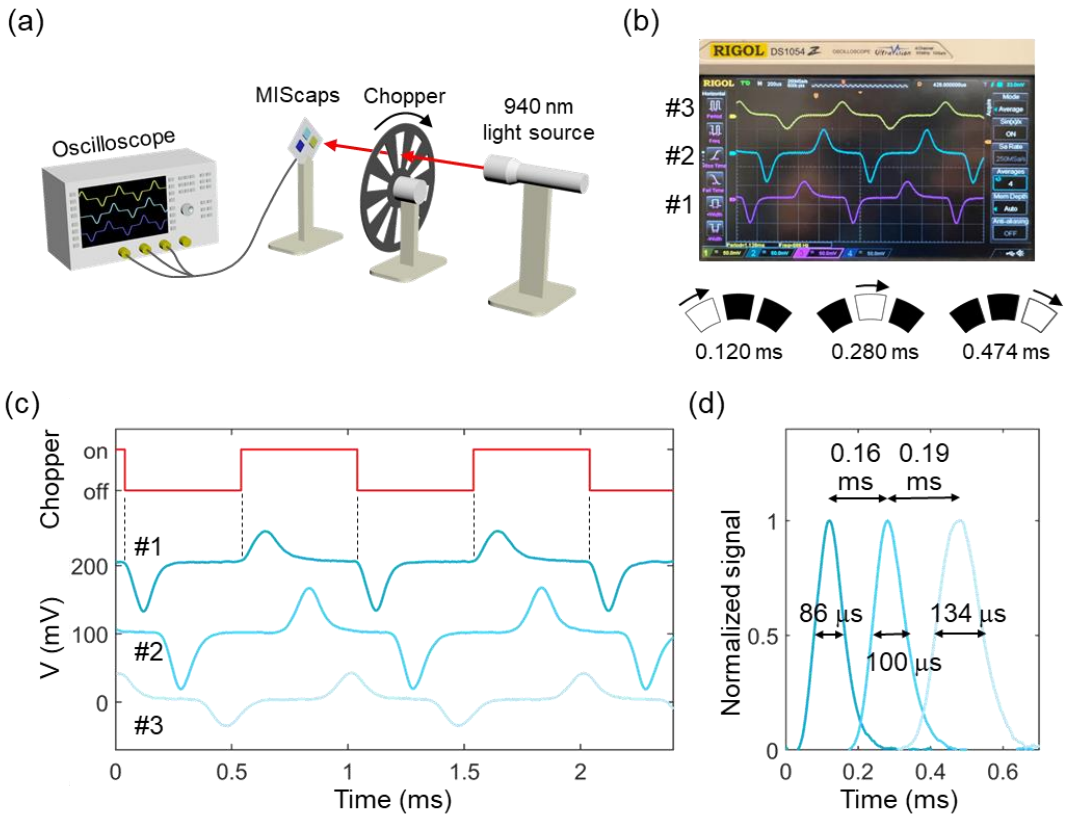

Figure 5.20. Demonstration of motion tracking by integrated retinomorphic system. (a) Setup of measuring the pattern of a light chopper with three retinomorphic sensors. (b) Waveforms of the three retinomorphic pixels captured by an oscilloscope (upper). Traveling pattern of one spacing on the chopper imaged by pixels (lower). (c) Waveforms of the three retinomorphic pixels with 100 mV shifted spacing. The waveform of the chopper is aligned with the first retinomorphic pixel. (d) Normalized signal of the peaks of the three pixels with full width at half maximum (FWHM) marked on each curve.

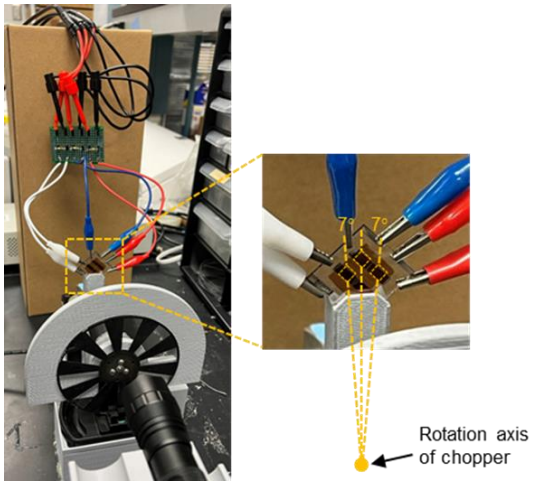

Figure 5.21. The setup of retinomorphic pixels and their relative position

5.7 Conclusion

In summary, we present a simple yet novel optical sensor which features a spiking voltage in response to fast-pulse signal rather than constant illumination. The present device could track ultrafast microsecond level signal with a rapid time response faster than 8 μs and a large -3dB of 50 kHz, that is also controlled by the choice of external resistance. Also, our organic SWIR retinomorphic protype (MIScap) based on simple RC circuits is easily capable of detecting pulsed light signal with an obvious SNR as high as ~3 at an ultra-low light intensity detection of 8 nW/cm^2. More importantly, based on a unique operation mechanism with energetic charge state and transient capacitance confirmed by IMVS and fitting results on principle of RC circuits. This prototype capacitive-mode photodiode features a good device performance with a high specific detectivity of 4.5×10^{10} Jones than regular Photodiode with a similar device configuration due to the effective dark current suppression within MIScap, along with wide operating voltage window from -5 to 5 V. Finally, these good findings further enabled the demonstration of proof-of-concept of high-speed target subject tracking in the SWIR range, manifesting the great potential application of the moving subjects monitoring under seawater.

Chapter 5, in part is currently being prepared for submission for publication of the material. Shuo-En Wu, Longhui Zeng, Yichen Zhai, Chanho Shin, Naresh Eedugurala, Jason David Azoulay, Tse Nga Ng, 2023. Retinomorphic motion detector fabricated with organic infrared semiconductors. The dissertation author was the primary researcher and author of this material.

REFERENCES

1 J. M. Nassar, S. M. Khan, S. J. Velling, A. Diaz-Gaxiola, S. F. Shaikh, N. R. Geraldi, G. A. Torres Sevilla, C. M. Duarte, M. M. Hussain, *npj Flexible Electronics* **2018**, *2*.

2 B. D. Paulsen, S. Fabiano, J. Rivnay, *Annu Rev Mater Res* **2021**.

3 E. Zeglio, O. Inganäs, *Active Materials for Organic Electrochemical Transistors*, Wiley-VCH Verlag, **2018**.

4 B. D. Paulsen, K. Tybrandt, E. Stavrinidou, J. Rivnay, *Organic mixed ionic–electronic conductors*, Nature Research, **2020**.

5 J. Rivnay, S. Inal, B. A. Collins, M. Sessolo, E. Stavrinidou, X. Strakosas, C. Tassone, D. M. Delongchamp, G. G. Malliaras, *Nat Commun* **2016**, *7*.

6 J. Rivnay, S. Inal, B. A. Collins, M. Sessolo, E. Stavrinidou, X. Strakosas, C. Tassone, D. M. Delongchamp, G. G. Malliaras, *Nat Commun* **2016**, *7*.

7 T. H. Le, Y. Kim, H. Yoon, *Electrical and electrochemical properties of conducting polymers*, MDPI AG, **2017**.

8 N. A. Kukhta, A. Marks, C. K. Luscombe, *Molecular Design Strategies toward Improvement of Charge Injection and Ionic Conduction in Organic Mixed Ionic-Electronic Conductors for Organic Electrochemical Transistors*, American Chemical Society, **2022**.

9 J. Rivnay, S. Inal, A. Salleo, R. M. Owens, M. Berggren, G. G. Malliaras, *Organic electrochemical transistors*, Nature Publishing Group, **2018**.

10 S. M. Kim, C. H. Kim, Y. Kim, N. Kim, W. J. Lee, E. H. Lee, D. Kim, S. Park, K. Lee, J. Rivnay, M. H. Yoon, *Nat Commun* **2018**, *9*.

11 B. D. Paulsen, S. Fabiano, J. Rivnay, *Annu Rev Mater Res* **2021**.

12 J. Rivnay, S. Inal, A. Salleo, R. M. Owens, M. Berggren, G. G. Malliaras, *Organic electrochemical transistors*, Nature Publishing Group, **2018**.

13 J. Rivnay, M. Ramuz, P. Leleux, A. Hama, M. Huerta, R. M. Owens, *Appl Phys Lett* **2015**, *106*.

14 A. Giovannitti, R. B. Rashid, Q. Thiburce, B. D. Paulsen, C. Cendra, K. Thorley, D. Moia, J. T. Mefford, D. Hanifi, D. Weiyuan, M. Moser, A. Salleo, J. Nelson, I. McCulloch, J. Rivnay, *Advanced Materials* **2020**, *32*.

15 M. J. Donahue, A. Williamson, X. Strakosas, J. T. Friedlein, R. R. McLeod, H. Gleskova, G. G. Malliaras, *Advanced Materials* **2018**, *30*.

16 J. T. Friedlein, R. R. McLeod, J. Rivnay, *Device physics of organic electrochemical transistors*, Elsevier B.V., **2018**.

17 J. Rivnay, P. Leleux, M. Ferro, M. Sessolo, A. Williamson, D. A. Koutsouras, D. Khodagholy, M. Ramuz, X. Strakosas, R. M. Owens, C. Benar, J. M. Badier, C. Bernard, G. G. Malliaras, *Sci Adv* **2015**, *1*.

18 D. A. Bernards, G. G. Malliaras, *Adv Funct Mater* **2007**, *17*, 3538.

19 D. A. Bernards, D. J. MacAya, M. Nikolou, J. A. Defranco, S. Takamatsu, G. G. Malliaras, *J Mater Chem* **2008**, *18*, 116.

20 F. Cicoira, M. Sessolo, O. Yaghmazadeh, J. A. Defranco, S. Y. Yang, G. C. Malliaras, *Advanced Materials* **2010**, *22*, 1012.

21 M. Ghittorelli, L. Lingstedt, P. Romele, N. I. Crăciun, Z. M. Kovács-Vajna, P. W. M. Blom, F. Torricelli, *Nat Commun* **2018**, *9*.

22 S. Wustoni, C. Combe, D. Ohayon, M. H. Akhtar, I. McCulloch, S. Inal, *Adv Funct Mater* **2019**, *29*.

23 C. Posch, T. Serrano-Gotarredona, B. Linares-Barranco, T. Delbruck, *Proceedings of the IEEE* **2014**, *102*, 1470.

24 Q. B. Zhu, B. Li, D. D. Yang, C. Liu, S. Feng, M. L. Chen, Y. Sun, Y. N. Tian, X. Su, X. M. Wang, S. Qiu, Q. W. Li, X. M. Li, H. B. Zeng, H. M. Cheng, D. M. Sun, *Nat Commun* **2021**, *12*.

25 W. Tong, H. Meffin, D. J. Garrett, M. R. Ibbotson, *Stimulation Strategies for Improving the Resolution of Retinal Prostheses*, Frontiers Media S.A., **2020**.

26 C. Trujillo Herrera, J. G. Labram, *J Phys D Appl Phys* **2021**, *54*.

27 C. Trujillo Herrera, J. G. Labram, *ACS Appl Electron Mater* **2022**, *4*, 92.

28 J. G. Labram, *J Phys D Appl Phys* **2023**, *56*.

29 S. T. Keene, T. P. A. van der Pol, D. Zakhidov, C. H. L. Weijtens, R. A. J. Janssen, A. Salleo, Y. van de Burgt, *Advanced Materials* **2020**, *32*.

30 M. Moser, T. C. Hidalgo, J. Surgailis, J. Gladisch, S. Ghosh, R. Sheelamanthula, Q. Thiburce, A. Giovannitti, A. Salleo, N. Gasparini, A. Wadsworth, I. Zozoulenko, M. Berggren, E. Stavrinidou, S. Inal, I. McCulloch, *Advanced Materials* **2020**, *32*.

31 A. F. Paterson, A. Savva, S. Wustoni, L. Tsetseris, B. D. Paulsen, H. Faber, A. H. Emwas, X. Chen, G. Nikiforidis, T. C. Hidalgo, M. Moser, I. P. Maria, J. Rivnay, I. McCulloch, T. D. Anthopoulos, S. Inal, *Nat Commun* **2020**, *11*.

32 A. Giovannitti, K. J. Thorley, C. B. Nielsen, J. Li, M. J. Donahue, G. G. Malliaras, J. Rivnay, I. McCulloch, *Adv Funct Mater* **2018**, *28*.

33 M. Sessolo, J. Rivnay, E. Bandiello, G. G. Malliaras, H. J. Bolink, *Advanced Materials* **2014**, *26*, 4803.

34 M. P. Zarabadi, F. Paquet-Mercier, S. J. Charette, J. Greener, *Langmuir* **2017**, *33*, 2041.

35 Y. Zhao, X. guang Hu, S. Hu, Y. Peng, *Applications of fiber-optic biochemical sensor in microfluidic chips: A review*, Elsevier Ltd, **2020**.

36 M. Cuartero, G. Crespo, T. Cherubini, N. Pankratova, F. Confalonieri, F. Massa, M. Lou Tercier-Waeber, M. Abdou, J. Schäfer, E. Bakker, *Anal Chem* **2018**, *90*, 4702.

37 L. Campanella, C. Colapicchioni, G. Crescentini, M. P. Sammartino, Y. Su, M. Tomassetti, B Sensitive membrane ISFETs for nitrate analysis in waters, **1995**.

38 S. E. Wu, L. Yao, A. Shiller, A. H. Barnard, J. D. Azoulay, T. N. Ng, *Adv Electron Mater* **2021**, *7*.

39 J. Ahn, J. Lee, S. Kim, C. Kim, J. Lee, P. M. Biesheuvel, J. Yoon, *Desalination* **2020**, *476*.

40 S. H. Roelofs, A. Van Den Berg, M. Odijk, *Microfluidic desalination techniques and their potential applications*, Royal Society of Chemistry, **2015**.

41 K. Wang, L. Yao, M. Jahon, J. Liu, M. Gonzalez, P. Liu, V. Leung, X. Zhang, T. N. Ng, *ACS Energy Lett* **2020**, *5*, 3276.

42 T. Kim, W. Choi, H. C. Shin, J. Y. Choi, J. M. Kim, M. S. Park, W. S. Yoon, *Applications of voltammetry in lithium ion battery research*, Korean Electrochemical Society, **2020**.

43 M. Cuartero, G. A. Crespo, M. Ghahraman Afshar, E. Bakker, *Anal Chem* **2014**, *86*, 11387.

44 S. E. Wu, A. Shiller, A. Barnard, J. D. Azoulay, T. N. Ng, *Microchimica Acta* **2022**, *189*.

45 H. Liu, Q. Li, S. Zhang, R. Yin, X. Liu, Y. He, K. Dai, C. Shan, J. Guo, C. Liu, C. Shen, X. Wang, N. Wang, Z. Wang, R. Wei, Z. Guo, *Electrically conductive polymer composites for smart flexible strain sensors: a critical review*, Royal Society of Chemistry, **2018**.

46 H. Liu, H. Zhao, S. Li, J. Hu, X. Zheng, R. Li, Y. Chen, Y. Su, *Adv Mater Technol* **2019**, *4*.

47 L. Li, Y. Bai, L. Li, S. Wang, T. Zhang, *Advanced Materials* **2017**, *29*.

48 M. Cucchi, H. Kleemann, H. Tseng, G. Ciccone, A. Lee, D. Pohl, K. Leo, *Adv Electron Mater* **2021**, *7*.

49 J. Ji, X. Zhu, D. Han, M. Li, Q. Zhang, Y. Shu, Z. Cheng, W. Zhang, E. Hua, S. Sang, *Molecules* **2019**, *24*.

50 J. Ji, Y. Fu, J. Wang, P. Y. Chen, D. Han, Q. Zhang, W. Zhang, S. Sang, X. Yang, Z. Cheng, *J Mater Chem C Mater* **2020**, *8*, 11499.

51 Y. Xu, T. Minari, K. Tsukagoshi, J. A. Chroboczek, G. Ghibaudo, *J Appl Phys* **2010**, *107*.

52 L. Yao, J. Liu, N. Eedugurala, P. Mahalingavelar, D. J. Adams, K. Wang, K. S. Mayer, J. D. Azoulay, T. N. Ng, *Cell Rep Phys Sci* **2022**, *3*.

53 S. Takamatsu, T. Takahata, M. Muraki, E. Iwase, K. Matsumoto, I. Shimoyama, *Journal of Micromechanics and Microengineering* **2010**, *20*.

54 M. Bhattacharjee, M. Soni, P. Escobedo, R. Dahiya, *Adv Electron Mater* **2020**, *6*.

55 Z. Wu, Y. Zhai, H. Kim, J. D. Azoulay, T. N. Ng, *Acc Chem Res* **2018**, *51*, 3144.

56 C. Shin, N. Li, B. Seo, N. Eedugurala, J. D. Azoulay, T. N. Ng, *Mater Horiz* **2022**, *9*, 2172.

57 Y. T. Set, B. Li, F. J. Lim, E. Birgersson, J. Luther, *Appl Phys Lett* **2015**, *107*.

58 J. Bisquert, F. Fabregat-Santiago, I. Mora-Seró, G. Garcia-Belmonte, S. Giménez, *Journal of Physical Chemistry C* **2009**, *113*, 17278.

59 A. Upadhyaya, C. M. Singh Negi, A. Yadav, S. K. Gupta, A. S. Verma, *Superlattices Microstruct* **2018**, *122*, 410.

60 L. Zeng, W. Han, S. E. Wu, D. Wu, S. P. Lau, Y. H. Tsang, *IEEE Trans Electron Devices* **2022**, *69*, 6212.

61 G. Simone, M. J. Dyson, C. H. L. Weijtens, S. C. J. Meskers, R. Coehoorn, R. A. J. Janssen, G. H. Gelinck, *Adv Opt Mater* **2020**, *8*.

62 N. Li, X. Hu, X. Sui, Q. Chen, T. N. Ng, *ACS Appl Electron Mater* **2022**.

63 J. Zheng, G. Sun, Y. Jiang, T. Wang, A. Huang, Y. Zhang, P. Tang, S. Zhuang, Y. Liu, S. Yin, F. Wu, X. Q. Zhang, J. Y. Cheung, K. B. Shi, Z. W. Liu, C. Luo, S. Yin, P. Ruffin, G. Lu, J. Zhang, F. T. S Yu, 0180) Microscopy; (090.2890) Holographic optical elements; (110.2970) Image detection systems, Plenum Press, **2006**.